UNIVERSIDADE FEDERAL DE PERNAMBUCO
CENTRO DE TECNOLOGIA E GEOCIÊNCIAS
DEPARTAMENTO DE ELETRÔNICA E SISTEMAS
PROGRAMA DE PÓS-GRADUAÇÃO EM ENGENHARIA ELÉTRICA

TÚLIO DE LIMA PEDROSA

EXPLORING NANOPARTICLE SIZE DEPENDENCE IN PHOTOTHERMAL APPLICATIONS

Recife

2024

TÚLIO DE LIMA PEDROSA

EXPLORING NANOPARTICLE SIZE DEPENDENCE IN PHOTOTHERMAL APPLICATIONS

Tese apresentada ao Programa de Pós-Graduação em Engenharia Elétrica da Universidade Federal de Pernambuco como requisito parcial para obtenção do grau de Doutor em Engenharia Elétrica.

Área de Concentração: Fotônica.

Orientador: Prof. Dr. Renato Evangelista de Araujo.

Recife

2024

.Catalogação de Publicação na Fonte. UFPE - Biblioteca Central

Pedrosa, Tulio de Lima.
Exploring nanoparticle size dependence in photothermal applications / Tulio de Lima Pedrosa. - Recife, 2024.
150f.: il.

Tese (Doutorado) - Universidade Federal de Pernambuco, Centro de Tecnologia e Geociências, Programa de Pós-Graduação em Engenharia Elétrica, 2024.
Orientação: Renato Evangelista de Araújo.
Inclui referências, apêndices e anexos.

1. Energia solar; 2. Fotoacústica; 3. Nanopartículas de ouro; 4. Ressonância de plasmons de superfície localizados; 5. Terapia fototérmica; 6. Termoplasmônica. I. Araújo, Renato Evangelista de. II. Título.

UFPE-Biblioteca Central

TÚLIO DE LIMA PEDROSA

EXPLORING NANOPARTICLE SIZE DEPENDENCE IN PHOTOTHERMAL APPLICATIONS

Tese apresentada ao Programa de Pós-Graduação em Engenharia Elétrica da Universidade Federal de Pernambuco como requisito parcial para obtenção do título de Doutor em Engenharia Elétrica.

Aprovada em: 29/07/2024.

BANCA EXAMINADORA

Prof. Dr. Renato Evangelista de Araujo (Orientador)
Universidade Federal de Pernambuco

Prof. Dr. Eduardo Fontana (Examinador Interno)
Universidade Federal de Pernambuco

Prof. Dr. Anderson Monteiro Amaral (Examinador Externo)
Universidade Federal de Pernambuco

Prof. Dr. Luis Arturo Gómez Malagón (Examinador Interno)
Universidade de Pernambuco

Prof. Dr. Carlos Jacinto da Silva (Examinador Externo)
Universidade Federal de Alagoas, Brazil

Prof. Pierre-François Brevet, PhD. (Examinador Externo)
Claude Bernard University Lyon 1

Recife

2024

Aos meus pais.

ACKNOWLEDGEMENTS

Do que vivi, uns dizem que foi sorte. Do que aprendi, alguns dirão que foram bençõs. Eu aproveito o ensejo para dizer que, tudo isso, apenas foi. E de tudo que foi, fica esta, que nada mais é do que um símbolo de gratidão e apreciação por tudo que tem ocorrido em minha vida. Neste momento, gostaria de poder transmitir o meu pensamento de forma poética, mas como sei não poder fazê-lo, recorrerei a palavras mais diretas.

Agradeço a Deus pelo sopro da vida e pelas oportunidades que temos sempre de recomeçar.

Agradeço a meu pai, Emerson, e a minhã mãe, Cristiane, por todo o suporte proporcionado ao longo desses proveitosos anos, onde, além de muito carinho, não faltaram incentivos para aprender coisas novas. A ética do trabalho que trago no peito só se aprende na observação de exemplos, e levarei comigo a durante a vida inteira. A minha irmã Tábata e ao meu irmão Tales pelos momentos compartilhados durante todos estes anos. Se a distância física nos separa, o carinho fraternal nos aproxima mais a cada ano que passa. A Rayane, minha noiva e companheira, por todo amor e afeto, sempre ao meu lado nos momentos de maiores aflições. De ti, nunca faltou compreensão (nem mesmo à distância).

Ao Centro Espírita Deus a Procura de Seus Filhos, do qual faço parte desde que nasci e que é parte integral de minha formação. Por me guiar nesse período enquanto casa de trabalho e oração, e na minha busca por espiritualidade.

Ao Professor Renato Evangelista de Araujo, por acreditar sempre em meu potencial e facilitar minha participação em atividades e programas dos quais normalmente não faria parte. Sua forma humanizadora de orientar é inspiradora e deixa uma marca profunda em quem almeja um dia seguir o magistério superior.

A toda a equipe que compõe o LOBI e que torna o ambiente de convívio sempre agradável. Meus mais sinceros agradecimentos a Mariana Crispim e Caio Judá nas discussões, conversas e contribuições nas atividades coletivas e individuais. Em especial, agradeço a Gabrielli Oliveira por tomar a frente e viabilizar a execução dos trabalhos com fungos e camundongos, a Caio Vital pelo suporte na condução dos experimentos de aquecimento solar e a Arthur Pereira por viabilizar os experimentos fotoacústicos nas amostras deste trabalho. A completude desta tese, devo a tantos finais de semana e feriados com vocês compartilhados dentro de um laboratório.

Ao Laboratório de Computação Embarcada e Tecnologias Industriais (LaCETI), onde aperfeiçoei meus conhecimentos e desenvolvi novas habilidades que me são muito uteis. Lá trabalhei com pessoas incríveis, com as melhores conversas na hora do almoço. Nunca esquecerei das paradas obrigatórias no Panela de Barro durante as visitas a Belo Jardim.

Ao Prof. Diego Rátiva por permitir o uso das instalações do IIT/UPE para a realização dos ensaios de aquecimento solar e ao Prof. Anderson Gomes por disponibilizar a infra-estrutura do Laboratório de Fotônica do DF/UFPE para a excução dos experimentos fotoacústicos. Agradeço também ao Prof. Georges Boudebs (Physique - Laboratoire Lphia, Université Angers, França) pela contribuição na caracterização de lente térmica de nossas amostras e a Ilia Goemaere (Biophotonics Research Group, Ghent University, Bélgica) por ceder gentilmente as amostras de nanopartículas de polidopamina para ensaio de aquecimento solar.

A Sebastian Wachsmann-Hogiu (Department of Bioengineering, McGill University, Canada), agradeço todo o apoio prestado durante os meses em que fui visitante do seu laboratório e a hospitalidade que me foi proporcionada, tanto no ambiente profissional como na cidade de Montreal em si. Agradeço também a oportunidade de apresentar trabalho na Photonics West 2024. A sua orientação ajudou a desenvolver novos pontos de vista que me ajudaram a amadurecer um pouco mais cientificamente.

Foi um prazer trabalhar com Reza Abbasi, Xinyue Hu e Meruyert (Mira) Imanbekova. A eles devo toda a camaradagem e muitos momentos felizes em Montreal. As conversas generalistas e sobre computação com Benjamin e aos almoços com Jashandeep Kaur conversando sobre a vida. Aos bons momentos compartilhados com os roomates Sacha Lightbound e Anand Anto, sempre com muitas conversas na hora de cozinhar. A todos os bons amigos que fiz em Montreal, mas que não pude citar.

Aos amigos brasileiros que já tinha ou que fiz em Montreal, que compuseram a rede de apoio para quem está longe de casa: a Catarina Cataldi, por me ajudar durante minha mudança para a cidade, atuando como uma verdadeira guia e conselheira, sempre checando o meu bem estar nos momentos difíceis. A Arthur Pimentel, pelos passeios na cidade e conversas agradáveis. A Arthur Pereira, por todos as caminhadas no Mont Royal e as incontáveis visitas ao Eaton Center para comer e conversar.

Por último, mas não menos importante, agradeço a CNPq e a CAPES, a primeira por fomentar o meu doutorado durante os três primeiros anos, e a segunda por pagar o meu salário durante o ano de sanduíche em Montreal, Canadá.

Dizia o poeta: “A vida é arte do encontro embora haja tanto desencontro pela vida.” A todos e a todas que cruzaram o meu caminho, mas que por esquecimento ou falta de espaço não foram citados, meus mais sinceros agradecimentos e consideração.

"Desaprender 8 horas por dia ensina os princípios."

Manoel de Barros, Uma didática da invenção (1993).

RESUMO

O papel fundamental de nanopartículas (NPs) em aplicações médicas e em tecnologias de captação de energia tem sido alvo de extensivas análises na última década. NPs com diferentes formatos podem oferecer grande absorção óptica e demonstram grande potencial nos casos em que o aquecimento fototérmico (AF) é explorado. Entretanto, restrições como tamanho e concentração, relacionadas ao uso de NPs metálicas em processos clínicos, limitam severamente a eficácia de processos térmicos. Além disso, a necessidade de escalabilidade em aplicações de conversão energética utilizando coletores solares culmina em elevados custos de operação. Dessa forma, estratégias que reduzam a quantidade de material requerida em tais aplicações é fundamental para sua implementação em ambientes reais. Nesta tese, objetivamos investigar a dependência do AF com o tamanho da NP, a fim de estabelecer uma metodologia para a identificação de NPs com tamanho otimizado, baseada na análise de figuras de mérito ($\mathrm{J_o}$, $\mathrm{S^2F}$ e $\mathrm{SJ_o}$). A dependência do fotoaquecimento de NPs com o tamanho da nanoestrutura foi investigada utilizando uma abordagem teórica e experimental, com uso da técnica espectroscópica de lente térmica e câmera térmica. As estratégias de otimização, empregadas para nanoesferas e nanobastões de ouro (AuNSs e AuNRs), culminaram na identificação dos tamanhos ideais de NPs, que foram posteriormente utilizadas na fotoinativação térmica (IFT) de *Candida albicans*, na terapia fototérmica (TFT) em camundongos e como agentes de contraste para imageamento fotoacústico através da comparação do desempenho de tamanhos ótimos e sub ótimos. Em seguida, NPs de polidopamina (PDA) foram investigadas para aquecimento solar, expandindo o escopo da otimização de nanoaquecedores para fontes de banda larga através da introdução de uma nova figura de mérito ($\mathrm{SJ_o}$). Para AuNSs, observamos que a temperatura global se assemelha ao comportamento do $\mathrm{J_o}$, com diâmetro ideal de 50 nm para AuNS. A técnica de lente térmica permitiu a estimativa da temperatura intermediária de uma única NP, que se mostrou semelhante ao comportamento de $\mathrm{S^2F}$, com desempenho máximo esperado para diâmetro de 80 nm. Para AuNRs, tamanhos menores são mais eficientes para conversão fototérmica, conforme indicado pelo $\mathrm{J_o}$. Para AuNRs isolados, entretanto, $\mathrm{S^2F}$ sugere que o desempenho ideal é alcançado para AuNRs de tamanho 90×25 e 150×30 nm para 808 e 1064 nm, respectivamente. A análise teórica de $\mathrm{SJ_o}$ revelou tamanho ideal de aproximadamente 180 nm para nanoesferas de polidopamina, e o experimento sugeriu que o efeito da dependência do tamanho no aumento da temperatura segue o $\mathrm{SJ_o}$ calculado, conforme inicialmente hipotetizado. Ao abordar problemas práticos, o trabalho contribui para o avanço na compreensão dos processos de otimização de NPs para diversas aplicações e permite aos pesquisadores discernirem configurações ideais que maximizam a eficiência da geração de calor e minimizam os efeitos colaterais indesejáveis.

Palavras-chave: Energia solar, Imageamento fotoacústico, Inativação fototérmica, Nanopartículas de ouro, Otimização, Polidopamina, Ressonância de plasmons de superfície localizados, Terapia fototérmica, Termoplasmônica.

ABSTRACT

The fundamental role of nanoparticles (NPs) in medical applications and energy harvesting technologies has been the subject of extensive analysis in the last decade. NPs with different shapes can offer great optical absorption and demonstrate great potential in cases where photothermal (PT) heating is exploited. However, restrictions such as size and concentration, related to the use of metallic NPs in clinical processes, severely limit the effectiveness of thermal processes. Furthermore, the need for scalability in energy conversion applications using solar collectors results in high operational costs. Therefore, strategies that reduce the amount of material required in such applications are essential for their implementation in real environments. In this thesis, we aim to investigate the dependence of PT heating on NP size, in order to establish a methodology for the identification of size optimized NPs, based on the analysis of figures of merit, the Joule number $\mathrm{J_o}$ for pulsed laser excitation, $\mathrm{S^2F}$ for continuous laser excitation and $\mathrm{SJ_o}$ for broadband heating. The dependence of PT heating of NPs with the size of the nanostructure was investigated using a theoretical and experimental approach, using the thermal lens spectroscopic technique and thermal camera. The optimization strategy, employed for gold nanospheres and nanorods (AuNSs and AuNRs), culminated in the identification of ideal sizes of NPs, which were subsequently used in the thermal photoinactivation (PTI) of *Candida albicans*, in photothermal therapy (PTT) in mice and as contrast agents for photoacoustic imaging by comparing the performance of optimal and suboptimal sizes. Next, polydopamine (PDA) NPs were investigated for solar heating, expanding the scope of nanoheater optimization for broadband sources by the introduction of a new figure of merit ($\mathrm{SJ_o}$). For AuNSs, we observed that the global temperature resembles the behavior of $\mathrm{J_o}$, with an ideal diameter of 50 nm for AuNS. The thermal lens technique allowed the estimation of the intermediate temperature of a single NP, which was similar to the behavior of $\mathrm{S^2F}$, with maximum performance expected for a diameter of 80 nm. For AuNRs, smaller sizes are more efficient for photothermal conversion, as indicated by $\mathrm{J_o}$. For isolated AuNRs, however, $\mathrm{S^2F}$ suggests that optimal performance is achieved for AuNRs of size 90×25 and 150×30 nm for 808 and 1064 nm, respectively. Theoretical analysis of $\mathrm{SJ_o}$ revealed the optimal size of PDA nanospheres in water is approximately 180 nm, and the experimental results suggested that the effect of size dependence on temperature increase follows the calculated $\mathrm{SJ_o}$, as initially hypothesized. By addressing practical problems, this work contributes to advancing the understanding of NP optimization processes for diverse applications and allows researchers to discern optimal configurations that maximize heat generation efficiency and minimize undesirable side effects.

Keywords: Localized surface plasmon resonance. Gold nanoparticles. Photoacoustic imaging. Photothermal inactivation. Photothermal Therapy. Polydopamine. Size optimization. Solar energy. Thermoplasmonics.

LIST OF FIGURES

LIST OF TABLES

LIST OF ABBREVIATIONS AND ACRONYMS

AIDS	Acquired immunodeficiency syndrome
ANSI	American National Standards Institute
AP	Apoptosis
AR	Aspect ratio
ATCC	American Type Culture Collection
BSA	Bovine Serum Albumin
CEEA	Comitê de Ética em Experimentação Animal
CID	Chemical Interface Damping
CMOS	Complementary Metal–Oxide–Semiconductor
CTAB	Cetyltrimethylammonium bromide
CW	Continuous wave
DAMP	Damage-associated molecular patterns
DASC	Direct Absorption Solar Collector
DDA	Discrete Dipole Approximation
DSO	Digital storage oscilloscope
ESF	Edge spread function
FDA	Food and Drug Administration
FEM	Finite Element Method
FoM	Figure of Merit
FoV	Field of View
FWHM	Full Width at Half Maximum
FWP	Full waveplate
GHG	Greenhouse gases
HE	Hematoxylin and eosin stain

IC50	Half-maximal inhibitory concentration
IR	Infrared
IV	Intravenous
Jo	Joule number
LED	Light emitting diode
LNA	Low noise amplifier
LSF	Line spread function
LSPR	Localized Surface Plasmon Resonance
MI	Muscle invagination
MLWA	Modified long wavelength approximation
MPE	Maximum permissible exposure
MSU	Monosodium urate
NE	Necrosis
NF	Nanofluid
NIR	Near-infrared
NP	Nanoparticle
NR	Nanorod
OPO	Optical parametric oscillator
PA	Photoacoustic
PAI	Photoacoustic imaging
PAM	Photoacoustic microscopy
PAT	Photoacoustic tomography
PBS	Phosphate Buffered Saline
PD	Photodiode
PDA	Polydopamine
PDI	Photodynamic inactivation

PEG	Polyethylene glycol
PML	Perfectly matched layer
PTI	Photothermal inactivation
PTT	Photothermal therapy
PVC	Polyvinyl chloride
QCL	Quantum cascade laser
S180	Murine Sarcoma 180
S2F	Steady-state factor
SEM	Scanning Electron Microscopy
SJo	Spectral Joule number
TIR	Total internal reflection
TIRF	Total internal reflection fluorescence
TL	Thermal lens
TLM	Thermal lens microscopy
UST	Ultrasound transducer
UV	Ultraviolet
UV-Vis	Ultraviolet-Visible

LIST OF SYMBOLS

ω	Angular frequency
ω_p	Plasma frequency
ϵ	Relative permittivity
ϵ_0	Vacuum permittivity
ϵ_m	Medium permittivity
ϵ'	Real part of relative permittivity
ϵ''	Imaginary part of relative permittivity
ϵ_{bulk}	Bulk permittivity
j	Imaginary unit
N	Density of free electrons
e	Elementary charge
m_e	Electron's rest mass
γ_0	Bulk damping parameter
γ	Modified damping parameter
A	Surface scattering constant
v_F	Fermi velocity
l_∞	Mean free path
L_{eff}	Effective mean free path
V_{np}	NP volume
S	NP surface area
r	NP radius
k	Wavenumber
λ	Wavelength
σ_{sca}	Scattering cross section

σ_{abs}	Absorption cross section
σ_{ext}	Extinction cross section
q	Heat power density
$\vec{E}$	Electric field vector
$\vec{r}$	Position vector
P_{abs}	Total heat power
V	Domain volume
dV	Domain differential element
I	Irradiance
τ_{ep}	Electron–phonon characteristic time
τ_p	Thermal relaxation time
ρ_{np}	Density of the NP
c_{np}	Heat capacity of the NP
κ_{np}	Thermal conductivity of the NP
κ_m	Thermal conductivity of the medium
ρ_{bf}	Density of the basefluid
c_{bf}	Heat capacity of the basefluid
κ_{bf}	Thermal conductivity of the basefluid
ρ_{nf}	Density of the nanofluid
c_{nf}	Heat capacity of the nanofluid
κ_{nf}	Thermal conductivity of the nanofluid
R_{eq}	Equivalent nanoparticle radius
η	Photothermal conversion efficiency
t	Time
f	Laser repetition rate
ΔT_{np}^{fs}	Temperature increase over time for one fs pulse for a single nanoparticle

$\langle \Delta T_{np}^{fs} \rangle$	Average temperature increase over one fs pulse for a single nanoparticle
ΔT_{np}^{CW}	Steady-state temperature increase for CW excitation for a single nanoparticle
ΔT_{global}	Global temperature increase
ΔT_{global}^{fs}	Global temperature increase due to fs illumination
ΔT_{global}^{CW}	Global temperature increase due to CW illumination
$\dot{Q}_{in}$	Power source density
$\dot{Q}_{out}$	Power loss density
a_n	Mie scattering coefficient
b_n	Mie scattering coefficient
m_r	Relative refractive index
x	Nanosphere size parameter
ψ_n	Riccati-Bessel function of the 1st kind and nth order
ξ_n	Riccati-Bessel function of the 2st kind and nth order
d	Nanoparticle diameter
α_p	Dipole polarizability
α_x	x-axis spheroidal polarizability
α_x'	Corrected x-axis spheroidal polarizability
α_y	y-axis spheroidal polarizability
α_z	z-axis spheroidal polarizability
L_x	Spheroidal shape factor along x-axis
L_y	Spheroidal shape factor along y-axis
L_z	Spheroidal shape factor along z-axis
e	Spheroid eccentricity
AR	Aspect ratio
L	Nanorod/spheroid length
D	Nanorod/spheroid diameter

λ_{ref}	Reference wavelength (1 eV)
β	Shape correction factor
S^2F	Steady-state factor
J_o	Joule number
$\#_{np}$	Total number of nanoparticles
C_{np}	Volumetric density of nanoparticles
p	Volume fraction
λ_p	Plasmon peak wavelength
ℓ	Optical path length
w_0	Beam waist at the focus
M_{tot}	Total mass of nanoparticles
Δp	Change in pressure
$\Delta \rho$	Change in medium density
c_0	Speed of sound in medium
ρ_0	Equilibrium density of the medium
β_V	Thermal coefficient of volume expansion of the medium
F	Laser fluence
W	Weber contrast
I_S	Photoacoustic intensity
I_B	Average background photoacoustic intensity
SJ_o	Spectral Joule number
α_{np}	Nanoparticle absorption coefficient
α_{bp}	Basefluid absorption coefficient
α_{nf}	Nanofluid absorption coefficient
E_λ	Spectral irradiance of the source
A_m	Solar weighted coefficient

A_c	DASC's surface area
U	Fluid flow velocity
H	DASC's height
L	DASC's length
h	DASC's heat loss coefficient
T_{amb}	Ambient temperature
T_{sun}	Temperature at the Sun's surface
T_{in}	Input temperature of the fluid
T_{out}	Output temperature of the fluid
Δx	Spacing in horizontal direction
Δy	Spacing in vertical direction
$\dot{m}$	Fluid mass flow rate
η_{th}	DASC's thermal efficiency
η_{ex}	DASC's exergy efficiency
J_{Txy}	Polarization rotation matrix
J_{xy}	Jones matrix for x-polarized light
M_{y-pol}	Jones matrix of y-axis polarizer
M_{fwp}	Jones matrix of FWP
M_{sample}	Jones matrix of the sample
ϕ_0	Phase shift introduced by the FWP
ϕ	Phase shift introduced by the sample
δ	Optical path difference
t	Thickness of birefringent sample
Δn	Birefringence of the sample

CONTENTS

1 INTRODUCTION

Metallic nanostructures have been receiving increasing attention in the last decade as important materials for optical applications such as optical therapies [2], medical diagnosis [3] and energy harvesting [4]. Nanoparticles (NPs) with different formats offer great optical absorption in the visible and near-infrared (NIR) region and demonstrates a great potential for use in cases which photothermal conversion is appreciated. Therefore, the development of methodologies for the identification of nanostructures optimized for photothermal applications is essential for the introduction of new nanostructured materials. The large optical absorption of metallic nanostructures arises from the collective oscillation of the metal's conduction electrons, a phenomenon called Localized Surface Plasmon Resonance (LSPR). The electric field of incoming light induces charge separation, that is responsible for the emergence of a restoring force between the negative and positive charge centers in the NP, driving the system to return to its original stable configuration. If excited at the proper frequency, this restoring force is the origin of a resonance effect [5] in which very high electric field enhancement can be achieved inside and outside the NP.

In many applications where NPs are used, heat is, oftentimes, a major problem to overcome. For instance, the local heating arising from plasmonic structures elicit changes in the surrounding refractive index due to thermo-optic effect [6] or lead to the denaturation of biomolecules and proteins in biosensing frameworks [7]. Furthermore, the high temperatures achieved can also lead to reshaping and melting dynamics [8] as well as micro-bubble formation [9,10], all of which are detrimental for sustaining plasmon resonance. Exist, however, occasions where the generation of heat must be appreciated. Notably, the introduction of materials that allow the integration of diagnostic and therapeutic processes is of great interest in the medical field [11]. In this regard, the LSPR phenomenon has been explored in photothermal processes for the destruction of cells and tissues, such as microorganisms and malignant tumors [12,13] taking advantage of the electric field damping via Joule Effect. In this context, the use of optimized nanoheaters as theranostic (therapy and diagnosis) agents for photoacoustic (PA) imaging and thermal therapies is an innovative approach.

Optical techniques such as photothermal inactivation (PTI) have been explored in the control of microbiological contamination [14]. Both PTI and photothermal therapy (PTT) relies on the increase in temperature, due to light absorption, for localized thermal destruction of biological structures [15]. In thermal treatments, a well-localized heating is desired, leading to temperature increase in a restricted tissue volume. Thermal therapy is reliant not only on the final temperature reached, but also on the time extension the heating is sustained and for this purpose thermal-conduction devices, ultrasonic and electromagnetic waves have been exploited as heating sources for medical thermal procedures [13]. Moreover, lasers and LEDs are widely explored in

optical therapies. In particular, the use of infrared (IR) light sources at the biological window allows deep tissue (few centimeters range) treatment. At the biological window, absorption and scattering process are minimized, leading to a partial transparency of tissues. Two spectral bands are defined as ideal for optical therapy: i) the first biological window that extends from 650 nm to 950 nm; and ii) the second biological window, which extends from 1000 nm to 1400 nm [16].

Simultaneously, solar thermal energy has become a promising alternative for energy applications such as domestic hot water production and industrial processes that require heat. Typical solar thermal collectors are surface absorbers, based on a solid surface to harvest sunlight and transfer heat to working fluids such as water and oils [17]. Such collectors have many losses, exchanging significant amounts of heat with the environment via convection and radiation. In this context, Direct Absorption Solar Collectors (DASC) eliminate the surface absorber and rely on working fluids to better harvest solar energy in volumetric manner [17]. To efficiently convert solar radiation into heat, the working fluid must be able to effectively absorb most of the energy available in a wide range of the solar spectrum. This is achieved by the use of nanofluids (NFs), a regular mixture of working fluid with nanomaterials capable of modifying the thermal and optical properties of the liquid [17].

Plasmonic NPs are excellent candidates to compose NFs. For instance, the strong absorption of metal NPs across the visible range is widely explored for DASC applications [17,18]. The excellent stability of metal oxides have also been exploited for thermal solar collectors, however their optical performance is reduced in comparison to metal NPs due to its wide energy bandgaps [17]. On the other hand, transition metal nitride nanofluids have been reported to significantly enhance the performance of DASCs in comparison to Au NFs ($\sim 40\%$) due its low optical scattering and broad absorption spectra [19]. In this sense, DASCs may be potentially employed in applications that requires low temperature increase [20]. Despite of its promises, there is a lack of technology readiness level assessments for such devices, requiring the simplification and increase in reliability of the entire heating system to become competitive [21]. Furthermore, the search for alternative NFs comprising of cheaper materials with optimized size may drive cost reduction and enable more rational use of resources.

1.1 MOTIVATION

The progressive increase in fungal infections in health care institutions corresponds to a serious public health problem, being associated with high rates of morbidity and mortality. This situation worsens with the increase in yeast resistance to antifungal agents, which leads to therapeutic failure and makes it difficult to fight invasive infections. The emergence of a wide variety of pathogens resistant to chemical agents has attracted the attention of the antimicrobial chemotherapy industry. Candida albicans is a fungus that is among the many organisms that inhabit the human mouth and digestive system, and that (under normal circumstances) do not induce harmful health effects. However, population imbalance (excess) of this fungus results in

candidiasis, that causes serious oral and vaginal infections in patients with immunosuppressive diseases, such as AIDS, who are hospitalized in an intensive care unit or undergoing chemotherapy. The search for alternative procedures for instrument and surface sterilization is a topic of relevant medical interest [22].

Processes and inputs that increase the efficiency of thermal therapies are targets of scientific and medical attention. In this context, nanostructures become a highly desirable technology for therapy. Metallic NPs have also been explored for PA imaging [23], which combines the high resolution achieved by optical imaging techniques with the high penetration depth capabilities provided by ultrasound methodologies [24]. In PA imaging (tomography, microscopy and endoscopy), laser light is sent to a target tissue and part of the light energy is converted into heat. The generated heat induces the transient thermoelastic expansion of the target, giving rise to an acoustic emission. Therefore, the amplitude of PA signals is related to temperature increase and is intrinsically tied to photothermal phenomena [25]. The detection of the optically generated ultrasonic wave allows the construction of 2D and 3D images, mapping the tissue.

The shape, size and composition of metallic NPs defines the application of nanostructures in medical-therapeutic procedures. The establishment of NP preparation methodologies with different configurations, which enhances the electromagnetic fields close to the metallic particle and with plasmon resonance frequency in different regions of the electromagnetic spectrum (from visible to IR) is a major concern for bio-applications. In general, to achieve IR resonances, which allow optical therapies in deep regions of biological tissues, the dimensions of the nanostructures are greater than 20 nm. Other factors regarding the use of NPs as treatment platforms in humans raise concerns regarding accessibility from a clinical standpoint. The amount of laser energy administrable within safety levels may not be enough to efficiently induce adequate thermal variation, rendering the technique to become impractical. For instance, laser exposition of human skin at 1064 nm is limited to 100 mJ/cm^2 for laser pulses shorter than 100 ns and 1 W/cm^2 for CW illumination [26], limitations that the optimal administration of NPs might help overcome.

Additionally, despite being extensively studied in biomedical applications, the versatility of NPs extend their usefulness to other areas. In the energy field, for instance, the search for renewable sources to fulfill the progressive replacement of global energy balances to levels projected by sustainable development goals, has made the use of solar resources highly appreciated due to the abundance of solar radiation incident on Earth that can be used in thermal conversion processes. The improvement of solar collectors through the use of new materials is an important factor that contributes to their adoption as viable energy source. For instance, the use of working fluids containing plasmonic NPs, specially gold, allows for more efficient conversion of the solar spectrum converted into heat [27].

However, the amount of material required to make the adoption of gold-containing systems possible culminates in high costs and makes the scalability of such devices impractical. Thus, the search for alternative materials capable of reducing costs while preserving solar ab-

sorption performance is of utmost importance. Polymers are good examples of materials that can replace noble metals, as they are cheaper and can perform as well as gold (Au) NPs in solar applications. This is the case of polydopamine (PDA) NPs, which have high absorption in the visible and NIR spectra and have been used as a photosensitizer agent in thermal applications [14,28].

1.2 OBJECTIVES

The goal of this thesis was to establish a methodology based on a size-dependent approach for the identification of optimized (high-performance) NPs to be used in photothermal processes under monochromatic and broadband illumination.To achieve the objectives of this work, the following steps were carried out:

- Thermal and electric field evaluation of NPs by simulation;
- Characterization of Au nanospheres and nanorods (theoretical);
- Optimization gold nanospheres for photothermal conversion (theoretical);
- Evaluation (experimental) of the photothermal conversion performance of colloidal NPs;
- Evaluation of the performance of optimal Au nanorods in the photoinactivation of Candida albicans (experimental);
- Assessment of PTT of Sarcoma 180 in mice using optimal Au nanorods (experimental);
- Appraisal of the influence of optimal Au nanospheres and nanorods in PA generation (experimental);
- Establish figure of merit for photoheating of NPs subjected to broadband illumination;
- Characterization of Au and PDA nanospheres for broadband (solar) illumination (theoretical);
- Temperature increase assessment by Au and PDA nanospheres under solar irradiation (experimental);
- Performance evaluation of DASC with NFs containing Au and PDA nanospheres (theoretical).

1.3 OVERVIEW

This thesis is organized in seven chapters. The chapters were arranged to mirror the path followed to perform this research and are separated by theme: 1) Introduction; 2) Thermoplasmonics; 3) Nanoheater optimization; 4) Photoinactivation of Candida albicans and Photothermal Therapy in mice; 5) Plasmon-mediated photoacoustic generation in gold NFs; 6) Spectral Joule

number for absorption of broadband light sources: gold and polydopamine solar NFs; and 7) Conclusions and future prospects. The first two chapters are of introductory nature, establishing the basis for the applications described from chapters 4 to 6.

The second chapter discusses the optical and thermal properties of plasmonic NPs. Here, the importance of the Drude model for the description of permittivity and the impact of NP size are shown. The Localized Surface Plasmon Resonance effect is introduced, as well as its effects to the optical cross section of NPs. Moreover, this chapter assesses the collective heating of NPs under monochromatic excitation, providing figures of merit to quantify heat generation in each case. Subsequently, chapter 3 explores the methodologies previously introduced for the optimization of Au nanospheres and Au nanorods in aqueous medium.

In chapter 4, optimized Au nanorods are applied and tested in thermal therapy. From theoretical results, the performance of two distinct nanorod sizes (optimal and sub-optimal) are compared for PTI of Candida albicans (in vitro) and PTT in mice (in vivo). NP cytotocixity is discussed and the effectiveness of the the thermal treatment in cancer cells is briefly examined.

The existing links between temperature increase and PA generation grounds the investigation performed in chapter 5. Here, the effects of the optimization of Au nanospheres and Au nanorods for temperature increase are assessed for PA generation in gold NFs employing PA microscopy setup. The effect of NP size is considered for contrast enhancement and NP stability under high power nanosecond laser pulses is mentioned.

Chapter 6 broadens the methodology for NP optimization introducing a new metric for the appraisal of plasmonic heating under broadband light sources. Within this framework, the optical heating of PDA NPs of different sizes is examined for solar energy harvesting and its performance is compared with Au NPs. This process is further extended to assess the use of PDA NPs as constituents of the absorbing workfluid in solar thermal panels through the simulation of DASCs, evaluating temperature distribution.

The last chapter (*Conclusions and future prospects*) discusses the usefulness of the accomplished results and their applicability. Finally, the contributions that resulted from the work carried out are highlighted, including publications in scholarly peer-reviewed journals and participation in conferences.

Three additional appendices were included to supply further information about the techniques, tools and analyses not reported in the main body of the thesis. *Appendix A* features the Thermoplasmonics library developed in Python and used to accomplish this work. This library uses Mie and Mie-Gans theories to calculate the optical cross sections of plasmonic NPs and integrates it to a thermal module using the Finite Difference Method (FDM) to simulate DASCs. *Appendix B* describes the basics of Finite-Element Method and features instructions to motivate the simulation of optical and thermal properties of nanoparticles in *COMSOL Multiphysics*. Furthermore, *Appendix C* report the activities performed and results accomplished during the

one year period of international collaboration in the Department of Bioengineering of McGill University (Canada). Moreover, two annexes were included. *Annex A* incorporate the refractive index of polydopamine extracted from published thin film results found in the literature. This data was extensively used in chapter 6, but is not available elsewhere. Finally, the awards received for scientific and technical production related to this thesis are shown in *Annex B*.

2 THERMOPLASMONICS

Thermoplasmonics is defined as the field of plasmonics that handles the generation of heat by light absorbing NPs. Here, electric field damping caused by the localized plasmon resonance effect is explored in the heating of metallic NPs and their surroundings. Therefore, the knowledge of temperature increase at the NP surface as well as the temperature gradient in the environment become highly desirable.

On this basis, thermoplasmonics has been applied in photothermal assisted catalysis of chemical reactions such as photosynthesis and methane production [29], solar energy applications by thermal [19,30] and hybrid [31] harvesting through the heating of fluids containing NPs and multimodal imaging by the merge of photoacoustic and optical coherence tomography [32]. The heating of the plasmonic NPs have also been used to on biopplications such as sensing using plasmonically controlled Polymerase Chain Reaction for real-time fast point-of-care diagnostics [33,34] and Surface Enhanced Raman Scattering based detection [35], in addition to photothermal cancer therapy [36,37]. The field also includes sub-diffraction trapping using plasmonic optical tweezers [38] and label-free thermometry [39], among other applications.

2.1 DIELECTRIC FUNCTION OF METALLIC NANOPARTICLES

The optical properties of metals can be described by modeling the transport phenomenon of electrons in metals. This approach is know as Drude Model [40] and evokes the kinetic theory of gases to represent the conduction electrons of metals as a gas cloud moving in a static background of heavy ions, for which the Coulomb interaction among electrons (independent carriers) and between electrons and the background ions (unbounded/free electrons) are to be neglected. In the presence of external fields, the electrons move accordingly to Newton's laws of motion, that is damped by collisions between electrons and the static ions of the background. Using this semi-classical approach, the permittivity of metals is given by [40]:

$$\epsilon(\omega) = 1 - \frac{\omega_p^2}{\omega^2 + j\gamma_0\omega} \ , \tag{2.1}$$

in which, $\omega_p = \sqrt{\frac{Ne^2}{\epsilon_0 m_e}}$ is the plasma frequency, with N representing the density of free-electrons, e the elementary charge, m_e the mass of the electron, ϵ_0 the vacuum permittivity, and γ_0 the bulk damping parameter. In Equation 2.1, the bulk damping parameter is proportional to the ratio between the Fermi velocity and the mean free path of the electron cloud ($\gamma_0 \propto v_F/l_\infty$). As the size of the metallic structure decreases, the probability of collisions also diminishes, while collisions with NP surface increases. This is specially true in the nanometric regime, where the NP diameter has dimensions comparable to the mean free path of the conduction electrons. This

aspect leads to the reduction of the mean free path and increase of the damping factor, causing the permittivity of metallic NPs to be size dependent [41]. Therefore, the damping parameter can be written as:

$$\gamma = \gamma_0 + A\frac{v_F}{L_{eff}} \ , \tag{2.2}$$

where the effective mean free path is $L_{eff} = 4V_{np}/S$ for convex shapes. Here, S is the NP surface area and V_{np} is the NP volume. If the NP is spherical, $L_{eff} = 4r/3$, r representing the radius of the NP. The surface scattering constant (*A*) is an empirical parameter that describes the scattering at the surface of nanostructures or at the interface between materials at composite nanostructures. For spheres, *A* is usually considered to be equal to one [42], while the surface scattering parameter for nanords lies between 0.25 and 0.5 [43,44]. Beyond accounting for the semi-classical elastic scattering of electrons at the NP surface, the A parameter also depends on the type of medium surrounding the particle. The surface of NPs often consists of a mix of different chemical species or functional groups (often stabilizers), which interact with molecules in the surrounding medium. These interactions modify surface charge and can cause energy losses in a phenomena known as Chemical Interface Damping (CID) [45,46]. Altough such interactions can give rise to adsorbate induced resonant states that greatly affects LSPR [45], CID modeling is not considered in our analysis.

To compute the size dependent permittivity of metallic NPs, one can start from experimental permittivity data available for bulk metals (ϵ_{bulk}) in the literature, as it already takes into account the intraband and interband contributions to the permittivity. The size dependence is obtained by adding the term of Drude equation containing the damping parameter γ_0, and subtracting the term with the modified damping factor γ (Equation 2.2) instead. Therefore, the size dependence of NP permittivity is given by [42]:

$$\epsilon(\omega) = \epsilon_{bulk}(\omega) + \frac{\omega_p^2}{\omega^2 + j\omega\gamma_0} - \frac{\omega_p^2}{\omega^2 + j\omega\left(\gamma_0 + A\frac{v_F}{L_{eff}}\right)} \ . \tag{2.3}$$

Table 1 shows the values of each parameter in Equation 2.3 for gold. From the bulk gold permittivity [47] it's possible to evaluate the real and imaginary permittivity of gold nanospheres in the visible and near infrared regions.

Figures 1A and 1B show, respectively, the real and imaginary permittivities of gold nanospheres ranging from 5 to 40 nm in radius. One can notice that Figure 1A have negative values of real permittivity, while Figure 1B show that smaller particles have higher losses. The model derived in Equation 2.3 however, is limited to nanostructures larger than 5 nm. For smaller NPs, quantum effects related to a reduced number of atoms in the crystal start to appear [50], and thus, the description of the crystal permittivity using the Drude model becomes insufficient.

Table 1 – Parameters of bulk gold.

Parameter	Value	Description	Reference
ω_p	1.369×10^{16} rad/s	Plasmon frequency	48
A	1	Surface scattering constant	43
v_F	1.4×10^{6} m/s	Fermi velocity	49
γ_0	1.07×10^{14} s^{-1}	Bulk damping factor	48

Figure 1 – Size dependent permittivity for gold nanospheres of radius 5, 10, 20 and 40 nm. **A.** Real permittivity. **B.** Imaginary permittivity.

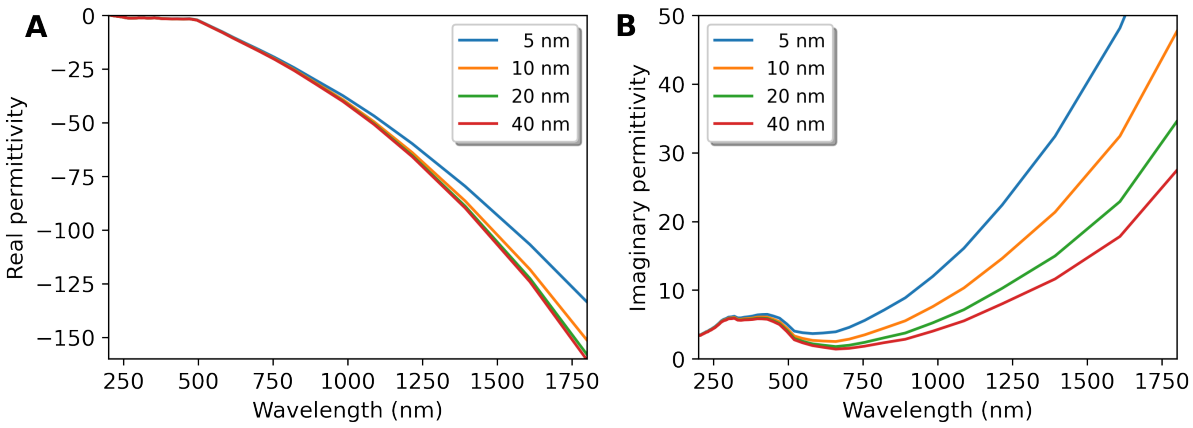

Source: belongs to the author.

2.2 MIE THEORY

Mie theory is a rigorous mathematical description of the absorption and scattering of plane electromagnetic waves by metallic spherical NPs embedded in an infinite dispersive medium, that is also isotropic and uniform. It follows that the scattering cross section and the extinction cross section are respectively given by [51]:

$$\sigma_{sca} = \frac{2\pi}{k^2} \sum_{n=1}^{\infty} (2n+1)(|a_n|^2 + |b_n|^2) \ , \tag{2.4}$$

and

$$\sigma_{ext} = \frac{2\pi}{k^2} \sum_{n=1}^{\infty} (2n+1) \ \mathrm{Re}\left\{a_n + b_n\right\} \ . \tag{2.5}$$

In Equations 2.4 and 2.5, $k = \frac{2\pi}{\lambda}\sqrt{\epsilon_m}$ is the wavenumber for incident light at wavelength λ in a medium of relative permittivity ϵ_m. Also,

$$a_n = \frac{m_r\psi_n(m_r x)\psi'_n(x) - \psi_n(x)\psi'_n(m_r x)}{m_r\psi_n(m_r x)\xi'_n(x) - \xi_n(x)\psi'_n(m_r x)} \ , \tag{2.6}$$

$$b_n = \frac{\psi_n(m_r x)\psi'_n(x) - m_r\psi_n(x)\psi'_n(m_r x)}{\psi_n(m_r x)\xi'_n(x) - m_r\xi_n(x)\psi'_n(m_r x)} \ , \tag{2.7}$$

in which $\psi_n(x)$ and $\xi_n(x)$ are the Riccati-Bessel functions with $x = kr$. Here, *r* is the nanosphere radius and $m_r = \sqrt{\epsilon(\omega)/\epsilon_m}$ is the ratio between the complex refractive index of the NP and the refractive index of the medium. The absorption cross section can be obtained by subtracting the scattering cross section from the extinction cross section, as:

$$\sigma_{abs} = \sigma_{ext} - \sigma_{sca} \ . \tag{2.8}$$

The power series expansion in terms of *n* represents the resonant modes of the NP. The dipole is represented by $n = 1$, the quadrupole by $n = 2$, and so on. Higher order modes are associated to higher energies and larger particles. As the excitation energy or particle size increases, higher order modes become more important. Typically for NPs smaller than 30 nm in diameter, only the lowest order contributions are considered. This is equivalent to set a_n, and b_n to zero, except for a_1 and b_1, reducing the cross sections to what is known as Rayleigh approximation. Thus:

$$\sigma_{ext} = k \ \mathrm{Im}\left\{4\pi r^3 \left[\frac{m_r^2 - 1}{m_r^2 + 2}\right]\right\} \ , \tag{2.9}$$

$$\sigma_{sca} = \frac{k^4}{6\pi}\left|4\pi r^3 \left(\frac{m_r^2 - 1}{m_r^2 + 2}\right)\right|^2 \ . \tag{2.10}$$

However, equation 2.9 is accurate only if scattering is much smaller than absorption [51]. Therefore:

$$\sigma_{abs} = k \ \mathrm{Im}\left\{4\pi r^3 \left(\frac{m_r^2 - 1}{m_r^2 + 2}\right)\right\} \ . \tag{2.11}$$

The validity of the Rayleigh approximation in NP resonance gives a dipole-like radiation pattern to its scattered fields. As higher modes of oscillation gain more importance, the radiation pattern of their scattered fields becomes more pronounced in certain directions, giving the known

forward scattering characteristic that is commonly associated with Mie theory. This simpler way of evaluating what is happening locally when light interacts with a spherical NP assumes the wavelength of incident light to be considerably larger than the NP diameter d ($\lambda \gg d$). In turn, the electric field interacting with the nanosphere remains approximately uniform at all times, enabling the electrostatic approach known as the quasi-static approximation. The field homogeneity across the particle displaces the electron cloud, accumulating charges at the NP boundary and inducing an instantaneous polarization described by the dipolar polarizability (α_p) [5]:

$$\alpha_p = 4\pi r^3 \left(\frac{m_r^2 - 1}{m_r^2 + 2} \right) \ . \tag{2.12}$$

Therefore, in general, scattering and absorption cross sections are written as:

$$\sigma_{sca} = \frac{k^4}{6\pi} |\alpha_p|^2 \ \text{and} \tag{2.13}$$

$$\sigma_{abs} = k \ Im \{\alpha_p\} \ . \tag{2.14}$$

2.3 MIE-GANS THEORY

Although Mie theory provides a very robust framework for the extraction of the optical cross sections of isotropic NPs such as spheres and multilayered shells, it cannot be used for NPs with anisotropic shapes, since there is no closed form solution of Maxwell's equations available. Complex shapes typically require the implementation of numerical solutions and modeling such as Discrete-Dipole Approximation (DDA) [52] and Finite Element Method (FEM) [53] to obtain its optical properties. While FEM breaks the complex geometry into smaller domains and applies Maxwell's equations, the Direct Dipole Approximation approach approximates a complex shape as a finite array of small polarizable dipoles and superimposes its fields. For more information regarding FEM, refer to Appendix B.

Nevertheless, the quasi-static approach of Mie theory can still be extended to approximate anisotropic NPs resembling spheroidal shapes, such as rods (prolate spheroids) and disks (oblate spheroids). Therefore, for spheroidal NPs much smaller than the wavelength of light, Mie-Gans theory may be applied [54]. The calculation is performed representing the polarizability for each spheroidal axis separately. Assuming an elongated (prolate) NP parallel to the x-axis, the polarizability for the x-axis (α_x) is [51,55]:

$$\alpha_x = \frac{V_{np}}{L_x + \frac{1}{m_r^2 - 1}} \ , \tag{2.15}$$

for, V_{np} the NP volume L_x the shape factor for the polarizability along the x-axis. In this particular case, the shape factor of the long axis is [51]:

$$L_x = \frac{1-e^2}{e^2}\left[\frac{1}{2e}\ln\left(\frac{1+e}{1-e}\right)-1\right] \ . \tag{2.16}$$

Here e is related to the NP aspect ratio (AR) by $e = \sqrt{1-1/\mathrm{AR}^2}$, and due to the prolate spheroid symmetry, the shape factor of the shorter axes is then given by $L_y = L_z = (1-L_x)/2$ [51].

However, Equations 2.15 and 2.16 do not precisely describe nanorods, since their shape quickly diverges from spheroid for increasing ARs. Moreover, as Mie-Gans theory arises from the quasi-static approximation, it only accounts for the dipole term of the plasmon resonance. For larger NPs, higher order terms must be considered to include retardation and depolarization effects, which is done using the Modified Long Wavelength Approximation (MLWA) in the long axis (x-axis) [56,57]:

$$\alpha'_x = \frac{\alpha_x}{1 - j\frac{k^3}{6\pi}\alpha_x - \frac{k^2}{2\pi L}\alpha_x} \ . \tag{2.17}$$

where L is the longer length of the prolate spheroid. The last term in the denominator accounts for red-shifts due to depolarization as the NP size increases, while the imaginary term accounts for radiative damping [57]. Hence, the effective polarizability is the sum of the polarizability of each axis ($\alpha_p = \alpha'_x + \alpha_y + \alpha_z$).

2.4 LOCALIZED SURFACE PLASMON RESONANCE

Cross section approximations using the quasi-static approach are obtained exploring the polarizabily of the sphere (2.12) or prolate spheroid (2.17) in Equations 2.13 and 2.14. From the complex dielectric function of metals, $\epsilon = \epsilon' + j\epsilon''$, the optical cross sections for spherical NPs are:

$$\sigma_{sca} = \frac{8\pi k^4 r^6}{3}\frac{(\epsilon'-\epsilon_m)^2+\epsilon''^2}{(\epsilon'+2\epsilon_m)^2+\epsilon''^2} \quad \text{and} \tag{2.18}$$

$$\sigma_{abs} = 4\pi k r^3 \frac{\epsilon_m \epsilon''}{(\epsilon'+2\epsilon_m)^2+\epsilon''^2} \ , \tag{2.19}$$

in which ϵ_m is the medium permittivity. Equations 2.18 and 2.19 indicate that all cross sections increase considerably and peaks when the denominator goes to zero, i.e., $(\epsilon'+2\epsilon_m)^2+\epsilon''^2 = 0$.

This condition states that real part of the nanosphere permittivity must be negative $\epsilon' = -2\epsilon_m$, at the same time that ϵ'' must be small, a constraint know as Fröhlich condition. If the Fröhlich condition is met, the forced oscillation of the conduction electrons is sustained, giving rise to the Localized Surface Plasmon Resonance (LSPR) [58]. Similarly, for rod-like NPs (considering only the resonance along the long axis), Equation 2.15 may also be used to obtain the resonant condition. Here, the Fröhlich condition is met when $[\epsilon_m + L_x(\epsilon' - \epsilon_m)] + (\epsilon'' L_x)^2 = 0$ (obtained by plugging Equation 2.15 in Equations 2.13 and 2.14).

The presence of medium permittivity in the Fröhlich condition implies that plasmon peak is sensitive to changes in the medium refractive index. Beyond that, LSPR properties are also dependent on parameters such as NP material, shape and size. The spectral region in which LSPR occurs depends upon the free carrier density of the NP material [58]. Noble metals such as Cu, Ag and Au constitutes the most commonly studied plasmonic materials, as their high density of carriers place the LSPR in the visible region, while non-noble metals, such as Pb and Al, exhibit LSPR frequencies in the UV region of the spectrum [5,41] and display broader LSPR bands. The LSPR of doped semiconductor NPs occurs typically at infrared wavelengths and their high thermochemical stability is promising for thermoplasmonic applications [59]. Besides, their active gain may be explored in more sophisticated applications.

NPs have been synthesized in a diversity of shapes. For instance, nanocubes [60–65], nanocages [60,66], nanoprisms [67,68], nanorods [69–72], nanodisks [73,74], and nanoshells [75–77] have been extensively explored for various applications. Such structures control the absorption and scattering contributions to plasmon spectrum via anisotropy and enables multiple resonant modes as well as LSPR tunability. Despite being normally obtained by chemical synthesis, physical methods have also been explored to produce complex shape NPs. For instance, shape and inter-particle distance control is achieved by lithographic techniques [78], and high stability NPs are produced using laser ablation techniques [79].

As the size of a NP increases, the non-homogeneity of the electric field in the NP induces dephasing to the oscillating electrons and creates retardation effects, inducing the broadening and red-shift of plasmon peak [5]. In most cases, new resonant modes arise due to anisotropy in NP shape, what is specially true for gold nanorods (AuNRs). For AuNRs, size is directly related to longitudinal mode LSPR tunability [80], tied to its AR, defined as the ratio of its length (L) to its width (D). This tunability enable near-infrared operation AuNRs and provide higher absorption structures, which makes them exceptionally desirable for biomedical applications [81].

To better illustrate shape and size contributions to LSPR, Figure 2A shows the difference between Fröhlich conditions for gold nanosphere (AuNS) and AuNR of size 18 nm (red dashed line) and 40×10 nm (blue dashed line) respectively, embedded in aqueous medium ($\epsilon_m \sim 1.77$). NP sizes were chosen so the volume of gold is the same for both shapes. The black solid line is the real part of gold permittivity divided by the medium permittivity (ϵ'/ϵ_m). While for the AuNS resonance condition is achieved when $\epsilon'/\epsilon_m = -2$, for AuNR the longitudinal polarizability

dominates the effect and pushes it to a longer wavelength. Here, $\epsilon'/\epsilon_m = (1 - 1/L_{\mathrm{x}})$ and is approximately -14. Figure 2B depict the absorption cross section of 18 nm AuNS (red solid line) and 40 $\times$ 10 nm AuNR (blue solid line) in aqueous medium. One can easily notice the shifted LSPR of the AuNR occurring at $\sim$ 800 nm against the $\sim$ 520 nm of the AuNS. Furthermore, despite having the same mass of gold, the AuNR shows larger absorption cross section. The absorption cross sections were calculated using Equation 2.14 along the respective polarizabilites for spheres and rod-like NPs, as described previously.

Figure 2 – **A.** Real part of bulk gold permittivity divided by the medium permittivity (ϵ'/ϵ_m) and Fröhlich conditions for 18 nm AuNS (red dashed line) and AuNR of size 40 $\times$ 10 nm (blue dashed line). **B.** Absorption cross section of 18 nm AuNS (red solid line) and 40 $\times$ 10 nm AuNR (blue solid line) using the quasi-static approximation. In all cases, aqueous medium was considered.

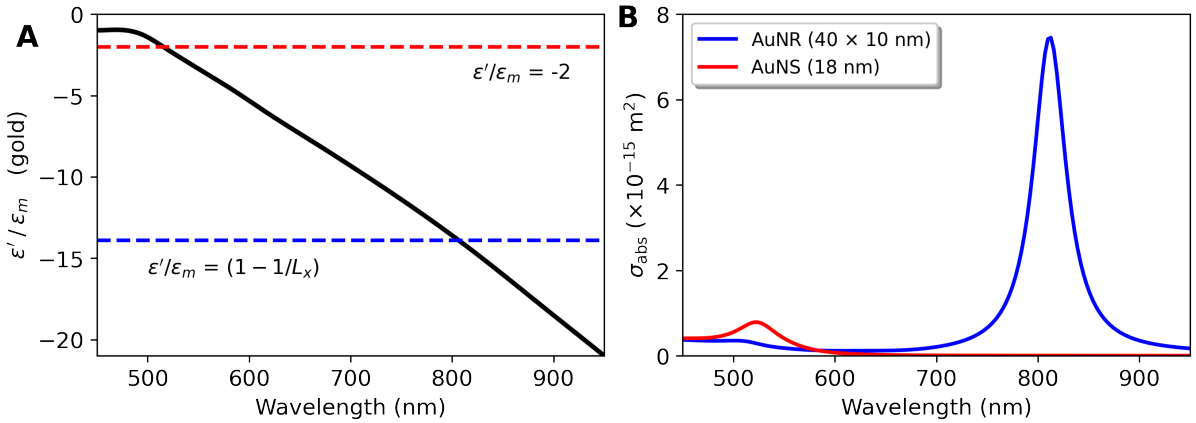

Source: belongs to the author.

2.5 JOULE HEATING

In thermoplasmonics, heat is generated through the absorption of light by NPs supporting LSPR modes in a process known as photothermal conversion. During illumination, the conduction electrons of the metallic NP oscillate in response to the incident excitation field, with the same frequency. The oscillation of this electron cloud inside the NP is, therefore, an electric current that dissipates energy via Joule effect. The heat power density (q) within the NP is given by [5]:

$$q(\vec{r}) = \frac{1}{2}\omega\epsilon_0 \; Im\{\epsilon(\omega)\} \left|\vec{E}(\vec{r})\right|^2 \;, \tag{2.20}$$

where ω is the angular frequency of oscillation, $\epsilon(\omega)$ is the frequency dependent complex permittivity of the metal, ϵ_0 is the vacuum permittivity and $\vec{r}$ is the position vector. The total heat power delivered by the NP is obtained integrating Equation 2.20 over the nanostructure volume. Therefore, the total heat power, P_{abs} is [5]:

$$P_{abs} = \frac{1}{2}\omega\epsilon_0 \, Im\{\epsilon(\omega)\} \int_V dV \left|\vec{E}(\vec{r})\right|^2 . \tag{2.21}$$

The heat power density is proportional to the square of the electric field, i.e, is proportional to the intensity of incident light, and therefore, Equation 2.21 is rewritten as $P_{abs} = \sigma_{abs} I$, in which *I* is the irradiance of the excitation source. This simplifies Equation 2.21 for use with arbitrarily shaped NPs.

To better understand heat delivery by NPs, it's important to grasp the timescales involved in the process from heat generation to heat exchange with the surroundings, which is a determining factor for NP selection based on application specificity. When radiation strikes, a metallic NP, inducing the LSPR (Figure 3A), the absorbed light energy promotes electrons to an excited state above the metal Fermi level, changing the conduction band population distribution. The interaction of hot-electrons with the NP lattice takes place after a few ps and corresponds to the internal electron-phonon characteristic relaxation time (τ_{ep}), leading to NP temperature increase as depicted in Figure 3B. Within the thermal relaxation time (τ_d), thermal energy is released to the surrounding medium, mainly by a conductive contribution, causing the NP to act as a nanoheater, as shown in Figure 3C. The thermal relaxation characteristic time of a metallic NP is associated to its size and is described by [82]:

$$\tau_d = \frac{\rho_{np} c_{np}}{3\kappa_m} R_{eq}^2, \tag{2.22}$$

in which R_{eq} is the equivalent radius of a sphere with the same volume of a metallic NP of arbitrary shape, ρ_{np} and c_{np} are, respectively, the density and specific heat capacity of the NP and κ_m is the thermal conductivity of the surrounding medium. In water, the metallic NP τ_d can reach up to a few nanoseconds [83].

On selecting metallic nanoparticles for thermal applications, structures with a high absorption cross section are desired. High σ_{abs} values may lead to significant light energy absorption, and therefore increased NP temperature. In general, increasing the size of plasmonic particles enhances not only the absorption cross section, but the scattering cross section (σ_{sca}) value also rises, which indicates, for larger NP sizes, that the energy is strongly scattered to the NP surroundings. The Photothermal Conversion Efficiency (η) is an important figure of merit (FoM) for the evaluation of optical heating performance by NPs [13,85], defined as the ratio of absorption to extinction cross section, i.e.:

$$\eta = \frac{\sigma_{abs}}{\sigma_{ext}} = \frac{\sigma_{abs}}{\sigma_{sca} + \sigma_{abs}} . \tag{2.23}$$

Equation 2.23 quantifies the portion of the incident EM field absorbed by the NP. Usually, small plasmonic NPs are very efficient optical couplers, absorbing the incident light with barely

Figure 3 – Photothermal timescales for metallic NPs, from **A.** plasmon excitation with promotion of free carriers (fs) and **B.** electron−phonon relaxation (ps), to **C.** heat exchange with the surrounding medium (ps to ns).

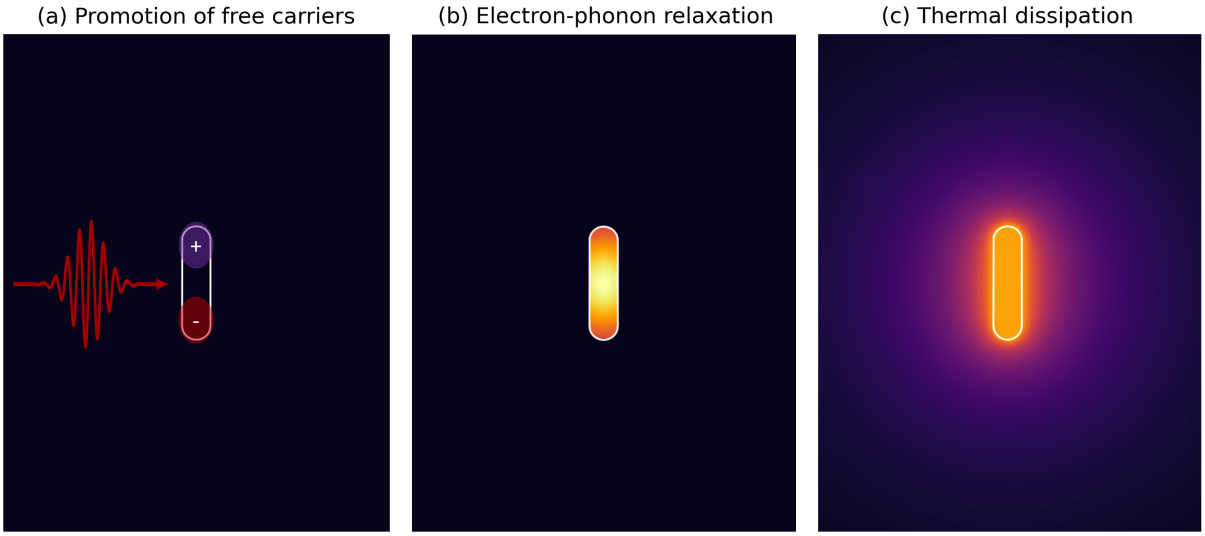

Source: adapted from Pedrosa, Farooq e Araujo[84].

any scattering. As the particle grows bigger, both the absorption and scattering increase. However, for larger particles, the scattering process starts to dominate light-NP interaction.

2.6 OPTIMIZATION METRICS FOR NANOPARTICLE MEDIATED HEAT GENERATION

Under fs pulse illumination, the pulse duration is roughly 10 times shorter than the electron–phonon relaxation time and if the pulse repetition period is longer than τ_d, the power delivered by the pulse is absorbed before the energy starts to be transferred from the hot-electron cloud to the NP lattice [5]. The change in temperature over time (ΔT_{np}^{fs}), driven by fs laser absorption and heat conduction to the surrounding medium over a timescale τ_d, is given by:

$$\rho_{np} c_{np} \frac{\partial}{\partial t} \left[\Delta T_{np}^{fs}(t)\right] = \kappa_{np} \nabla^2 \left[\Delta T_{np}^{fs}(t)\right] + \dot{Q}_{in}(t) - \dot{Q}_{out}(t) \ . \tag{2.24}$$

The energy balance of the system is given by the difference between the power source density ($\dot{Q}_{in}$) and the power loss density ($\dot{Q}_{out}$), and κ_{np} is NP thermal conductivity. Considering a uniform temperature distribution inside the NP, the Laplacian of the temperature change is null. The power source density is the heat power transferred from the electron gas to the atomic lattice of the nanoparticle, which is highly dependent on laser pulse duration. If the laser pulse is shorter than the electron-phonon relaxation, the power source density is given by [5]:

$$\dot{Q}_{in}(t) = \frac{\sigma_{abs} \langle I \rangle}{f \tau_{ep} V_{np}} \ e^{-t/\tau_{ep}} \ . \tag{2.25}$$

Here, $\langle I \rangle$ denotes the average pulse irradiance, f is the laser repetition rate and V_{np} is the NP volume ($V_{np} = \frac{4}{3}\pi R_{eq}^3$). For gold NPs, $\tau_{ep} \sim 1.7$ ps [5]. Following the transient heat conduction, the power loss density is driven by conductive contributions in the NP outward direction that is proportional to the temperature difference between NP and medium temperatures (that is the same as $\Delta T_{np}^{fs}(t)$):

$$\dot{Q}_{out}(t) = \rho_{np} c_{np} \frac{\Delta T_{np}^{fs}(t)}{\tau_d} . \tag{2.26}$$

An analytical expression is derived from Equation 2.24 for the temperature increase of a single NP, if no phase transitions are involved in the process:

$$\Delta T_{np}^{fs}(t) = \frac{\langle I \rangle}{\rho_{np} c_{np} f \left(1 - \tau_{ep}/\tau_d\right)} \frac{\sigma_{abs}}{V_{np}} \left[e^{-t/\tau_d} - e^{-t/\tau_{ep}} \right]. \tag{2.27}$$

Figure 4 shows the temperature dynamics of different AuNRs of sizes 40 $\times$ 10 (solid line), 90 $\times$ 25 (dot-dashed line) and 134 $\times$ 40 nm (dashed line), all of which have LSPR around 800 nm. Increasing NP volume leads to longer relaxation times and lower temperature build up. The material parameters used were κ_m = 0.59 W/(m ^{o}C), c_{np} = 129 J/(kg ^{o}C) and ρ_{np} = 19320 kg/m^3 [5], while laser parameters were f = 80 MHz and $\langle I \rangle$ = 10 W/mm^2. The absorption cross sections were extracted from FEM simulations.

Under pulsed illumination, the maximum temperature change is not only localized in space, but also in time, as the heat front diffuses away from the NP surface. On this basis, the average temperature of a single NP under fs laser pulses is obtained by taking the average integral over the laser repetition rate period ($\langle \Delta T_{np}^{fs} \rangle = f \int_t^{t+1/f} \Delta T_{np}^{fs}(t')dt'$). Therefore, the NP average temperature is given by:

$$\langle \Delta T_{np}^{fs} \rangle = \frac{\langle I \rangle \tau_d}{\rho_{Au} c_{pAu}} \frac{\sigma_{abs}}{V_{np}} \left[1 - \frac{e^{-1/f\tau_{ep}}}{1 - \tau_{ep}/\tau_d} \right]. \tag{2.28}$$

The ability of a NP to lose heat to its surroundings is related to its surface area and volume. To grant efficient heat loss, the volume must be minimized, while surface area must be maximized. Thus, NP morphology becomes relevant to thermoplasmonic applications. An effective way to evaluate the ability of a NP to generate heat is exploring the Joule number (Jo) [86], given by:

$$Jo = \frac{\lambda_{ref}}{2\pi} \left(\frac{\sigma_{abs}}{V_{np}} \right) , \tag{2.29}$$

Figure 4 – Temperature increase of different AuNRs of sizes 40 × 10 (solid line), 90 × 25 (dot-dashed line) and 134 × 40 nm (dashed line) for f = 80 MHz and $\langle I \rangle$ = 10 W/mm^2.

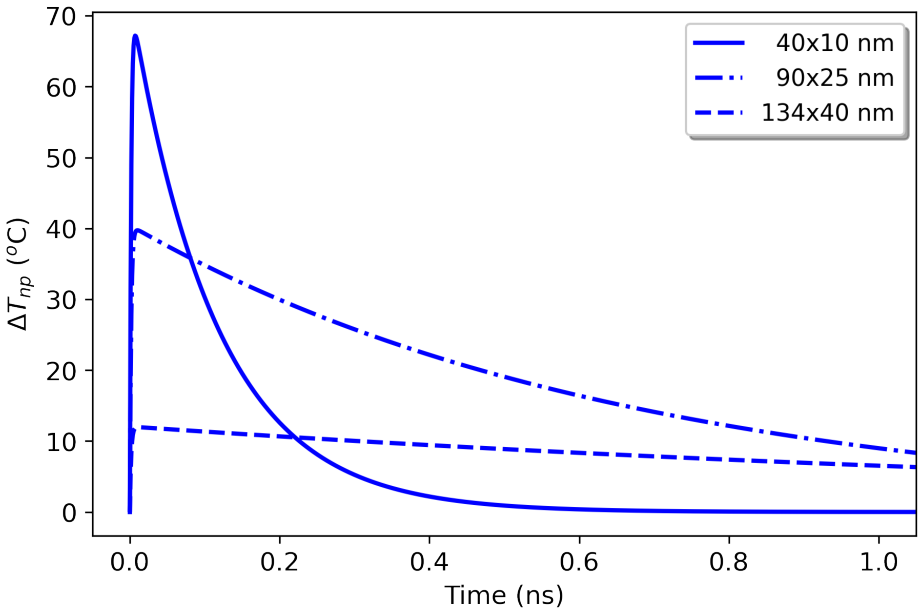

Source: belongs to the author.

in which $\lambda_{ref} \approx 1240$ nm is the reference wavelength of a photon with energy of 1 eV. Temperature variation is directly proportional to the ratio of its absorption cross section to volume ($\Delta T_{np}^{fs} \propto \sigma_{abs}/V_{np}$). Comparing Equations 2.29 and 2.27 it is noticeable that $\Delta T_{np}^{fs} \propto Jo$. Hence, Jo arise as the ideal FoM to assess temperature variation in single NPs induced by fs pulses. Moreover, depending on NP size, this can be extended to pulses up to tens of ns, regarding that most of the pulse energy is absorbed before thermal diffusion becomes effective. If a train of fs pulses is used to induce photothermal conversion in a NP, the temporal profile described by Equation 2.27 is replicated after each pulse. If the laser repetition period $(1/f)$ is longer than τ_d, there is no initial cumulative heating in the NP. However, since the thermal diffusivity of water is much smaller than gold, heat diffuses slower in water. Although such behavior is insufficient to support cumulative heating from a single nanostructure perspective, the superposition of heat generated by many nanoheaters favors large temperature changes in macroscopic media [83].

However, the plasmonic heating induced by pulsed lasers and CW sources are governed by distinct dynamics, and therefore, the features of the excitation source should also be considered to identify efficient nanoheaters [84,87]. For continuous excitation, energy absorption and conductive transport of heat to the surrounding medium happens concurrently, leading to lower temperature rises. A generalized expression for the steady-state temperature change for a NP of arbitrary shape is given by [88]:

$$\Delta T_{np}^{CW} = \frac{I}{4\pi\kappa_m}\frac{\sigma_{abs}}{R_{eq}\beta}\ , \tag{2.30}$$

in which β is the shape-correction factor. For AuNRs, β is a function of the AR and is given by $1 + 0.096587\ \ln^2(\mathrm{AR})$ [88]. The shape factor β, the absorption cross section and the equivalent radius are all a function of NP shape. Therefore, changes in NP dimension may increase or reduce the steady-state temperature achievable. Following Equation 2.30, a new FoM, the Steady-state factor, was defined as [84,87]:

$$S^2F = \frac{\sigma_{abs}}{R_{eq}\beta}\ . \tag{2.31}$$

Each NP shape will provide a different value for J_o and S^2F. Similarly, sweeping NP size leads to changes in absorption cross section and volume, as the former grows quadratically with size while the latter is related to its cube. The difference in growth rates may lead to the emergence of optimal NP size where V_{np} growth overcomes σ_{abs} growth. This optimal size is a turning point in which absorption dominated interactions become scattering dominated and can be used to delineate the regime in which the NP operates (good absorber vs good scatter). Another factor that weights in the final temperature of the NP is the thermal diffusivity of the surrounding medium. As it describes the rate of heat transfer inside a material, media with lower thermal diffusivity have less efficient heat exchange with heating NPs, which contributes to higher NP temperature increases.

Several applications that rely on photothermal conversion demand temperature increase at the macroscopic scale. It is, therefore, relevant to investigate the effect of NP optimization under collective heating. Considering a medium containing multiple plasmonic NPs excited by a laser (pulsed or CW), the total global temperature change is given by the superposition of each individual NP in the steady state [83]:

$$\Delta T_{global} = \sum_{n=1}^{\#_{np}} \Delta T_{np}^{(n)}. \tag{2.32}$$

Here, $\#_{np}$ is the total number of NPs and n is the n$^{\text{th}}$ NP of the sample. Supposing the thermal contribution is the same for all NPs, the summation can be replaced by a volume integral over th e illuminated region (V') with constant volumetric density of NPs (C_{np}). From Equations 2.28 and 2.30 it follows that the collective heating for each case becomes:

$$\Delta T_{global}^{fs} = C_{np}\langle\Delta T_{np}^{fs}\rangle V_{np}\left(\frac{3}{4\pi}\int_V \frac{dV'}{{r'}^3}\right) \quad \text{and} \tag{2.33}$$

$$\Delta T_{global}^{CW} = C_{np} \Delta T_{np}^{CW} R_{eq} \left(\int_V \frac{dV'}{r'} \right). \tag{2.34}$$

Qualitatively, the global temperature change is proportional to $C_{np}\Delta T_{np}$, which, in turn, is proportional to $C_{np}\sigma_{abs}$ in both cases. Considering a colloid of gold NPs with volume fraction p, one can infer that:

$$\Delta T_{\mathrm{global}} \propto p \left(\frac{\sigma_{abs}}{V_{np}} \right). \tag{2.35}$$

Therefore, for collective heating, the change in global temperature is proportional to NP Joule number ($\Delta T_{\mathrm{global}} \propto J_{\mathrm{o}}$). Nevertheless, for thick or very concentrated samples (large C_{np}), most of the energy delivered will be absorbed independent of the sample absorption cross section. Furthermore, the described FoM are limited to NPs that doesn't have radiative transitions. Yet, the FoM may be modified to accommodate NPs with radiative properties, such as semiconductor NPs and quantum dots. This is beyond the scope of this work and will not be discussed.

3 NANOHEATER OPTIMIZATION

Many groups have been working on different methodologies to prepare NPs of various structures, leading to high optical cross sections and tunable plasmon spectrum at the visible and near-infrared (NIR) band. However, optical therapies raise concerns regarding accessibility from a clinical standpoint. For instance, skin exposure to laser radiation at 1064 nm is limited to 100 mJ/cm^2 for pulses shorter than 100 ns and 1 W/cm^2 for continuous wave (CW) illumination [26]. Simultaneously, for 514 nm, exposure is limited to 20 mJ/cm^2 for pulses shorter than 100 ns and 0.2 W/^{o}C for CW irradiation. Therefore, in photothermal therapy assisted by plasmonic particles, the use of high-performance metallic nanoheaters may lead to: (i) the reduction of NP concentration used; and (ii) the reduction of light fluence.

For the purposes of this work, the optimization procedure was carried out for AuNSs and AuNRs. Obtained optimization results were later explored in various photothermal applications.

3.1 MATERIALS AND METHODS

3.1.1 Computational analysis

The optimization methodology follows a theoretical approach using Mie Theory or FEM to compute the optical cross sections of AuNSs and AuNRs in aqueous medium. The size dependent optical cross sections are then converted into the respective FoM (J_o and S^2F), providing the curves and colormaps that correlate the FoM to the NP dimensions. This method provides a simple yet effective way to identify the optical heating performance of size dependent NPs.

AuNSs with different sizes are well explored as nanoheaters for thermal applications, and their optical properties have been demonstrated to rely on their size. Gold nanoparticles with small dimensions primarily absorb light around 524 nm, whereas larger nanoparticles demonstrate increased light scattering and have peaks that broaden considerably and shift towards longer wavelengths. The absorption and scattering cross sections of AuNSs were obtained using Mie Theory. The NP diameter was varied from 5 to 100 nm for spectroscopic analysis and the permittivity values of gold were extracted from Johnson & Christy [47]. To validate the computational procedure, the results were thoroughly evaluated by comparison with reports in the existing literature [89].

The plasmonic properties of AuNRs were appraised by means of FEM electromagnetic simulations in COMSOL Multiphysics, in which a single AuNR of length *L* and diameter *D* was placed in a dielectric medium (water). The NR longitudinal axis was aligned with the polarization of incident light. The surrounding medium refractive index was assumed to be wavelength independent and bounded by a perfectly matched layer (PML) with spherical

symmetry, mimicking an open boundary and avoiding the reflection of scattered light, as seen in Figure 37 (Appendix B). NR length L was swept from 15 nm up to 200 nm for a set AR. The process was extended for various AR values. The results obtained from FEM simulations were validated by comparison with Mie–Gans theory, using few NR structures with different AR [90].

3.1.2 Photothermal evaluation of AuNS samples

Theoretical results of the optimization model were experimentally verified using thermal lens (TL) in investigations conducted by Prof. Georges Boudebs at the University of Angers. Colloidal samples of monodispersed citrate-stabilized AuNSs (less than 12% variability in size and shape) were acquired from Sigma-Aldrich (Missouri, EUA) with diameters of 5, 50 and 100 nm. The samples were prepared to have the same gold mass concentration (17.4 ± 1.2 mg/L) and collective heating of AuNS samples was evaluated under CW laser irradiation [87]. The experimental measurement system integrated a Z-scan setup, where the sample were moved along the propagation z-axis of the modulated laser beam, with a TL detection mode, as depicted in Figure 5. In short, the setup explored a chopped 532 nm laser (Oxxius, LCX-532S) and a photodiode connected to a digital storage oscilloscope. The colloid was contained in a 1 cm cuvette placed at a translational stage. The measured signal allowed to estimate the temperature of the sample [87].

Figure 5 – Z-scan setup in TL detection mode. The cell is positioned within the beam's Rayleigh length after passing L1 and the signal is measured in the far-field by PD.

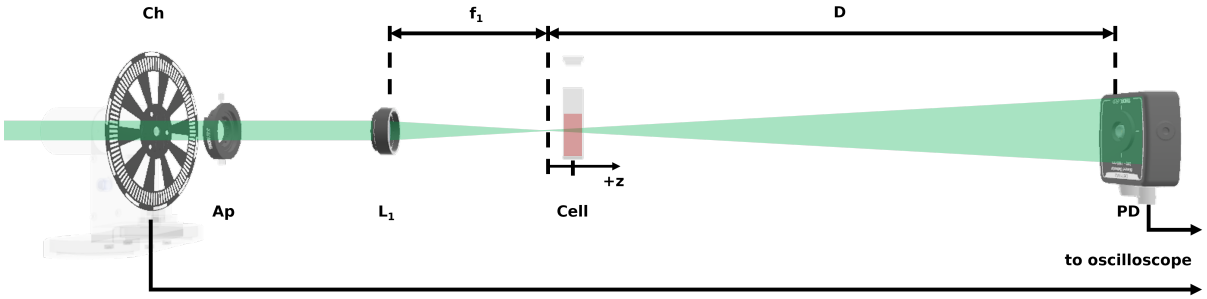

Source: belongs to the author.

3.1.3 Thermal evaluation of AuNR samples

Cetyltrimethylammonium bromide (CTAB)-stabilized colloidal samples of AuNRs in deionized water with sizes 41×10 nm, 90×25 nm and 134×40 nm were acquired from Nanopartz Inc. (Loveland, Colorado). All samples were diluted in distilled water to produce samples of same NP volumetric density (10^{15} m^{-3}). The thermal evaluation setup comprised of a pulsed laser (Coherent Chameleon Vision II, 140 fs, 80 MHz), one spherical lens and one cylindrical lens arranged to produce a light sheet in order to illuminate the specimen contained in the cuvette thoroughly and promote homogeneously temperature increase. The colloidal specimens are placed in a 2 mm cuvette and temperature evolution is appraised in real-time using

thermal camera (Flir E4; Flir, Wilsonville, OR). The thermal camera is adjusted to acquire the average temperature of the illuminated sample and compensate for ambient temperature change. Figure 6 illustrates the experimental setup for the appraisal of collective heating by colloidal sample of NPs. The fs laser source is omitted. This step has already been completed.

Figure 6 – Experimental detail picturing the light sheet optics and sample positioning for temperature acquisition.

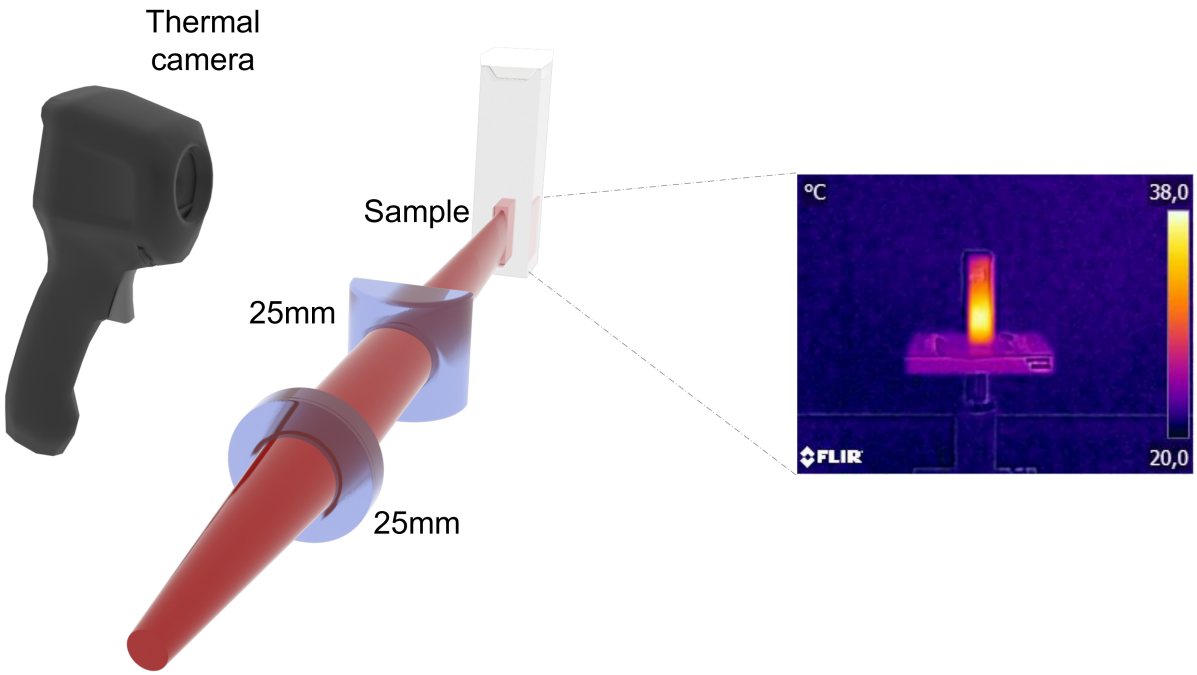

Source: belongs to the author.

3.2 RESULTS AND DISCUSSIONS

The samples were subjected to UV-Vis spectroscopy and scanning electron microscope (SEM). Figures 7A and 7B show the normalized extinction spectra of the AuNS (blue) and AuNR (red) samples, respectively. Figures 7C and 7D depict, respectively, AuNSs of diameter 50 and 100 nm, whereas Figures 7E to 7G illustrate AuNRs of size 41×10, 90×25 and 134×40 nm. The SEM of the 5 nm sample is absent since it is too small to be resolved by SEM. The red-shift in the extinction spectra seen for 100 nm AuNSs (Figure 7A) is produced by dephasing mechanisms mentioned in Chapter 2. It's important to allude, however, that for larger diameters the extinction red-shift is dominated by the red-shift observed for the scattering cross section, while the absorption cross section peak barely move.

Equations 2.24 and 2.30 indicate J_o and S^2F size dependence for a single NP. Figure 8 depicts $\mathrm{J_o}$ and $\mathrm{S^2F}$ values for AuNSs of different sizes (diameter), considering their maximum

Figure 7 – Characterization of gold colloidal samples. **A.** Normalized exctinction of AuNSs of size 5, 50 and 100 nm (UV-Vis). The vertical dashed line marks λ = 530 nm. Normalized extinction of **B.** Normalized exctinction of AuNRs of size 41×10, 90×25 and 134×40 nm (UV-Vis). The vertical dashed line marks λ = 808 nm. **C.** 50 nm AuNS (SEM). **D.** 100 nm AuNS (SEM). E) 41×10 nm AuNR (SEM). F) 90×25 nm AuNR (SEM). G) 134×40 nm AuNR (SEM). The scale bar is 100 nm for AuNSs and 20 nm for AuNRs.

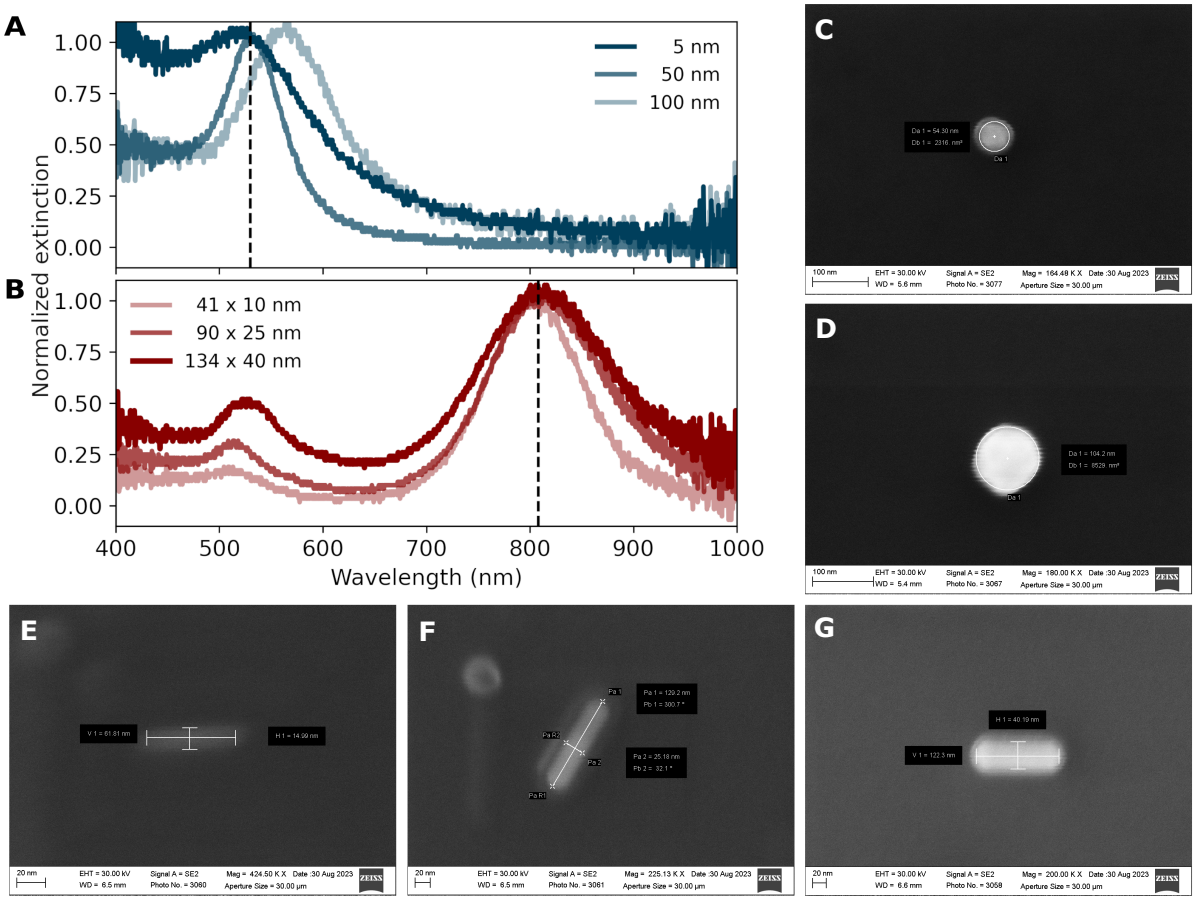

Source: belongs to the author.

absorption cross section at the plasmonic peak in water. According to Figure 8, when exposed to short pulse illumination, smaller particles are better suited for attaining higher temperatures compared to larger structures (blue line). The J_o of the nanospheres of diameters 5 nm and 50 nm are approximately two times higher than those of 100 nm nanospheres. Differently, under CW illumination, S^2F values (red line) indicate that single particles with large sizes can reach higher temperatures than smaller nanospheres when considered for single particle heating. In this case, the 100 nm AuNS shows a higher S^2F value than 5 nm and 50 nm NP.

TL technique was explored to identify micro-degree temperature changes of laser heated colloidal gold nanospheres on the selected samples (diameters of 5, 50 and 100 nm). The experimental approach relies on the assessment of the spatial temperature profile within a volume that is subjected to laser heating to establish the collective temperature rise (ΔT_{global}). It was

Figure 8 – Gold nanosphere J_o (blue) and S^2F (red) values, as function of the NP diameter, obtained by Mie theory (in water).

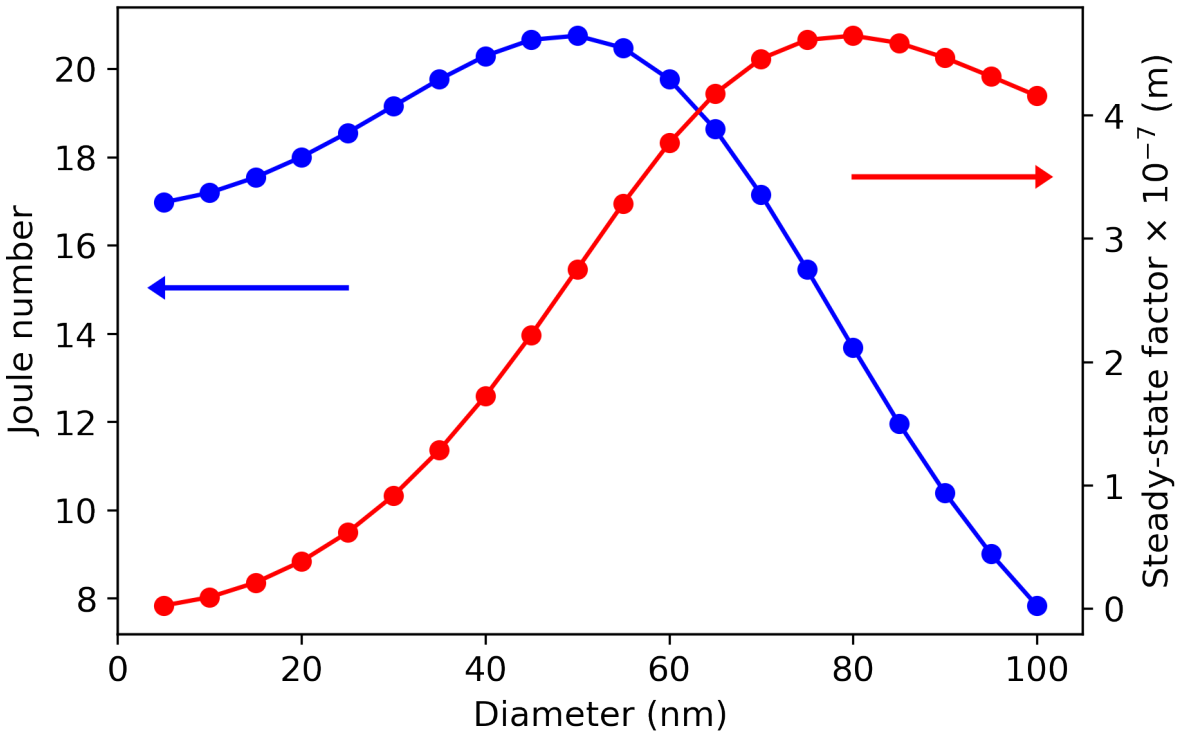

Source: adapted from Pedrosa, Boudebs e Araujo[87].

observed that experimental collective temperature rise resembles J_o behavior. However, the proposed thermal lens technique enabled the estimation of temperature rise for a single NP, which was shown to resemble the behavior of S^2F. Figure 9 illustrates single AuNS temperature rise estimates for 1.33 mW laser power. The collective temperature rise is then used to infer temperature increase for of individual NPs in the scenario where there is only a single NP present (intermediate steady-state) [91]:

$$\frac{\Delta T_{\text{global}}}{\Delta T_{np}} = \pi w_0^2 \, C_{np} R_{eq} \ln\left(\frac{2\ell}{w_0}\right). \tag{3.1}$$

Here, a vessel of optical path ℓ containing colloidal NPs were heated by a laser beam that illuminates a cylindrical volume of length ℓ and radius w_0 ($\ell \gg w_0$). The relation between collective and single NP temperature rise was also revealed by Equations 2.33 and 2.34.

Figure 9A indicates that the highest ΔT_{np} are achieved for larger particles. The result is compared against calculated S^2F for different AuNS sizes. Figure 9B depicts ΔT_{np} achieved for different excitation powers. Higher laser power leads to higher temperatures, maintaining the size-related behavior. Consequently, for single NP, optimal heating under CW illumination in aqueous medium is achieved at 80 nm diameter [87].

Figure 9 – **A.** Experimental (black) and theoretical (red) S^2F and single AuNS temperature rise as function of diameter (illuminated with 1.33 mW laser power). **B.** Experimental intermediate steady-state temperature variation for different excitation powers, considering 5, 50 and 100 nm diameter AuNSs.

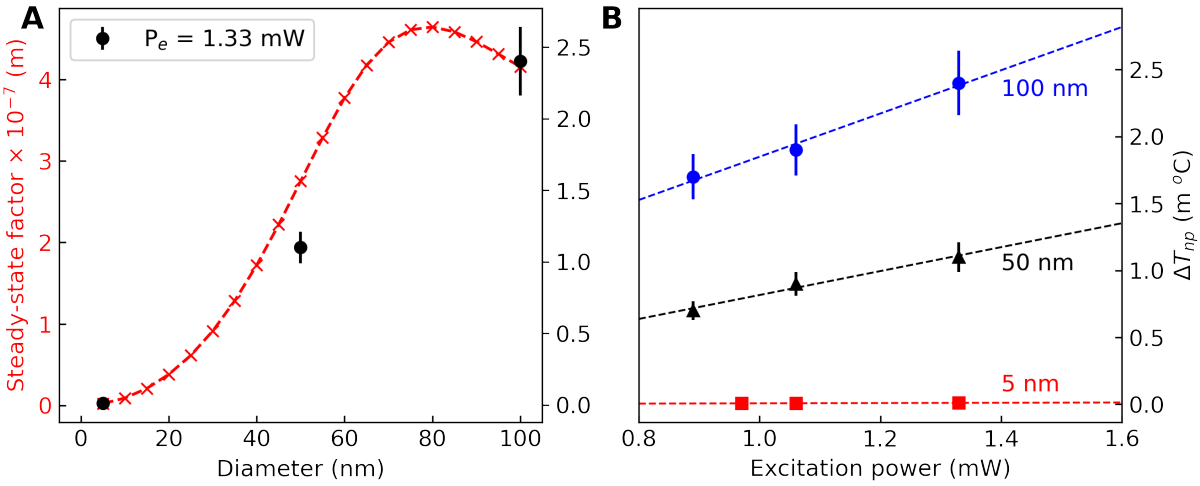

Source: adapted from Pedrosa, Boudebs e Araujo[87].

Following the proposed optimization procedure, the thermo-optical properties of AuNRs of various lengths and diameters are depicted in Figure 10. Figure 10A depicts a single AuNR of length L and diameter D. The colormap in Figure 10B delineates LSPR position (λ_p) as function of NR length and diameter. For all colormaps of Figure 10 the dashed and dash-dotted lines represent the AuNR sizes at which λ_p occurs for ∼800 nm and ∼1064 nm, respectively. The wavelengths 800 nm and 1064 nm correspond to important laser lines within the first and the second biological NIR transparency window. By changing the particle size and keeping AR constant, the LSPR barely moves for AuNRs of diameter smaller than 25 nm. Therefore, for bigger NRs, the dashed and dash-dotted lines start to bend due to dephasing effects on the conduction electrons and the LSPR position is red-shifted [92]. To obtain the AuNR diameter, we must explore the colormaps in conjunction with the FoM curves as function of AuNR length. Figures 10D, F and G allows the identification of the AuNR length associated with the highest FoM values. In order to obtain the AuNR diameter, the colormaps of Figures 10 (C, E and G) must be explored. Notice that the dashed-dotted and the dashed lines on colormap corresponds to the ordered pair (diameter, length) at which all the AuNRs have LSPR fixed at the same wavelength (800 nm for the dashed line and 1064 nm for the dashed-dotted line). Hence, for a fixed wavelength, only one AuNR length is related to one AuNR diameter.

Figure 10C shows the colormap for the Photothermal Conversion Efficiency of AuNRs. Large values of η are obtained for AuNRs with diameter smaller than 50 nm. Nevertheless, η values becomes smaller for increasing NR volumes, the overall absorption and scattering cross sections rise, and σ_{sca} overcomes σ_{abs}. Figure 10D depicts the decreasing behavior of η as the size of the NP, with resonance at 800 nm (blue) and 1064 nm (orange), is increased. Therefore, it

Figure 10 – **A.** Scheme of an AuNR and its dimensions. **B.** LSPR colormap as a function of AuNR length and diameter. **C**, **E**, **G.** Colormaps for η, J_o and S^2F, respectively, for various AuNR dimensions. The outlined dashed and dash-dotted curves in all colormaps depict AuNR dimensions in which the plasmon peak occurs for 800 nm and 1064 nm, respectively. **D**, **F**, **H.** Evolution of η, J_o and S^2F as a function of AuNR size. The blue curves represents AuNR sizes with LSPR in 800 nm, while the orange curves portrays AuNR sizes with LSPR in 1064 nm.

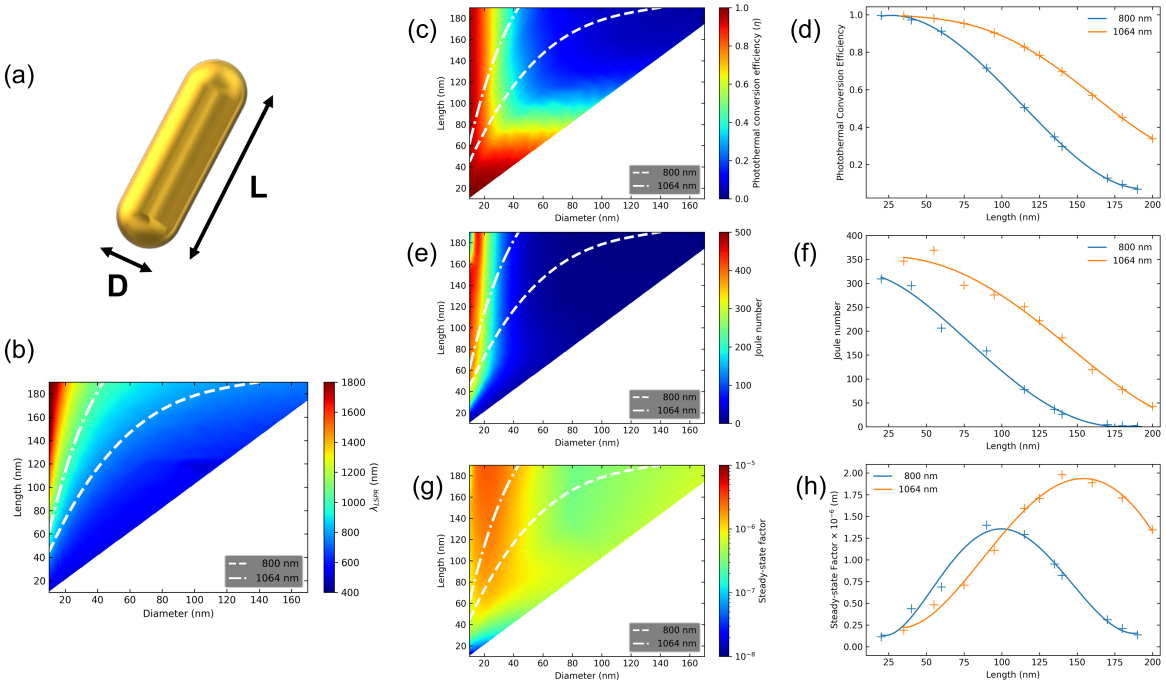

Source: adapted from Pedrosa, Farooq e Araujo[84].

is compelling to think that smaller-size particles are preferable for heat generation. Figure 10E is the Joule number colormap for AuNRs in water. One can observed that particles with diameter smaller than 30 nm show high J_o. As stated previously, the capacity of an NP to convert light into heat is proportional to σ_{abs} and inversely related to its volume. As the particle grows bigger, so do both contributions. However, σ_{abs} and volume grow at different rates, which leads to a reduction of Jo values as the NR increases. Figure 10F outlines Jo values as function of AuNR length in water for the traces at which λ_p are 800 nm and 1064 nm. J_o follow a trend similar to η, where smaller NP sizes are more efficient for photothermal conversion. This is different to what was observed for AuNSs (Figure 8, blue line).

Figure 10G illustrate the S^2F colormap for AuNRs in water, while Figure 10H outlines S^2F as function of AuNR length for the inset traces. The reddish-colored area of Figure 10G indicates that high S^2F is obtained for particles of long length (larger than 60 nm) and short diameter (smaller than 40 nm). On defining S^2F, the NP size dependence is represented by the equivalent radius, while shape dependence is introduced by the shape factor β. The dashed and dashed-dotted lines in Figure 10H show that the best AuNR for single-particle CW photothermal conversion at 800 nm and 1064 nm in water are, respectively, $\sim$90 $\times$ 25 nm and $\sim$150 $\times$ 30

nm. Our results show that S^2F values tend to peak. Differently to Jo, where smaller AuNRs are better, S^2F maximum occurs at longer AuNR lengths (and diameters), indicating that on engineering plasmonic nanoheaters for single NP illumination, it is important to consider the illumination regime (pulsed or CW)[1].

Thermal imaging was used to appraise the collective heating of CTAB-stabilized colloidal AuNR samples of sizes of 41 $\times$ 10, 90 $\times$ 25 and 134 $\times$ 40 nm under 808 nm laser irradiation. Experimental results shows that if the same total mass of gold is used (among different samples), the collective heating follows the trend of the J_{o} [84].

Notwithstanding the 134 $\times$ 40 nm sample enabling higher temperature rise in the reported experimental arrangement, when the amount of gold is the same for different specimens of distinct AuNR sizes, the final global temperature weighed by the total Au mass becomes proportional to Joule number ($\Delta T_{\mathrm{global}}/M_{\mathrm{tot}} \propto J_{\mathrm{o}}$). The experimentally appraised collective temperature rise were contrasted with the total mass of gold present in each specimen, and the result is displayed in Figure 11A. In parallel, by dividing the total temperature rise by the total number of NPs in each sample, temperature rise tends to follow the AuNR absorption cross section ($\Delta T_{\mathrm{global}}/NP \propto \sigma_{abs}$), as shown in Figure 11B. Therefore, the choice of the best AuNR size for temperature rise under collective heating depends on the circumstances delineated by the application. If the same mass of material is considered, the FoM of choice is Jo. In turn, if the application concerns the same number of NPs, absorption cross section must be maximized [84].

Figure 11 – **A.** Experimental global temperature rise divided by the total mass of gold of each sample (red dashed line). For the same amount of gold, the total temperature rise follows Joule number (blue line). **B.** Measured global temperature rise divided by the total number of NPs in each sample (red dashed line). For the same number of NPs, the total temperature rise follows absorption cross section (blue line).

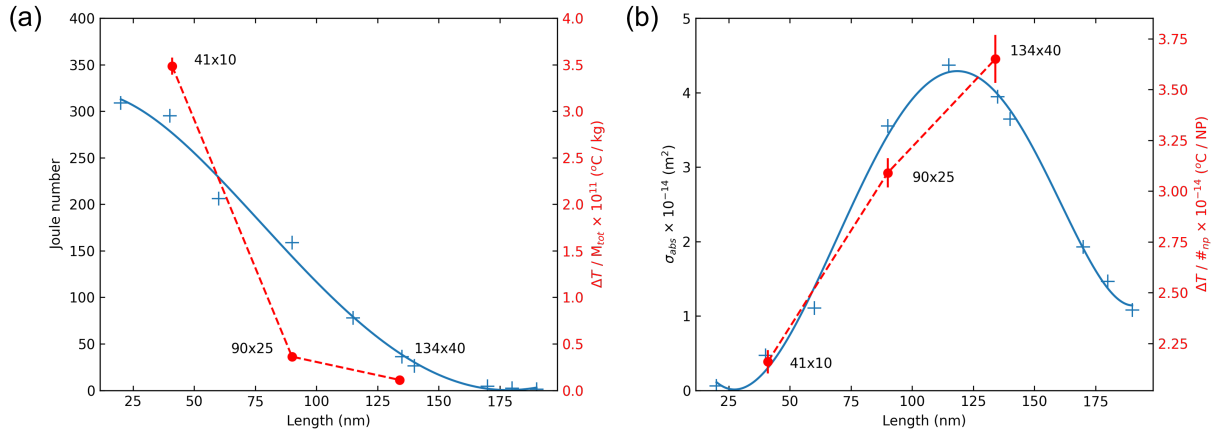

Source: adapted from Pedrosa, Farooq e Araujo[84].

Table 2 summarizes optimal AuNS and AuNR of different sizes embedded in aqueous medium. Joule number and Steady-state factor are the FoM considered.

[1] Theoretical results obtained during my master's degree.

Table 2 – Optimal AuNSs and AuNRs sizes in aqueous medium for different wavelengths.

	AuNS (530 nm)	**AuNR (808 nm)**	**AuNR (1064 nm)**
J_{o}	50 nm [87]	Smaller is better [84]	Smaller is better [84]
S^2F	80 nm [87]	90×25 nm [84]	150×30 nm [84]

3.3 CONCLUSIONS

A framework for the optimization of metallic NPs for heat generation was established and FoM were described for the optimization of heat generation: (i) the Joule number (J_{o}) for pulsed and cumulative heating and (ii) the Steady-State Factor (S^2F) for CW irradiation in the context of an isolated single NP. Both FoM are adequate for most metallic NP shapes and AuNSs and AuNRs were chosen for experimental assessment.

For AuNSs, theoretical analysis and thermal lens measurements allowed the identification of micro-degree temperature increase of laser heated colloidal samples of varying sizes. The measurements show that the achieved TL global temperature resembles J_{o} behavior, and the optimal AuNS diameter for efficient colloidal laser heating in water was identified to be 50 nm. TL technique also enabled the estimation of intermediate steady-state temperature of a single particle, which was shown to resemble S^2F behavior with maximum performance expected for a radius of 80 nm. Additionally, the optimal dimensions of AuNRs in aqueous medium were obtained for different laser lines (808 and 1064 nm). In particular, J_{o} indicate that smaller AuNR sizes are more efficient for photothermal conversion. Nevertheless, for single AuNR, S^2F suggests that optimal performance is achieved for samples of size 90×25 and 150×30 nm for 808 and 1064 nm, respectively. The effect of such optimizations in collective heating was also discussed and the experimental results obtained using thermal imaging show that if the same total mass of gold is used, collective heating follows the trend of the J_{o}. However, if the total number of NPs is the same among different samples, temperature increase is governed by absorption cross section.

Moreover, the rules of using FoM to select efficient plasmonic nanoheaters were revealed and size dependence of plasmonic NP optical heating was disclosed. In this sense, the following chapters explore the optimization methodology and compares the performance of optimal and sub-optimal NPs for different applications.

4 PHOTOINACTIVATION OF CANDIDA ALBICANS AND PHOTOTHERMAL THERAPY IN MICE

Photothermal processes have proven effective in controlling microbial infections and cancer cells. Here we propose the use of selected nanoheaters to improve the efficiency of fungal photothermal inactivation and photothermal therapy of tumors. Localized surface plasmon resonance phenomena in metallic NPs may be explored as an alternative strategy to achieve more efficient localized heating, and this study demonstrates the use of optimized plasmonic AuNRs to enhance the performance of photothermal inactivation of *Candida albicans* and photothermal therapy in Murine Sarcoma 180 in animal model. Here, the optical heating of polyethylene glycol coated AuNRs of varying sizes is experimentally evaluated following the size dependent computational approach applied to identify metallic nanorods with maximized thermal performance described in the previous chapter. The identification of high performance metallic nanoheaters may lead to the reduction of the NP dose used in plasmonic-based procedures.

In this chapter, we assess the perspectives of using optimized AuNRs following a NP size dependence approach for photothermal inactivation of *Candida albicans* and photothermal therapy in S180-bearing mice.

4.1 INTRODUCTION

The use of well-founded methods to select efficient plasmonic particles for photoinactivation of microorganisms are still scarcely explored. The electric field damping induced by LSPR can increase PTI activity. Despite several studies combining therapeutic modalities for the treatment of bacterial infections and increasing antimicrobial efficacy of treatments [93–95], as well as studies approaching the photothermal inactivation of yeasts [14,96–98], it is still necessary to establish procedures and inputs that enable the effective action of PTI on fungi.

The progressive increase in fungal infections in health care institutions corresponds to serious public health problem, being associated with high rates of morbidity and mortality [99,100]. This situation worsens with the increase in yeast resistance to antifungal agents, resulting in therapeutic failures and increased difficulty in combating invasive infections. In this sense, the emergence of a wide variety of pathogens resistant to chemical agents has attracted the attention of the antimicrobial chemotherapy industry. In particular, *Candida* species represent almost 90% of fungal pathogens responsible for fungal infections in general, and 8% of nosocomial bloodstream infections [101]. *Candida albicans* is the most predominant Candida species associated with yeast infections, being responsible for 65.3% of candidiasis [101]. *Candida albicans* is a fungus that is among the many organisms that inhabit the human body, and their presence under normal circumstances do not induce harmful health effects. However, population imbalance (excess) of this fungus results in candidiasis, which promote serious oral and vaginal infections in patients

with immunosuppressive diseases, such as AIDS, who are hospitalized in an intensive care unit or undergoing chemotherapy. The search for alternative procedures for the localized treatment of candidiasis with the least possible side effects, is a topic of relevant medical interest [22,102].

In contrast, the use of photothermal processes for the treatment of cancer has been widely investigated [103,104]. Traditional cancer therapies rely on chemotherapy and radioactive inactivation of tumorous cells, techniques that have been proven effective, albeit the collateral effects that arise from it [13]. As an alternative, Photothermal Therapy rely on locally induced hyperthermia to destroy tumor cells, thus, efficient photosensitizers must be administrated to obtain better therapeutic outcomes. Gold NPs such as nanospheres [105,106], nanoshells [107], nanorods [108–112], nanocubes [113,114], nanohexapods [109] and nanourchins [115] have been tested in a variety of photothermal cancer interventions. For instance, thermal based treatment of oral [110] and colon [105,111] carcinomas in mice were appraised and gold nanocages have also been effectively employed for selective photothermal destruction of breast cancer in vitro [113] and in vivo [114]. Photothermal treatment using different gold NPs for the treatment of melanoma in tumor-bearing mice [109,112] and breast cancer [106,113,116] have also been evaluated.

One important concern on using NPs on PTT is the incorporation of the nanoheaters in the target tissue or cells. NP targeting to cancer cells can be either passive, involving the intratumoral administration of NPs being injected directly into the particular site of the tumor, or active, which involves functionalization that facilitates NP binding to tumorous tissues following intravenous administration [117]. NPs with diameters ranging from 50 and 800 nm are not capable of penetrating blood vessel walls, since the spacing between vascular endothelial cells ranges from 15 to 30 nm [117]. In tumorous tissues, however, the angiogenesis process is responsible for the promotion of rapid and irregular development of new blood vessels with spacing ranging from 200 to 2000 nm in the capillaries, depending on tumor type and localization [118]. Such large spacing allows the uptake of NPs into intercellular spaces, which leads, consequently, to the accumulation of NPs inside tumors [119]. Nevertheless, the concentration of NPs administered must not be too high due to the cytotoxicity of gold NPs [120,121]. More recently, studies of the interaction of gold NPs with lipid membranes revealed that NP diameter is decisive in determining the absorption of the NP by lipid bilayers. In essence, the absorption of NPs larger than 60 nm is greatly reduced, and the majority of the larger gold NPs stay free in solution [122], which greatly reduces NP uptake.

For in-vivo applications such as cancer treatment, selective killing of tumorous cells demands a system based on a carrier, usually a targeting ligand capable of attaching to a specific targeted tissue. Red blood cell membranes embedding NIR dye and camouflaging Mn-ferrite NPs have been used as theranostic nanocarriers to induce immunogenic cell death in the treatment S180-bearing mice [123]. Murine Sarcoma 180 (S180) is a cell line originating from Murine mouse. S180 cells grow very quickly, and within seven days of subcutaneous implantation, the tumor reaches approximately $15 \times 11 \times 8$ mm [124]. These cells are commonly used in experimental (pre-

clinical) studies related to cancer, with the aim of understanding the mechanisms of tumor growth, testing new therapies and evaluating the effectiveness of different therapeutic agents [125,126].

Issues concerning stability, biocompatibility and cytotoxicity of plasmonic NPs remain a barrier for their clinical use. Challenges resulting from the complexity of biological systems (penetration depth, NP uptake, accumulation, tissue specific targeting and precise heating control of photothermal processes) contribute to the variability of photothermal treatment and result in uncertain therapeutic effectiveness. Thus, regulatory entities such as the U.S. Food and Drug Administration (FDA) are critical in promoting the safe and responsible use of plasmonic materials. Most of the FDA approved gold NPs focus on their antimicrobial effectiveness against bacteria [127,128]. Two examples are gold-silica nanoshells (15 nm core) and gold nanospheres ranging from 23-52 nm loaded with Ciprofloxacin and Cefaclor, respectively, are used for treatment of *S. aureus* and *E. coli* [128].

Although the number of human trials based on gold NP formulations for photothermal applications is increasing, such systems are still scarce. Aurrimune, for instance, is a formulation containing 27 nm gold NPs, loaded with TNF-α (a group of cytokines capable of causing apoptosis in tumor cells and which have a wide range of pro-inflammatory actions) and PEG. It has been tested for late stage pancreatic, breast, colon, melanoma, sarcoma and lung cancer. Alternatively, Aurolase makes use of 150 nm silica-gold nanoshells coated with PEG and has been tested for refractory and/or recurrent tumors for head and neck cancer. Similarly, Sebacia Microparticles, a formulation containing 150 nm silica-gold nanoshells coated with PEG, was approved for the photothermal treatment of inflammatory *Acne vulgaris* with minor side effects [128].

The size dependent optimization approach followed the Figure 10(e) that illustrates J_{o} for AuNRs of different lengths and diameters in water. The white dashed line represents AuNR sizes in which LSPR occurs at $\sim$ 800 nm. Figure 10(f) translates the white dashed line of Figure 10(e) as a correlation of J_{o} and AuNR length. Along this line, the sizes of 41×10 and 90×25 nm were selected for experimental comparison.

4.2 MATERIALS AND METHODS

4.2.1 Gold nanorod samples

Based on computational results, AuNR of sizes 41×10 nm and 90×25 nm were chosen to evaluate experimentally the collective heating of colloidal samples under laser irradiation. Both AuNR sizes have "matching spectra", exhibiting plasmonic peaks in the same wavelength. Colloidal samples of Polyethylene glycol-coated (PEGylated) AuNRs suspended in Phosphate Buffered Saline (PBS) were acquired from Nanopartz Inc. (Loveland, Colorado). The stock concentration of the acquired AuNR samples were 2.5 mg/mL and 4 mg/mL for sizes 41×10 nm and 90×25 nm, respectively.

4.2.2 Strain preparation for PTI

For in vitro analysis, *Candida albicans* (ATCC 14053) cells were cultured in Agar Sabouraud Cloranfenicol at 37 °C for 24 h. The cells were then harvested with an inoculation loop (1 μL) and suspended in 5 mL of sterile saline solution (8.5 g/L NaCl; 0.85% saline). The density of the cell suspension was adjusted according to the 0.5 MacFarland standard with a transmittance of 0.9 at 530 nm, determined by UV-Vis spectroscopy (Ocean Optics USB2000; Ocean Optics, Dunedin, FL). This procedure leads to a standard concentration of yeast containing approximately 3×10^6 colony forming units per milliliter (CFU/mL). This stage was carried out by doctoral candidate Gabrielli M. F. de Oliveira, with my support.

4.2.3 Tumor implantation for PTT

For in vivo assays, male albino Swiss mice (*Mus musculus*) weighing 25 - 35 g, were used. The mice were housed and kept in polypropylene cages with free access to food and water in a room with total air renewal 15 times per hour, under controlled lighting conditions (12 h light/dark cycle) at 22 $\pm$ 2 °C and humidity between 55 and 65%. The handling of the animals during the experiment was approved by the *Comitê de Ética em Experimentação Animal* (CEEA) of Federal University of Pernambuco (UFPE), under process #0088/2023 and in accordance with the National Institute of Health "Guide for the Care and Use of Laboratory Animals" [129].

S180 tumor cells were obtained from the Department of Antibiotics of Federal University of Pernambuco (Recife, Pernambuco, Brazil) and were maintained in mice through weekly intraperitoneal injections. The ascitic fluid with S180 tumor cells germinated for 7 days, after which was aspirated and centrifuged (70 g, 5 min, 4 °C). Cell counting and cell viability testing with Trypan Blue were performed using the sediment and the concentration of viable cells was adjusted with sterile 150 mM NaCl solution to 5.0×10^6 cells/mL. After preparation, the ascitic tumor was implanted subcutaneously in the right axillary region of experimental mice (0.1 mL) for growth in solid form. Tumor progression was assessed until the establishment of a palpable tumor mass with diameter of approximately 1.0 – 1.5 cm. This stage was also carried out by doctoral candidate Gabrielli M. F. de Oliveira, with my attendance support.

4.2.4 Cytotoxicity analysis

Fungal cells from the standard strain suspension were transferred to 10 Eppendorf Tubes (Eppendorf, Hamburg, Germany). Different doses of the stock NP solutions were added to each tube, for a total of 2 mL mixture in each tube, resulting in final concentrations of 6.25 $\mu\mathrm{g/mL}$, 12.5 $\mu\mathrm{g/mL}$, 25 $\mu\mathrm{g/mL}$ and 100 $\mu\mathrm{g/mL}$ for both 41×10 nm and 90×25 nm colloidal PEGylated AuNR samples. Following this procedure, one additional control tube (without NPs) was seeded and all tubes were incubated at 37 °C for 24 h to assess AuNR cytotoxicity.

Volumes of 20 μL of each sample were placed in a 96-well microtiter plate (sterile flat bottom). They were then serially diluted in 180 μL of saline solution (0.85%) until diluted to

1:10^6. To perform track-dilution plating, aliquots of 10 μL of the serial dilutions were transferred, with the aid of a multichannel pipette (Eppendorf, Hamburg, Germany) to two 90×15 mm Petri dishes (Kasvi, Paraná, Brazil) containing the previously solidified Agar Sabouraud Cloranfenicol culture medium. The plates were identified and conditioned in an incubation oven, where they remained for 24 h at 37 ^{o}C.

After 24h, the plates were removed from incubation for counting the colony forming units obtained from the serial dilution. The number of colonies were evaluated counting the colonies using Fiji ImageJ (Bethesda, MD). For this purpose, each plate was photographed. In the plate images, the area of interest containing the colonies was selected. The selected region was then converted to grayscale and a threshold adjustment was performed to distinguish the colonies and the background. This resulted in a high contrast image that still required watershed segmentation to distinguish between colonies that were close together. Then, the total number of colonies was automatically counted. The results were verified by an experienced professional microbiologist to ensure the validity of the counting method. The final cell viability was calculated dividing the final number of colony forming units obtained for each AuNR concentration by the final number of colony forming units in the control plates.

Cytotixicity analysis was not carried out for in vivo PTT in mice. Instead, experimental cytotoxicity of gold NPs in vitro available in the literature was used to establish safe sample concentrations for intratumoral administration of AuNRs [109]. Therefore, to maintain cell viability prior to laser irradiation, a maximum PEGylated AuNR concentration of 100 $\mu\mathrm{g/mL}$ was chosen.

4.2.5 Laser heating

In PTI, a 1 mL aliquot of the viable and control samples were transferred to Eppendorf Tubes and continuously irradiated by pulsed laser (Chameleon Vision II, - 140 fs/80 MHz; Coherent, Santa Clara, CA) at 808 nm. The laser optical intensity reaching the sample was 1 W/cm^2 and exposure time was 10 minutes. During laser exposure, the tube lids were kept open, and laser light was directed downwards, aligned to the tube opening. The beam waist matched the tube diameter, ensuring that the sample was thoroughly illuminated. A thermal imaging camera (Flir E4; Flir, Wilsonville, OR) was used for real-time temperature acquisition.

UV-Vis absorbance spectroscopy (Ocean Optics USB2000) was performed before and after irradiation of the samples containing AuNRs to ensure that the temperature assessment did not degrade the AuNPs during the experiment. The yeast samples submitted to photothermal treatment were reseeded in plates following the Track Dilution Method for further quantification of colony forming units [130]. All tests were carried out in triplicate and under aseptic conditions inside a laminar flow chamber.

For PTT, laser irradiation took place after 7 - 10 days of tumor growth. Subsequently, the animals were divided into seven experimental groups carrying S180, summarized in Table 3. As PTT was carried out on different days, saline irradiation (heating control groups) was performed

twice (G2 and G7).

Table 3 – Experimental groups for PTT in S180-bearing mice.

	Saline	**41×10 nm**	**90×25 nm**
Laser	G2 and G5	G1	G4
No laser	G7	G3	G6

Animals were anesthetized with 2% Xylazine (10 mg/kg) and 10% Ketamine Hydrochloride (75 mg/kg). The tumor region was shaved and the mice placed in supine position on the irradiation bed. Subsequently, 200 μL of an aqueous suspension containing PEGylated AuNRs (100 $\mu\mathrm{g/mL}$) or saline (0.9%) were injected intratumorally immediately before irradiation. Similarly to fungal PTI procedures, two distinct AuNR sizes were tested (41×10 and 90×25 nm). Laser beam waist and power were adjusted to expose the entire tumor to 1.0 W/cm^2 irradiance at 808 nm for 10 minutes, during which thermographs were taken using the thermal imaging camera. Throughout the irradiation process, a physical barrier was used to protect the animal face from diffuse reflections and prevent blindness. Mice were sacrificed 72 h after irradiation and tissue histology was performed in the irradiated tumors.

The experimental setup for laser heating experiments is depicted in Figure 12. Beam fluence is controlled by a Glan polarizer system and the beam expander controls the beam diameter at the sample. Notice that the same scheme was used to irradiate both the fungal and tumor samples (at different instances). While beam diameter was 0.7 cm for fungal irradiation, the beam width was adjusted to conform to the tumor diameter.

4.3 RESULTS AND DISCUSSIONS

4.3.1 Optical characterization of gold nanorods

Characterization of AuNR samples were performed via UV-Vis spectroscopy. Figures 13A and 13 illustrate the normalized absorbance of AuNR samples. In both cases, plasmon peak is located at ~ 808 nm.

4.3.2 In vitro PTI of *Candida albicans*

On exploring plasmonic NPs as nanoheaters, higher concentration should lead to a higher temperature increase, which is desirable for therapeutic applications. However, the used concentration of NPs must not be too high due to toxicity of the nanostructured agent [121]. Furthermore, different NP sizes also leads to different cytotoxic responses and requires the investigation of its effects [131].

The results of the AuNR cytotoxicity analysis is depicted in Fig 14, which shows the colony survival fraction for the different concentrations of AuNRs. Even though the mass

Figure 12 – Schematic details of the laser irradiation setup. The Eppendorf holder is used to irradiate the fungal samples, while the mice is placed on the irradiation bed. The three insets in the bottom left shows, respectively, from left to right, the intratumoral inoculation of AuNRs in mice, the irradiation of S-180 tumor and the irradiation of fungal suspension.

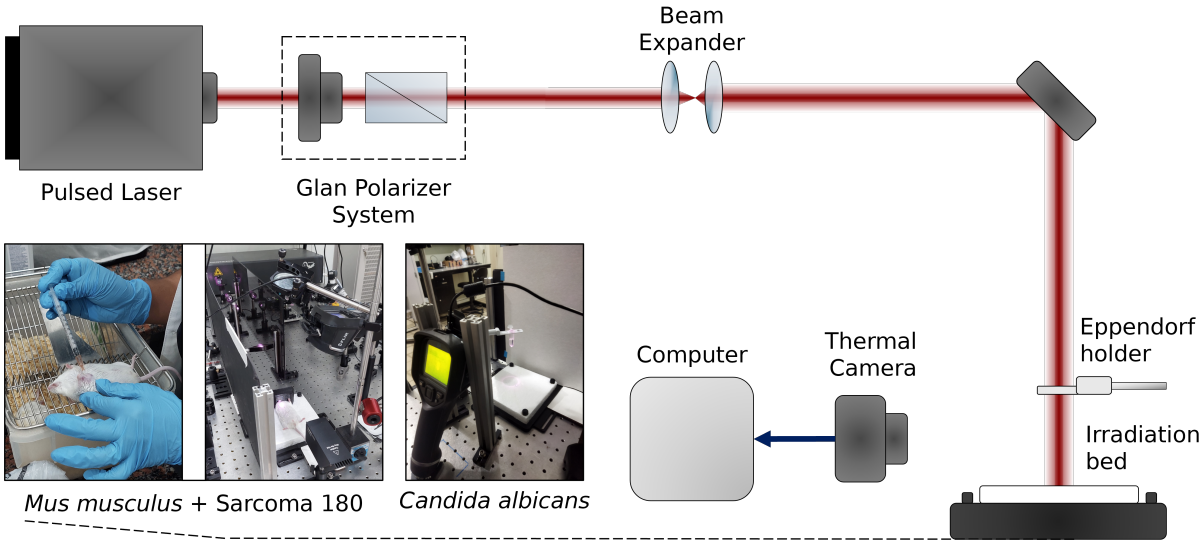

Source: belongs to the author.

Figure 13 – UV-Vis spectroscopy AuNR samples with the normalized absorbance of **A.** 41×10 nm AuNR sample; and **B.** 90×25 nm AuNR sample.

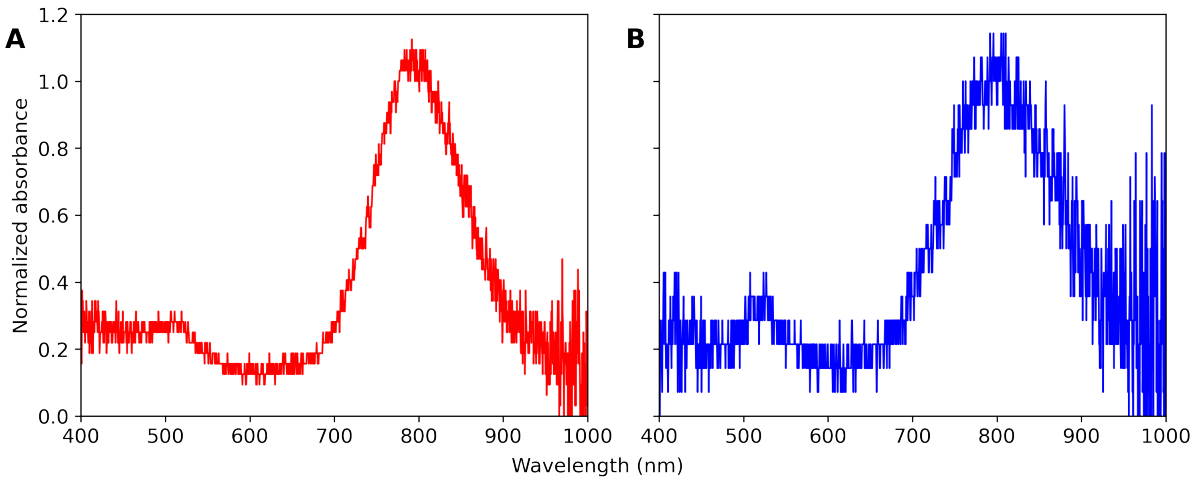

Source: belongs to the author.

concentration of colloidal gold in each sample is the same among the two nanorod sizes used (41×10 and 90×25 nm), the larger nanorod (gray) is considerably more cytotoxic, showing low survival fractions even at the lowest concentration (6.25 $\mu g/mL$). The use of 41×10 nm AuNRs (blue) remains viable for all concentrations tested. CTAB is a highly cytotoxic surfactant used to aid nanorod synthesis that also acts as a surface stabilizer to prevent aggregation [132]. The presence of CTAB in AuNRs directly affects the cytotoxicity of the NP, which can be decreased by the PEGlayering of nanorods. However, PEGylated nanorods still have CTAB molecules [133]. As the AuNR size increases, its surface area also increases, leading, consequently, to higher NP cytotoxicity due to the presence of larger amounts of CTAB.

As the toxicity of 90×25 nm AuNRs above 25 $\mu g/mL$ is enough to inactivate the yeast in the bulk, the PTI analyses were performed for concentrations of 6.25 $\mu g/mL$ and 12.5 $\mu g/mL$ only.

Figure 14 – Mean values of the survival fraction of *Candida albicans* incubated with different sizes and concentrations of PEGylated AuNRs.

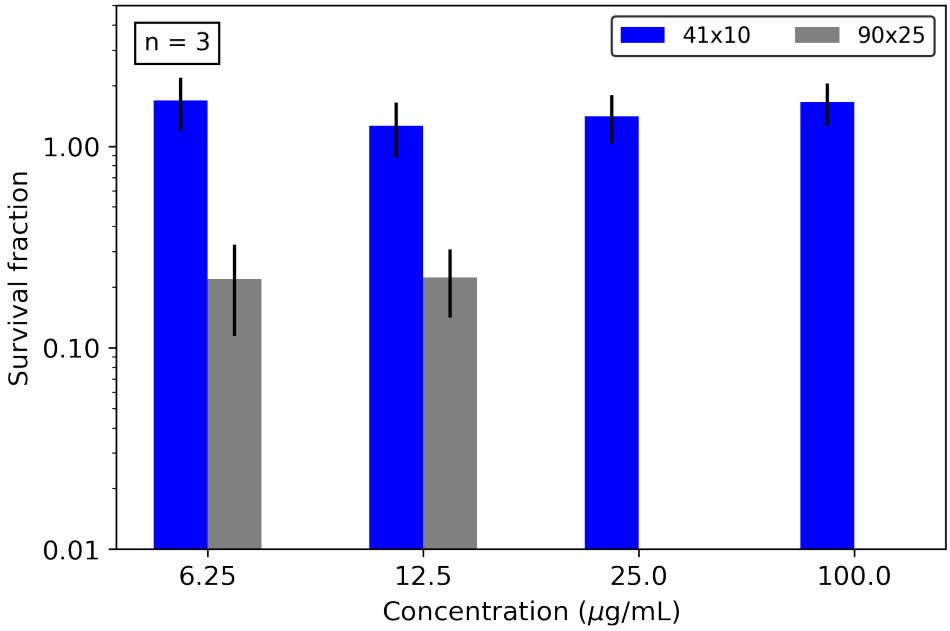

Source: belongs to the author.

Fig 15 shows the final temperature of the AuNR-fungal suspension after 10 minutes of laser irradiation. The temperature in all AuNRs suspensions raised above 35 ^{o}C and the thermal image of the Eppendorf Tubes reveals that the entire volume experiences uniform heating. It is well known that the heating temperatures achieved are the direct consequence of irradiation power. Nevertheless, the adherence to safe levels of laser exposure (typically 1.0 W/cm^2 [26]) for translational applications are a limiting factor in the use of higher irradiation powers. Consequently, NPs are essential in enabling sufficiently high-temperatures for therapeutic use.

Figure 15 – Thermographic stills of the samples after 10 minutes of laser irradiation. The rectangles indicates the sample location in the tubes. The colorbar (virtual) restricts the temperature to the same range range in all stills.

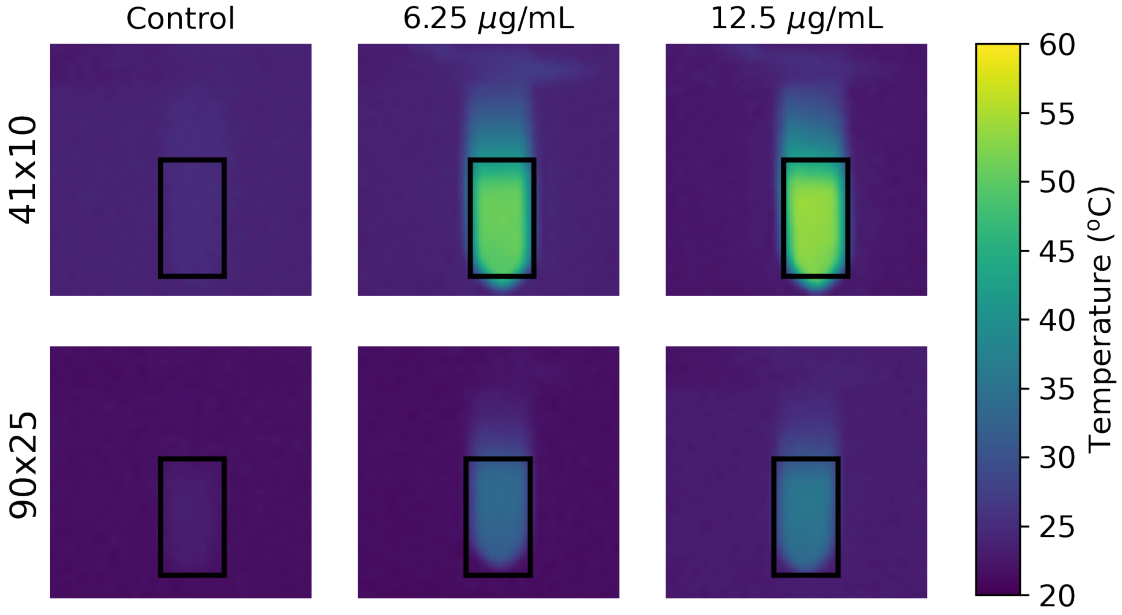

Source: belongs to the author.

In a collective heating of NPs, when the mass of gold is the same among different samples containing AuNRs of different sizes, the sample that will achieve the higher temperature is the one with larger Joule number [84]. For instance, for colloidal 41×10 nm AuNRs the average temperature after 10 minutes of laser irradiation (1 W/cm^2) was 27.9 and 53.1 °C for NP concentration of 6.25 and 12.5 $\mu\mathrm{g/mL}$, respectively, while in colloidal 90×25 nm AuNR samples the average temperature after 10 minutes of laser exposure was 32.3 °C for 6.25 $\mu\mathrm{g/mL}$ and 45.4 °C for 12.5 $\mu\mathrm{g/mL}$. Only the samples containing AuNRs of size 41×10 nm were able to achieve temperatures above the 42 °C, the temperature threshold assumed to initiate hyperthermia effects such as eukaryotic cell membrane alterations [26, 112, 134].

Fungal inactivation rely on the consistent temperature increase induced within the medium. The thermal damage caused by hyperthermia also depends on the time extension in which the higher temperatures are sustained. Fig 16A illustrates the average temperature of each sample during 10 minutes of laser exposure. The temperature was taken as the instantaneous temperature averaged over the the sample area bounded by the solid black boxes depicted in Fig 15. The temperature of AuNR-fungal suspensions for 41×10 nm AuNRs (blue and red solid lines) increased above 37 °C after 5 minutes of laser irradiation at 1 W/cm^2, while for 90×25 nm AuNRs (dashed lines) the temperature was less than 33 °C throughout the whole experiment. Fungal samples without AuNRs (used as a control) were also irradiated, but no significant temperature increase was observed after 10 minutes (solid black line).

After laser irradiation the samples were diluted, transferred to Petri dishes and rein-

Figure 16 – **A.** Temperature increase of AuNR-fungal suspensions for 6.25 $\mu g/mL$ (blue) and 12.5 $\mu g/mL$ (red) under 808 nm laser irradiation (1 W/cm^2). The solid and dashed lines represent AuNR sizes of 41×10 nm and 90×25 nm, respectively. The solid black line depicts the control under the same irradiation conditions. The measured temperature is the average temperature of boxed region in Fig 15. Cultured fungal suspensions subjected to different experimental conditions (12.5 $\mu g/mL$). **B.** Fungi; **C.** Fungi + NP; **D.** Fungi + Laser; and **E.** Fungi + NP + Laser.

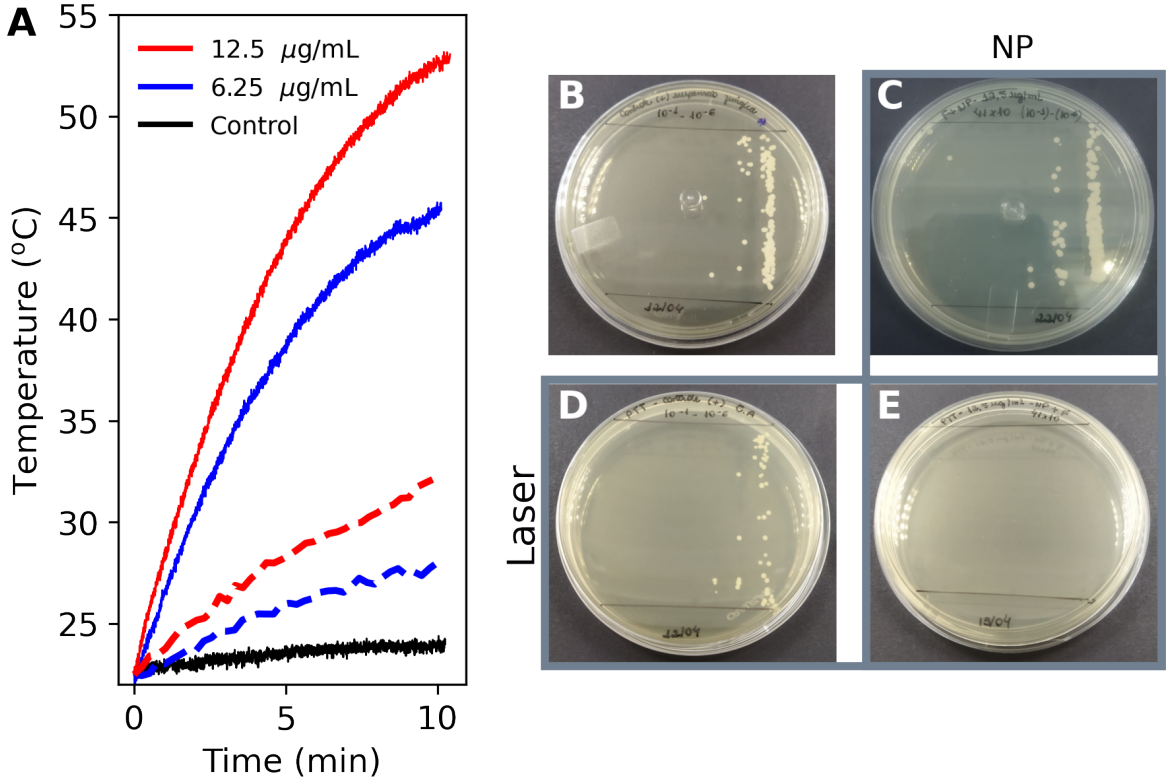

Source: belongs to the author.

cubated. Fig 16B-D display the efficacy of the photothermal inactivation by contrasting plate images of the cultured fungal suspensions subjected to different conditions. Fig 16B shows the growth of the control sample (Fungi), while Fig 16C illustrate the growth of the fungal sample incubated with 41×10 nm AuNRs at concentration of 12.5 $\mu g/mL$ (Fungi + NP). Notice that the presence of AuNRs alone is not enough to inactivate the yeast. Fig 16D depict the growth of the fungal sample after laser irradiation (Fungi + Laser), that was not enough to photoinactivate the microorganism by itself. In contrast, yeast inactivation was achieved when both laser and AuNRs (41×10 nm, 12.5 $\mu g/mL$) were used, as depicted in Fig 16E (Fungi + NP + Laser).

After incubation, the Colony Forming Units were counted for each plate, and the survival fraction of colonies were inferred. Fig 17 shows that only samples containing 41×10 nm AuNRs at 12.5 $\mu g/mL$ were capable of inducing cell death through hyperthermia. This is partially because the maximum temperature in the distribution reached 55 °C in this sample, as depicted in Fig 15. However, it is expected that the use of greater laser intensities should lead to higher

temperatures in all AuNR samples, which contributes to the reduction of the survival fraction, as higher temperatures leads to longer periods of hyperthermia. In none of the 90×25 AuNRs samples, the increase in temperature was able to completely inactivate the microorganisms. Furthermore, subjecting the control samples (without AuNRs) to laser irradiation did not lead to the inactivation of the fungi.

Figure 17 – Mean values of the survival fraction of *Candida albicans* after AuNR mediated laser thermal treatment. The blue and gray bars represents AuNRs of sizes 41×10 nm and 90×25 nm, respectively.

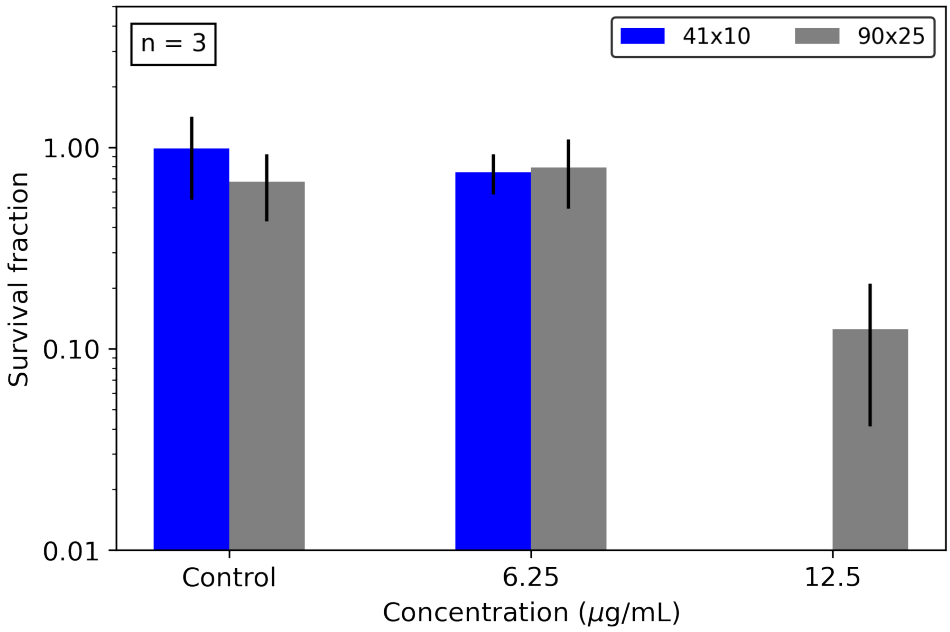

Source: belongs to the author.

4.3.3 In vivo PTT of Sarcoma 180

Wang et al.[109] reported the viability of MDA-MB-435 breast cancer cells after incubation for 48 h with AuNRs of size 36.2×9.1 nm at different concentrations ranging from 1.56 to 200 $\mu g/mL$. Half maximal inhibitory concentration (IC50), a conventional quantitative assay used to determine drug potency in cell-based cytotoxicity tests [135], was found to lie between 100 and 200 $\mu g/mL$. Therefore, AuNR samples were administered at a concentration of 100 $\mu g/mL$ in both G1 ($41 \times 10\ nm$) and G4 ($90 \times 25\ nm$). Irradiation groups G2 and G5, which act as thermal references, were inoculated with saline only. The other groups (G3, G6 and G7) were not irradiated.

For 808 nm, the MPE is limited at $33 mJ/cm^2$ for laser pulses of 1–100 ns [136]. However, for pulse durations shorter than 1 ns, the damage threshold of the energy density scales approximately with the square root of the pulse duration. Therefore, for 140 fs laser pulses, the MPE at 808 nm is scaled down by a factor of $\sqrt{1\ ns/140\ fs} = 84.5$, limiting the pulse fluence to $0.39\ mJ/cm^2$ [26]. For in vivo PTT, tumor diameter averaged 1.0 cm and produced an effective

area of approximatedely 0.78 cm^2. Therefore, the laser power was adjusted to provide irradiance equivalent to 1.0 W/cm^2 ($12.5\ nJ/cm^2$), in accordance to the Maximum Permissible Exposure (MPE), and a total dose of 600 J/cm^2 was delivered to all rodents after 10 minutes of irradiation. Thermal performance of S180-bearing mice inoculated with 41×10 nm AuNRs is illustrated in Figure 18. Figure 18A shows the average temperature of the irradiated tumors with error estimates (n = 4). The red line is the average temperature for tumors inoculated with AuNRs of size 41×10 nm (G1), while the black line describes the average temperature for tumors inoculated with saline (G2).

Figure 18 – Photothermal performance on S180-bearing mice inoculated with 41×10 nm AuNRs. **A.** Average surface temperature of the irradiated tumors with error estimates (n = 4). The red line is the average temperature for 41×10 nm AuNRs (G1), while the black line describes the average temperature for saline (G2). The colormaps depict the thermographic stills at 10 minutes for **B.** 41×10 nm AuNRs (G1) and **C.** saline (G2).

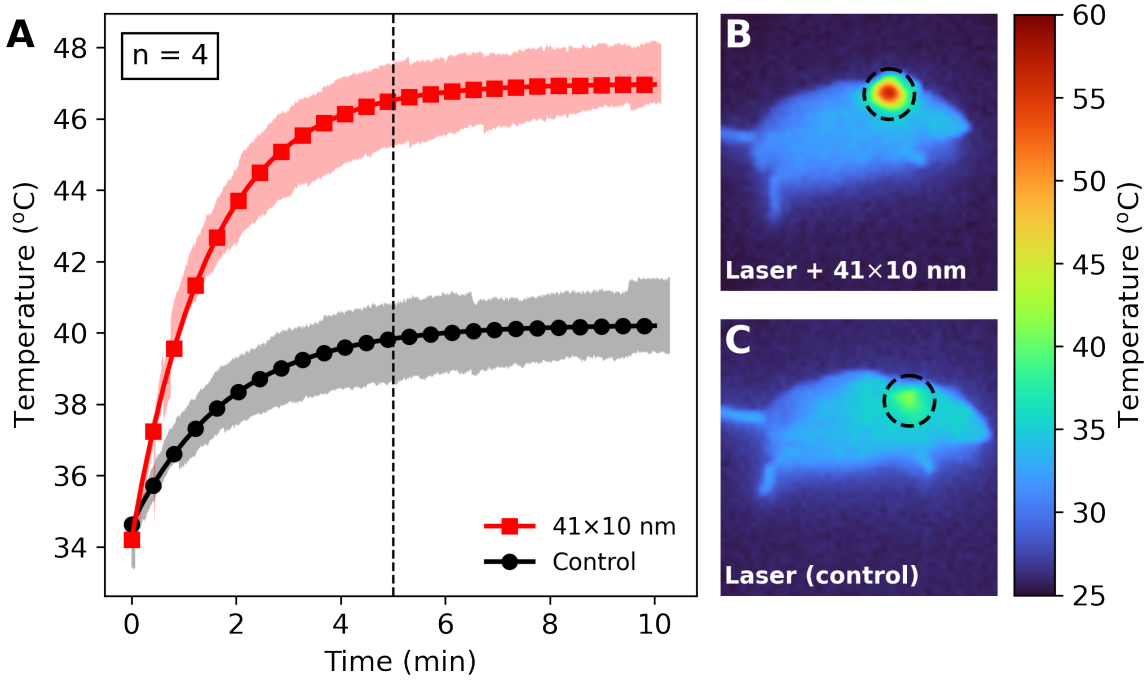

Source: belongs to the author.

For 41×10 nm AuNRs (G1), the temperature at the center of the tumor reached 65.0 °C after 6 minutes of irradiation, as depicted in Figure 18B. Temperature at the tumor edges after 10 minutes of irradiation was of about 40.0 °C, accounting for an average tumor temperature of 46.8 °C, demonstrating the high localization of the therapy. The highly localized hyperthermia generated as consequence of photothermal conversion may lead to membrane disruption or protein denaturation of targeted cells, resulting in cell death. The average temperature was measured considering the thermal distribution inside the dashed lines of Figures 18B and 18C. Tumors with saline solution (G2) experienced maximum temperature of 49.5 °C at its center (Figure 18C), and the average tumor temperature was observed to remain under 42 °C (39.7 °C).

Likewise, irradiation of S180-bearing mice inoculated by 90×25 nm AuNRs samples (G4) produced temperatures of 61.8 °C at the central region of the tumor, for an average temperature increase of 44.6 °C (Figure 19A, blue line). A quick inspection of Figure 19B reveal the shorter reach of thermal distribution around the tumor when compared to Figure 18B. Therefore, a lower efficacy therapy was expected, as the edges of the tumor weren't able to surpass 42 °C. Figure 19C portrays laser heating for mice inoculated with saline, and the black line of Figure 19A indicates an average temperature of 40.7 °C for G5. Overall, the PTT in G1 resulted in temperatures $\sim$ 2-3 °C above the G6 assessed temperature, while the temperatures between thermal control groups (G2 and G5) remained similar, within error estimates.

Figure 19 – Photothermal performance of S180-bearing mice inoculated with 90×25 nm AuNRs. **A.** Average surface temperature of the irradiated tumors with error estimates (n = 4). The blue line is the average temperature for 90×25 nm AuNRs (G4), while the black line describes the average temperature for saline (G5). The colormaps depict the thermographic stills at 10 minutes for **B.** 90×25 nm AuNRs (G4) and **C.** saline (G5).

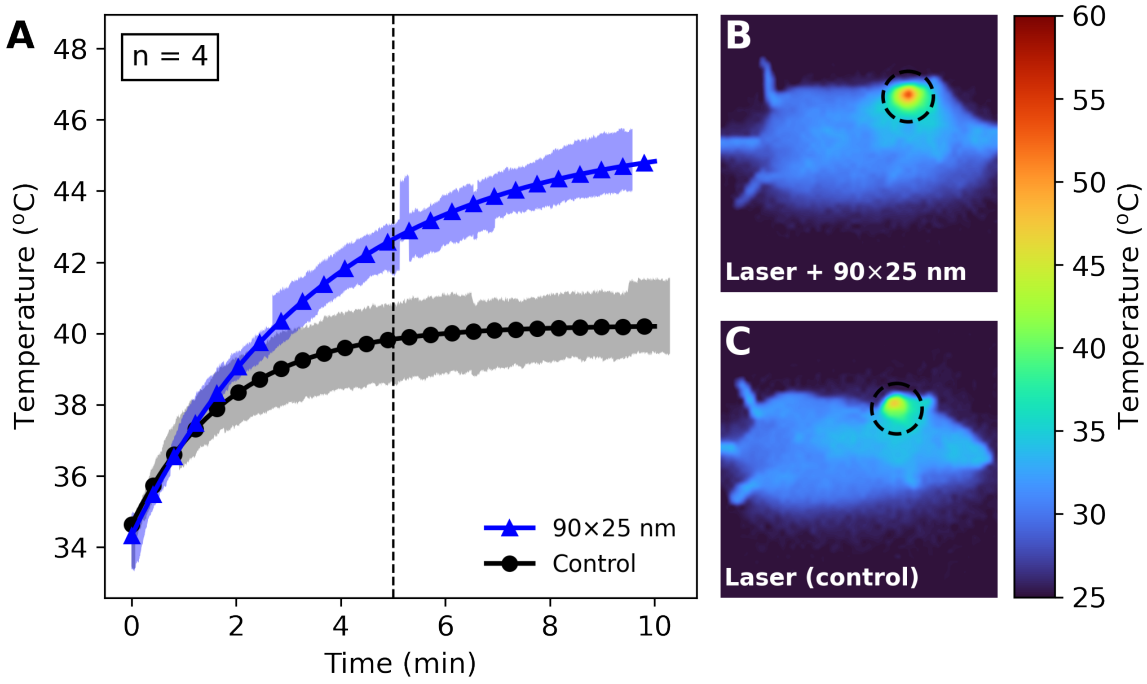

Source: belongs to the author.

Figure 18A shows that after 5 min G1 reaches the thermal equilibrium and the temperature stabilizes. This is not the case for G4 (Figure 19A), where after the 5 min mark the temperature is ~ 4 °C lower than G1. Therefore, the use of optimized NP reduces the time needed to achieve higher temperatures, decreasing therapy time. As non irradiated control groups, G3, G6 and G7 weren't subjected to thermal analysis.

In normal tissues, apoptosis plays a fundamental role in the cell cycle, maintaining homeostasis [137]. In cancer cells, however, apoptosis is inhibited, which enables unregulated

proliferation of cancer cells that results in tumor growth [111]. Benign tumors undergo expansive growth that leads to smooth borders and sharply demarcate the tumor site from normal tissue. They are typically encased by a fibrous capsule that prevents its spread beyond the layer of tissue in which it developed [138]. In contrast, malignant tumors have infiltrative character, growing into surrounding healthy tissues and spreading beyond the layer in which it originated [139]. Furthermore, invasive tumors are generally characterized by irregular surfaces [140]. In PTT, apoptosis, as well as necrosis, are cell death mechanisms initiated by thermal damage. During necrosis, cell membrane integrity is affected and damage-associated molecular patterns (DAMPs) released from intracellular content triggers collateral inflammatory responses. During apoptosis, DAMPs are released without affecting membrane integrity and leads to a different pathway through phagocytosis [141]. Nevertheless, membrane integrity is also lost if apoptotic cells are not quickly consumed by phagocytes. This leads to necroptosis [112], a process of secondary necrosis [141].

Histological sections of surgical specimens of S180 implanted in rodents are portrayed in Figure 20 and reveal irregular infiltrative margins in all groups, invading and dissociating muscle tissue [142,143]. Photothermal damage to tumor cells injected with AuNRs was confirmed by histological examination, as G1 and G4 form solid blocks of coagulative necrosis. G3, G6 and G7 indicate the presence of viable tumor cells with successive mitoses and regular tumor margins, while G2 and G5 demonstrated small areas of apoptosis.

Figure 20 – Photomicrographs of histological sections stained with HE of surgical specimens of S180 implanted in rodents. (MI) Muscle invagination (black arrows), (AP) Apoptosis, (NE) Necrosis and black circles indicate mitosis. Scale bar: 10 μm.

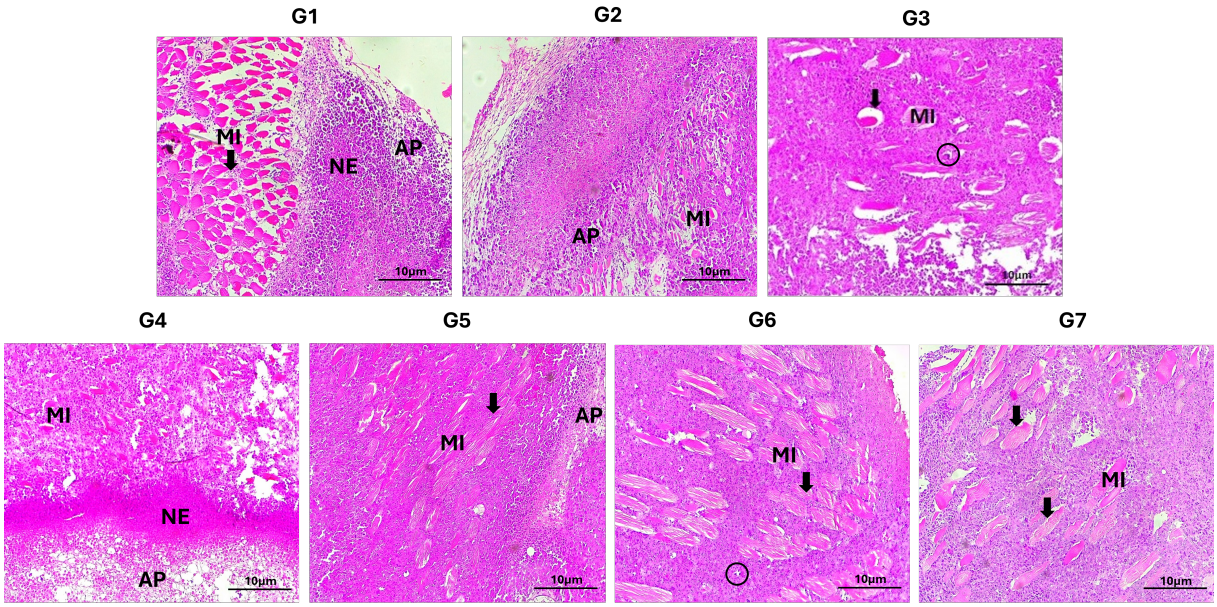

Source: belongs to the author.

The simultaneous presence of apoptosis, necroptosis and necrosis pathways in G1 and G4 implicate in temperature-dependent cell death patterns. At temperatures below 43 °C (low

temperatures), cell killing is ineffective, as cell viability remains above 50%, while at 46 ^{o}C (medium temperatures) both apoptosis and necroptosis are the main contributors to cell death [111]. When temperature is raised above 49 ^{o}C (high temperatures), cell death become necrosis dominant [111]. The absence of coagulative necrosis from irradiated tumors inoculated with saline (Figure 20, G2 and G5) corroborate with the low average temperature observed for both groups (39.7 ^{o}C and 40.7 ^{o}C, respectively), below the 43 ^{o}C mark, despite the considerably higher temperatures achieved at the tumor center. Furthermore, the similar area between necrotic and apoptotic regions of tumor tissues in G1 and G4 are indicative of medium temperature PTT. Notwithstanding the respective maximum temperatures of 65.0 ^{o}C and 61.8 ^{o}C for G1 and G4, the average temperatures observed are compatible with medium temperature PTT. Additionally, no cell death was observed for G3, G6 and G7 and no sign of AuNR cytotoxicity is apparent for G3 and G6.

To minimize necrotic response and maximize beneficial pathways, PTT between low and medium temperature range (43-46 ^{o}C) is preferable. This might be achieved decreasing laser irradiance or photothermal agent concentration, both of which benefit clinical applications.

4.4 CONCLUSIONS

Although photothermal methods have demonstrated their effectiveness in managing microbial infections, there is still a limited literature addressing the thermo-optic inactivation of fungi. The effectiveness of photothermal inactivation of yeast can be increased by exploiting optimized plasmonic nanoheaters. The potential use of AuNRs as optimized nanoheaters for infrared photothermal inactivation of *Candida albicans* was presented. Here we demonstrated that high temperatures of AuNR-fungal suspensions can be achieved (up to 55 ^{o}C) under 808 nm irradiation (1 W/cm^2). To disclose the unique effect of light on fungal inactivation, care was taken to identify the cytotoxicity of different PEGylated AuNR concentrations in the fungal samples. To avoid significant toxicity of the 90×25 nm AuNRs, sample concentrations used on photothermal assays were limited at 12.5 $\mu\mathrm{g/mL}$. Based on theoretical (quantitative analyses of size dependent J_o values) and experimental approach, our findings indicate that colloidal AuNRs of size 41×10 nm can achieve higher temperatures than its 90×25 nm counterpart, considering samples with same total mass of gold and under the same irradiation conditions.

Membrane disruption is potentially one of the outcomes of PTI. For this reason, the use of fluorescence leakage assays, using Acridine Orange and Propidium Iodide as live/dead markers, is better a way to quantify cell viability [144] and might be explored in the future. Further investigations on the PTI of *Candida albicans* using the aforementioned fluorescence techniques enables a more accurate modeling of photothermal induced cell death [145,146] that might also reveal fungal inactivation pathways in more detail.

For in vivo evaluation, S180-bearing male albino Swiss mice (Mus musculus) was used as animal model for appraisal of size dependent temperature increase in PTT mediated by AuNRs.

A total dose of 600 J/cm^2 was delivered for each irradiated mice and temperature increase was measured using thermal imaging camera. The obtained results showed tumor temperature stabilization after 6 minutes of irradiation. Tumors inoculated with AuNRs demonstrated highly localized therapy, while irradiated groups with saline were not observed to reach useful temperatures. Histological analysis confirmed photothermal damage inflicted to tumor cells injected with AuNRs through the discrimination of solid blocks of coagulative necrosis in G1 and G4. Furthermore, the similar area between necrotic and apoptotic regions of tumor tissues in both groups revealed therapeutic intervention in the regime of medium temperatures, while G2 and G5 demonstrated small areas of apoptosis with inefficient cell death.

On exploring optimal and sub-optimal plasmonic NPs as nanoheaters, higher Joule numbers should lead to proportionally higher increase in final temperature. Theoretical results estimate that 41×10 nm AuNRs have $\mathrm{J_o}$ of $\sim$ 300, against $\mathrm{J_o} \sim$ 150 for 90×25 nm samples. Therefore, temperature rise should be twice as higher for 41×10 nm AuNRs. The comparison of temperatures among samples of same concentration, evaluated at the 10 minutes mark, yielded a percentage increase ($100 \times (\mathrm{T_{41\times10}} - \mathrm{T_{90\times25}})/\mathrm{T_{90\times25}}$) of $\sim$ 55% for PTI assessments and $\sim$ 5% for PTT trials. While the increase observed for PTI is compatible with the FoM, in accordance to theoretical predictions, the performance increase for PTT was negligible ($\sim$ 2-3 $^{\mathrm{o}}$C). We attribute the observed discrepancy to a number of factors. The complex behavior of in vivo systems introduce parameters that are not controllable. For instance, tumor vascularization promotes heat exchange with blood flow and limits temperature rise. Also, the high inhomogeneity of biological tissues lead to diffuse scattering and increased reflection losses. Finally, the opaque character of the tumor implicates, as discussed in chapter 2, that virtually all energy delivered is absorbed by the sample. In this context, the contribution of optimization becomes minor, as experienced. In contrast, the transparency of PTI samples enabled the effective appraisal of the FoM.

Experimental results may vary due to random angular orientation of AuNRs throughout the sample, as its orientation in reference to the polarization of the laser affects the absorption of light [27]. Therefore, the anisotropic nature of AuNRs coupled with their random orientation in the sample effectively decreases the absorbed energy. Isotropic NPs such as nanostars can be used to overcome such limitations, as they are capable of absorbing light at NIR wavelengths and have large surface area when compared to nanospheres [147].

Moreover our findings reveal that AuNRs of 41×10 nm exhibit superior efficiency in near-infrared (808 nm) photothermal inactivation of fungi and in photothermal therapy of Murine Sarcoma 180, owing to their higher light-thermal conversion efficiency. The results provide insights to better exploit plasmonic NPs on photothermal inactivation and therapeutic protocols.

5 PLASMON-MEDIATED PHOTOACOUSTIC GENERATION IN GOLD NANOPARTICLES

For metallic NP mediated photoacoustic excitation, thermal processes are crucial contributors to the production of pressure waves. However, the fraction of heat converted into mechanical work depends on both the thermophysical constants of the medium and the NP parameters. Recent studies conducted in AuNR optimization show that a size dependence approach can be explored in the optimization of NPs for photothermal conversion, therefore, optimizing photothermal conversion must also lead to enhancement of photoacoustic amplitude. In this work, we explore photoacostic microscopy to investigate the size effects of AuNSs and AuNRs in photoacoustic generation by nanosecond laser pulses (5 ns, 10 Hz). The experiments were carried out at the Photonics Laboratory of the Physics Department of the Federal University of Pernambuco. Here, the signal amplitude of AuNSs of sizes 5, 50 and 100 nm and AuNRs of sizes 41×10, 90×25 and 134×40 nm were appraised for 530 nm and 808 nm laser excitation, respectively. The use of methodologies for the identification of optimized nanostructures for photoacoustic signal generation might help the establishment of new nanostructured materials as imaging and sensing agents.

5.1 INTRODUCTION

Photoacoustic imaging (PAI) is an emerging technique that combines optical and ultrasound imaging systems to achieve high resolution and deep tissue mapping of biomedical samples [24]. The method explore the high spatial resolution accomplished by optical absorption microscopy while mitigating the limitation in penetration depth imposed by optical scattering using ultrasonic detectors, revealing localized details of micrometer resolution in a sample of relatively large volume, providing a powerful tool that harnesses the advantages of both strategies.

Among PAI applications, its employment in life and biomedical sciences stands out, as it has been used for in vivo non invasive monitoring of glucose for diabetic patient care [148] and for the discrimination of lipid and collagen in biological tissues exporing multispectral excitation as detection strategy [149,150]. Multispectral photoacoustic (PA) tomography, particularly, has been applied for the monitoring of disease progression of Duchenne muscular dystrophy in pediatric patients [150], as a diagnostic tool for inflammatory bowel diseases [151] and as a way to distinguish between nerves and tendons in ex vivo analysis [152]. Many endogenous chromophores that absorb light have been widely used as contrast agents for visualizing physiological responses. For instance, oxyhemoglobin and deoxyhemoglobin are major markers present in blood that enable a multitude of uses, including noninvasive analyses of human palmar vessels [153], human brain imaging [154], neurological applications [155] and breast cancer tumor indentification [156]. For

cancer treatment specifically, PAI is an effective tool for the prediction of tumor recurrence and as a way to probe the therapeutic efficacy of photodynamic and photothermal therapies [157–159]. Furthermore, the recent dissemination of quantum cascade lasers (QCLs) has led to the use of Mid-infrared sources for the detection of biomarkers and organic species such as lipids and water in tissues in a label free approach due to the high contrast generated by the absorption of specific chemical bonds [160–162]. In that regard, the popularization of QCLs and other mid-infrared light sources have the potential of establishing a new paradigm in the field of PA and chemical imaging with direct impact in optical biopsy. Despite our efforts to list the recent advancements in the field, an extensive review of the subject is out of the scope of this chapter and an abundant set of review publications are available elsewhere [163–167].

The two main modalities of PAI are photoacoustic microscopy (PAM) and photoacoustic tomography (PAT). Both configurations offer balance between optical and acoustic resolution in imaging, thus, the focus of the light source and the choice of acoustic transducer are decisive in the final quality achieved [24]. In PAM, a laser beam is used to achieve great spatial resolution and low depth of penetration through focusing, while PAT relies on more diffuse illumination, providing great depth of penetration and transferring the determination of spatial resolution to the array of ultrasonic transducers and reconstruction algorithms [65,168]. A single ultrasonic detector in PAT provides low spatial resolution, while the use of detector arrays is capable of providing spatial resolution close to PAM systems [24,65,168,169]. When the optically excited volume is smaller than the acoustic volumetric resolution, PAM is achieved with lateral resolution of micrometric order, given by the beam waist size. When the optically excited volume is greater than the acoustic volumetric resolution, the spatial resolution is dictated by the acoustic transduction system.

Most devices for PAI use pulsed laser sources lasting nanoseconds with pulse energy in the order of tens of millijoules [170]. Such high energy pulses are required to optimize the penetration depth into the medium, which depends on laser wavelength and tissue absorption, initiating the thermoelastic expansion of the medium and inducing high PA signal generation with minimal thermal diffusion effect. On the other hand, the use of modulated CW sources induce a predominantly photothermal effect with low efficiency in PA signal generation due to longer pulse periods [171]. LED setups have also been successfully employed as PA pumps, providing the advantages of adjustable repetition rate, small footprint and lower cost over traditional laser sources [36,172,173].

The irradiance of the light source must be within Maximum Permissible Exposure (MPE) limits determined for each wavelength and lighting regime. Therefore, not only the MPE of a single pulse must be respected, but also the average power for repetition rates above 10 Hz must remain within the maximum permitted power. These limits are provided by the American National Standards Institute (ANSI) [170]. Experiments have demonstrated that maximum depth of PAI in breast tissue occurs at around 800 nm, when compared to 1064 nm and 532 nm, for the same excitation power [174]. However, PAI penetration into breast tissue for 1064 nm is potentially

greater when compared to 800 nm due to higher MPE: maximum skin exposure power in the second NIR transparency window is greater than in the first NIR transparency window. Thus, associated with the high availability of high-power pulsed lasers at 1064 nm on the market, the second NIR transparency window has become increasingly popular for PAI [174].

In synergy with wavelength, the chromophore has to be able to absorb the laser line while providing efficient light-to-heat conversion. Various exogenous contrast-enhancing agents have been investigated for use in imaging and functional analyses, including organic dyes, nanodroplets, gold nanoparticles and carbon nanostructures [175–179]. Moreover, exogenous chromophores are not limited to optically transparent organs, which is the case for endogenous chromophores [180]. The emergence of NP mediated PAI has led the increased interest towards the phenomenon of plasmon-mediated signal generation and provide advantages such as high selectivity by means of wavelength and targeting fictionalization, good sensitivity and cheapness. Likewise, the high temperatures reachable by nanostructures supporting plasmon resonance enable micro-bubble formation, that have been reported to induce cell perforation and cellular disruption [181] as well as provide enhanced visibility during PAI [182].

For metallic NP mediated PA excitation, thermal effects are the main contributors to the production of pressure waves [183]. The non-radiative release of the absorbed energy produces heating and the thermoelastic expansion of the NP surroundings, generating ultrasound. Change in pressure due to thermal effects is given by [25]:

$$\Delta p = c_0^2 \Delta\rho + c_0^2 \rho_0 \beta_V \Delta T \ , \tag{5.1}$$

where ρ_0 is the equilibrium density of the medium, $\Delta\rho$ is the change in medium density, $\mathrm{c_0}$ is the speed of sound in the medium, β_V is the thermal coefficient of volume expansion and $\Delta T = C_{np}\sigma_{\mathrm{abs}}F/\rho_0 c_{\mathrm{p}} V_{\mathrm{np}}$ is the temperature change, with $\mathrm{C_{np}}$ the volumetric density of NPs, $\mathrm{V_{np}}$ the volume of the NP, $\mathrm{c_p}$ the specific heat and F the laser fluence. As consequence, the fraction of heat converted into mechanical work has dependence on both thermophysical constants of the medium and NP parameters. Equation 5.1 explicitly states the relation between PA amplitude and temperature increase. Thus, for plasmon-mediated PA signal generation the amplitude of the measured acoustic wave must be directly proportional to $\mathrm{J_o}$, following temperature rise [84,87].

The performance of gold NPs of different sizes as nanoheaters have been evaluated in the past, however, most reports either have a theoretical nature [184–186] or were performed to investigate secondary effects such as NP aggregation [187], transverse mode excitation of AuNRs [188] and the consequences of thickness in the heat-transfer properties of silica-shelled AuNSs [189]. Therefore, in this chapter, PAM setup is employed to evaluate the effects of optimized AuNSs and AuNRs, following a NP size dependence approach.

5.2 MATERIALS AND METHODS

5.2.1 Gold nanoparticle samples

Based on computational results, the size dependent J_o was obtained (Chapter 3). AuNS samples were selected to evaluate the size dependent PA signal generation of gold colloids at 530 nm wavelength. Citrate-stabilized colloidal samples of monodispersed AuNSs in deionized water (less than 12% variability in size and shape), with diameters of 5, 50 and 100 nm, were acquired from Sigma-Aldrich (Missouri, EUA). Likewise, AuNRs of three different sizes were chosen to assess PA signal generation of colloidal gold under 808 nm laser irradiation. CTAB-stabilized colloidal samples of AuNRs in deionized water with sizes 41×10 nm, 90×25 nm and 134×40 nm were acquired from Nanopartz Inc. (Loveland, Colorado). The stock concentration of the acquired AuNR samples were 42 μg/mL, 60 μg/mL and 55 μg/mL for sizes 41×10 nm, 90×25 nm and 134×40 nm, respectively.

All samples were diluted in distilled water leading to solutions of the same total mass of gold. For AuNSs the final concentration among samples was 17.4 μg/mL, while for AuNRs it was 42 μg/mL. UV-Vis spectroscopy (Ocean Optics USB2000) was performed before and after the experiment to ensure that the NPs were not degraded and NP stability was assessed by scanning electron microscopy (SEM) after PAM.

5.2.2 Photoacoustic microscopy (PAM)

PA characterization was carried out employing a customized PAM setup shown in Figure 21 and previously described in Das et al.[190]. In short, laser light from an optical parametric oscillator (OPO) (OPOTEK, Vibrant 355 LD, 0.4–2.4 μm, 5 ns) operating at 10 Hz was focused in the samples consisting of three medical polyvinyl chloride (PVC) capillary tubes (from an IV Infusion set) positioned side-by-side. The tubes, of acoustic impedance of 3.2×10^6 rayls [191], have internal (external) diameter of 1.25 mm (2 mm) and were cleaned via multiple alcohol rinsing prior to sample injection. Gold NP samples were sealed inside the capillary tubes with thermoplastic adhesive and attached to an acrylic holder to provide mechanical stability for the measurements. Two holders with three capillary tubes each were prepared, one for AuNSs (5, 50 and 100 nm) and one for AuNRs (41×10, 90×25 and 134×40 nm). Subsequently, each acrylic holder was submerged into the distilled water cell for characterization, as displayed by the inset of Figure 21. AuNSs and AuNRs samples were irradiated by 530 and 808 nm, respectively, and laser fluence was limited to 20 mJ/cm^2 to comply with the exposure limit of pulsed nanosecond lasers for bioapplications (514 nm) [26].

The water immersion ultrasonic transducer (UST) (Olympus V310-N-SU, 5 MHz) was positioned at an angle to maximize the PA signal from the sample and minimize the effects of reflection and absorption at other interfaces, allowing the focused beam (f = 100 mm) to reach the sample. The sample was scanned using a X-Y motorized translation stage placed under the

water cell, comprised of two 50 mm linear stages (MTS50-Z8—50 mm, Thorlabs, Inc.). The acquired signal was amplified 19.4 times using a radio-frequency low noise amplifier (LNA) (ZFL-500LN-BNC) connected to a digital storage oscilloscope (DSO).

Figure 21 – Schematic details of the PAM setup. The beam fluence is controlled by a Glan polarizer system, and a small part of the beam is directed to a reference photodetector to trigger the digital storage oscilloscope (DSO) for data acquisition. The beam waist is reduced 10× and focused on the sample through a 100 mm convex lens. The sample is swept by the X-Y motorized translation stage and the PA signal acquired through the ultrasonic transducer (UST) is conditioned by the low noise amplifier (LNA) prior to being recorded by the DSO. The inset features the distilled water cell showing the focusing lens and UST positioning, as well as the details of the sample holder.

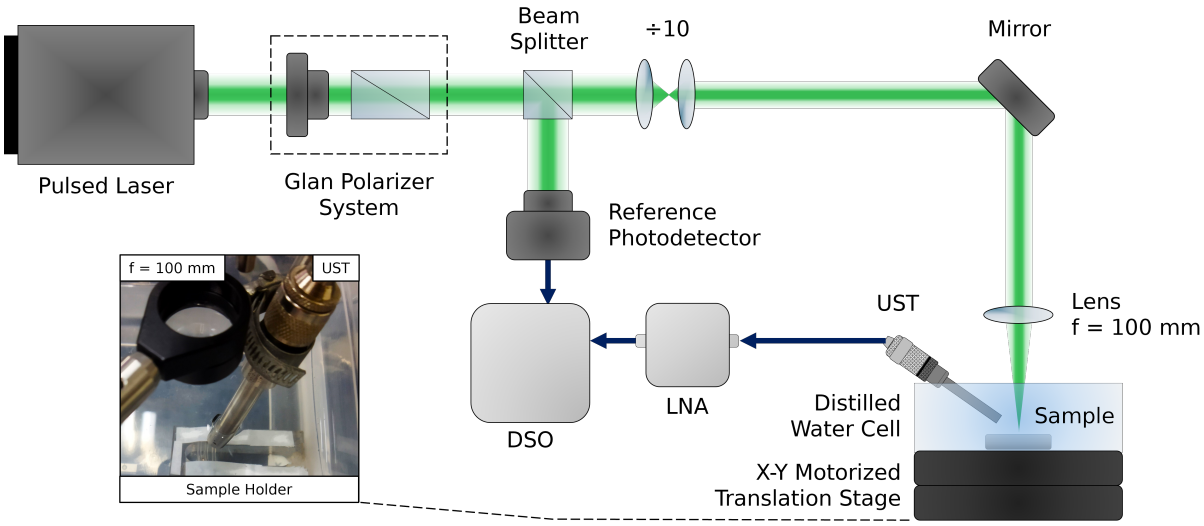

Source: belongs to the author.

5.3 RESULTS AND DISCUSSIONS

In gold NPs, the energy absorbed from a short laser pulse is converted into heat in a matter of tens of picoseconds [192], which causes it to quickly heat up while still absorbing the nanosecond laser pulse. Also, the thermal relaxation time of a gold NP is considerably longer than the time it takes to heat up. For instance, for heat to diffuse 100 nm (in water), it takes about 100 ns [83], facilitating the NP localized thermal buildup that promotes its thermoelastic expansion and gives rise to the PA signal. Despite the local amplitude enhancement assisted by individual NPs, the resulting contrast emerges from the contribution of all NPs within the heated volume and NP shape does not affect the overall waveform, as shown in Figure 22, that illustrate the photoacoustic response of samples containing 50 nm AuNSs (blue solid line, λ = 530 nm) and 90×25 nm AuNRs (red solid line, λ = 808 nm) after one laser pulse. The delay observed between photoacoustic pulses ($\sim 0.5\ \mu s$) is caused by slight changes in the sample distance from the UST ($\sim 0.749\ mm$, considering the speed of sound in water [193]). Such distance, however, only contributes to 0.04% attenuation [193] and is not sufficient to affect the detected signal.

Figure 22 – Photoacoustic signal from 50 nm AuNSs (blue solid line, λ = 530 nm) and 90×25 nm AuNRs (red solid line, λ = 808 nm). The overall shape of the PA signal is not affected by sample size and morphology.

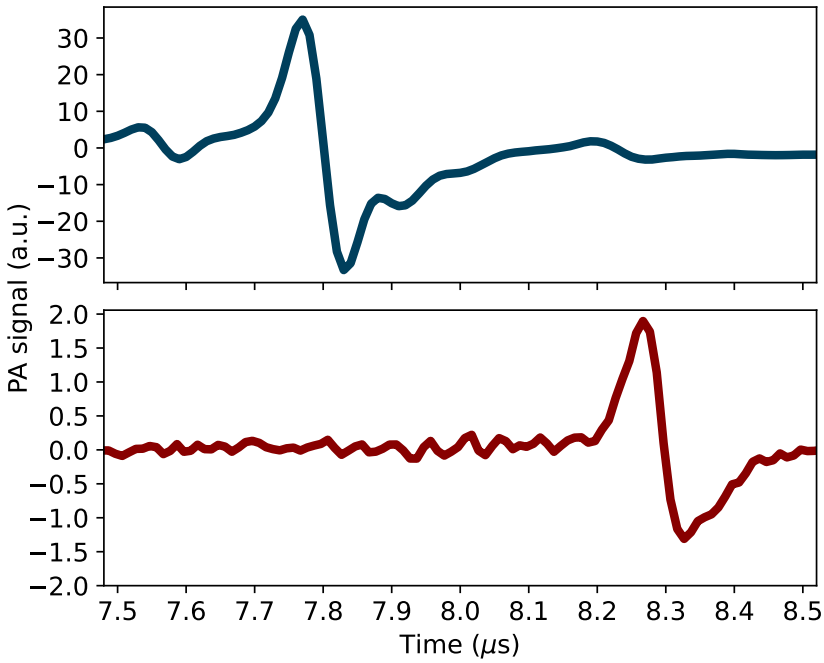

Source: belongs to the author.

To determine the lateral resolution of the imaging system, a high contrast sharp-edged black colored pattern on a plastic card with an abrupt change in absorption was imaged under 530 nm excitation as shown in Figure 23**A**. The averaged measured profile (white dashed line) was fitted to the edge spread function (ESF, red dashed line), while its first order derivative provided the line spread function (LSF, solid blue line), as shown in Figure 23**B**. The 100 mm focusing lens yielded a lateral resolution of about 295 μm for the PAM setup, estimated from the full width at half-maximum (FWHM) of the corresponding LSF [194,195]. The large field of view (FoV) necessary to get all three capillary tubes in a single image entails a compromise between resolution and scanning time.

To attest NP size dependence effect on the PA signal generation, the produced intensities were recorded for the prepared AuNS and AuNR samples. Figure 24A depicts the PAM image for the AuNS sample (λ = 530 nm), covering a FoV of 15×4 mm, whereas Figure 24B (λ = 808 nm) shows the PAM image obtained for the AuNR sample, covering a FoV 12×4 mm. In both cases, the capillary tubes containing the colloids were positioned on the acrylic base in ascending order of NP size, from left to right. The intensity behavior of the samples are denoted by the virtual color bar on the right-hand side of Figures 24A and 24B and the vertical dashed lines indicate the capillary tube lateral boundary with a dimension of ∼2 mm. For the AuNS sample (Figure 24A), the colloidal fluid containing NPs of 50 nm size produced the highest PA intensity, followed by NP sizes of 5 nm and 100 nm. This is clearly distinguishable in Figure 24C, where

Figure 23 – Experimental determination of the system resolution. **A.** High contrast sharp-edged black colored pattern card. **B.** Qualitative variation in PA intensity caused by the card, while the $\times$ shaped marker depicts the average transition profile along the direction of the white dashed guideline, fitted to the edge spread function (ESF, red dashed line). The corresponding line spread function (LSF, blue solid line) provides the full width at half-maximum (FWHM) of about 0.295 mm.

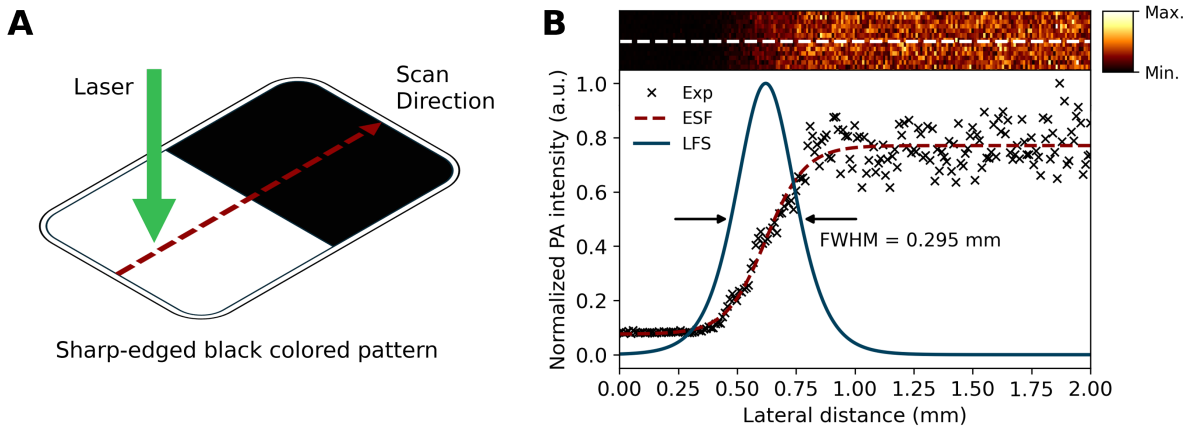

Source: belongs to the author.

the average PA intensity profile of the AuNS sample along the tubes is represented (blue solid line) with its error range (light blue filled region). In both Figures 24A and 24C the highest intensity regions inside the capillary tubes are not centered, but slightly shifted towards the right. This is due to the position of the photoacoustic detector at a slight angle from direct light beam incidence (which can be seen in the inset of Figure 21). Furthermore, as the capillary tubes are cylindrical, the absorption volume of the beam is not the same along the diameter (Beer law), consequently, the variation of PA signal along the diameter of the tube must also be considered. The size dependence effect for the AuNR sample is shown in Figure 24B. Here, the distribution of PA intensities is less homogeneous, despite being clearly contained inside the capillary tubes. Moreover, PA (peak) intensities recovered are significantly smaller ($\sim 4\times$), which is supported by the lower fluence of the OPO at 808 nm ($\sim 2.7\times$ less than 530 nm) and the random angular distribution of AuNR throughout the sample that effectively reduces the absorbed energy in half. The effect of AuNR size is still present, as shown by Figure 24D, where the average PA intensity profile along the tubes is represented by the red solid line and the error range by the light red filled region. The non uniform character of the PA intensity in the colloids of Figure 24B may be explained by the adhesion of CTAB, a cationic surfactant used to stabilize nanorods [196], to PVC, a polymer with a negatively charged surface [197] that can efficiently adsorb materials possessing positive charges through strong electrostatic interactions [198], thus leading to non-uniform agglomeration of AuNRs on the internal surface of the capillary tube.

From the averaged PA intensity profiles (Figures 24C and 24D), the spatial profile of the capillary tubes could also be estimated. For the AuNS sample (530 nm) the FWHM are 1.06, 0.85 and 1.12 mm for the tubes containing NPs of size 5, 50 and 100 nm respectively, averaging

Figure 24 – Experimental PAMs and PA intensities of colloidal gold samples containing NPs of different sizes. **A.** PAM of 5, 50 and 100 nm AuNS samples (λ = 530 nm, FoV = 15×4 mm). **B.** PAM of 41×10, 90×25 and 134×40 nm AuNS samples (λ = 808 nm, FoV = 12×4 mm). The colorbar depicts the PA intensities of the PAMs (virtual colors) and the vertical dashed lines indicate the boundary of the capillary tubes. **C.** Average PA intensity profile of the AuNS sample along the tubes (blue solid line) $\pm$ error range (light blue filled region). **D.** Average PA intensity profile of the AuNR sample along the tubes (red solid line) $\pm$ error range (light red filled region).

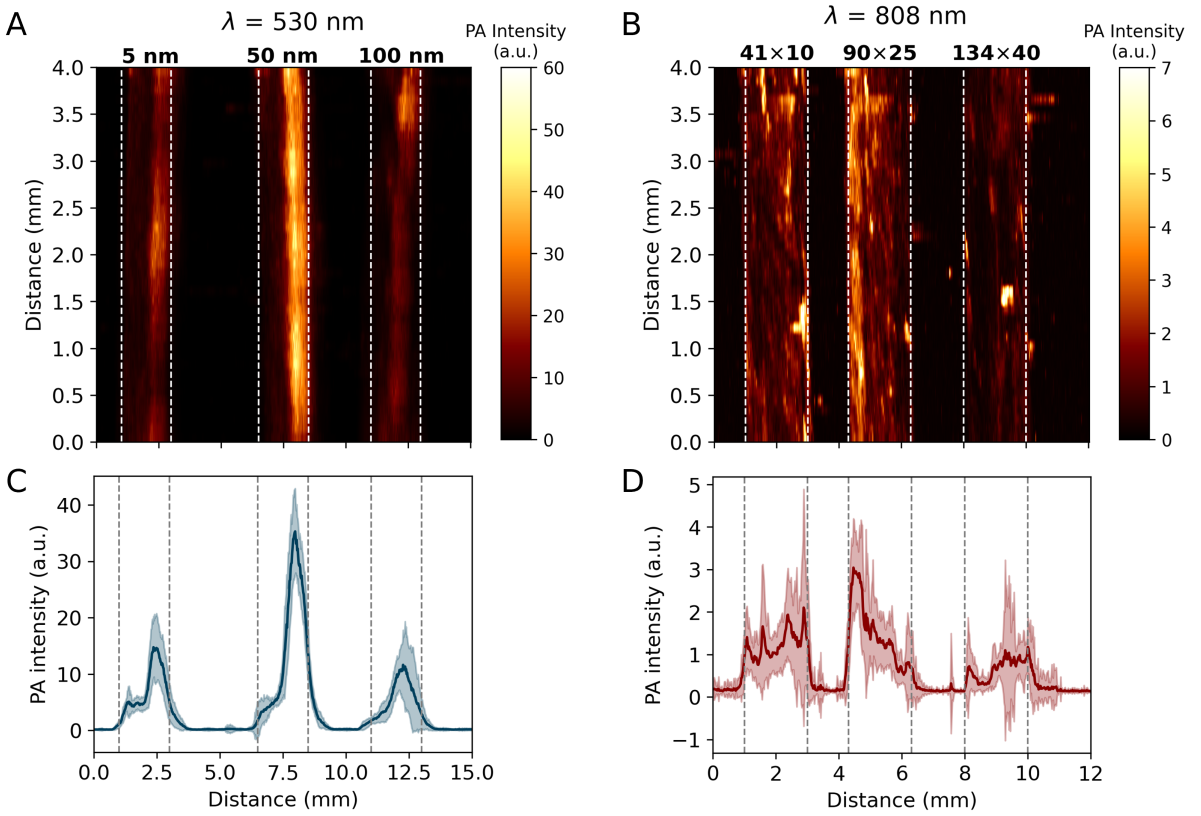

Source: belongs to the author.

to a FWHM of 1.02 ± 0.11 mm. Similarly, for the AuNR sample (808 nm), the FWHM are 1.66, 1.27 and 1.48 mm for tubes containing NP of sizes 41×10, 90×25 and 134×40 nm respectively, to an average of 1.47$\pm$0.16 mm. Consequently, the lateral dimension of the tube measured from PAM averages 1.24$\pm$0.27 mm between both wavelengths, which is a good match to the specification of the capillary tube region that holds the absorbing material (internal). The differences in lateral dimension observed for both wavelengths is attributed to larger beam waist at the focus ($\sim 1.5\times$) produced by the longer wavelength. The enlargement of the beam waist at 808 nm also affects fluence. Besides the disparity in the optical energy absorbed by the two samples, as absorbing NPs must dissipate a relatively large amount of heat in a very small space and across heterogeneous interfaces, thermal resistance at the particle-solvent interface, modified by NP functionalization, might actively influence results by improving thermal confinement and enhancing plasmon-mediated PA signal [199,200].

Image contrast can be estimated using the Weber formula [$W = (I_S - I_B)/I_B$], where I_S is the PA intensity from the sample and I_B is the average PA intensity of the background [201]. Weber contrast for the AuNS sample was calculated to be 42.27 ± 22.61, 101.04 ± 39.88 and 32.23 ± 23.90 for colloids containing NPs of size 5, 50 and 100 nm respectively, whereas for the AuNR sample it was 6.28 ± 4.85, 7.68 ± 5.58 and 2.80 ± 3.06 for NPs of size 41×10, 90×25 and 134×40 nm, respectively. Almost threefold enhancement ($\sim 139\%$) and more than fourfold improvement ($\sim 213\%$) in the PA contrast between AuNSs of size 50 nm and sizes 5 and 100 nm, respectively. Such enhancement is attributed to the size dependence of NP mediated PA signal generation and is illustrated in Figure 25A. Despite the claims that the intensity of PA signals generated by plasmonic NPs increase with σ_{abs}, the trends revealed by Figure 25 indicates better agreement with J_o. While a AuNS of 100 nm has σ_{abs} of 2.08×10^4 nm^2 compared with 6.11 nm^2 of 5 nm spheres, their J_o (7.8) is less than half of 5 nm spheres (16.9).

Figure 25 – Comparison between the size dependence trends of Joule number (solid black lines) and Weber contrast for **A.** AuNS sample (blue markers and dashed line) and **B.** AuNR sample (red markers and dashed lines).

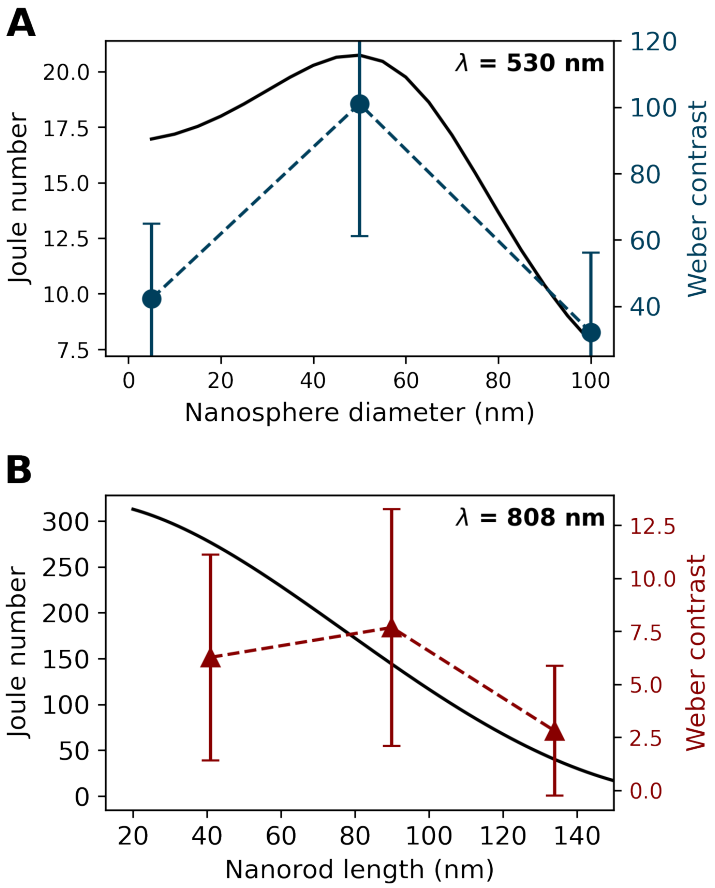

Source: belongs to the author.

For the different AuNR colloids, the enhancement observed for 41×10 nm was of $\sim 123\%$ larger than 134×40 nm. In contrast, the enhancement seen between AuNR samples containing 90×25 nm and 134×40 nm was $\sim 173\%$. This behavior is unexpected, since J_o anticipated that

AuNRs of size 41×10 nm (295.0) should perform better for PA signal generation than longer nanorods (158.7 and 36.2 for 90×25 and 134×40 nm, respectively). We envisage that the low energy effectively absorbed by the AuNR samples concurred to this result, which can be supported by the large error bars of Figure 25B. Furthermore, notice that $\sigma_{\mathrm{abs}}^{134\times40} > \sigma_{\mathrm{abs}}^{90\times25} > \sigma_{\mathrm{abs}}^{41\times10}$ ($4.07 \times 10^3 > 3.55 \times 10^3 > 4.91 \times 10^3$ nm^2) increase for longer AuNRs, in opposition $\mathrm{J_o}$ behavior.

When dealing with high powered nanosecond laser pulses, metallic NPs can suffer fragmentation [202]. Moreover, AuNRs of high aspect ratio become less stable due to thermodynamic instability, which leads to below melting point reshaping [8]. To verify the stability of gold NPs after laser irradiation, the samples were collected in the aftermath of the experiments and subjected to analysis via UV-Vis spectroscopy and scanning electron microscope (SEM). The administered fluence was not sufficient to degrade the NPs. Besides, in our experiments, the laser fluence administered is within the skin exposure limit at 514 nm.

5.4 CONCLUSIONS

In this work, colloidal suspensions of gold NPs in capillary tubes were used as a model for the investigation of NP size effect in plasmonic-assisted PA generation. In this sense, a PAM setup was explored to disclose the size dependence generation of plasmonic-mediated PA signal following a temperature increase optimization approach in colloidal gold. Distinct samples were prepared, accommodating fluids of colloidal gold of different shapes (NSs and NRs) and distinct sizes. Through standard methods of photoacoustic image analysis we have shown that despite having larger absorption cross sections, the large nanoparticle volume of bigger particles leads to less efficient conversion of light into heat.

Hence, photoacoustic intensity follows the trend of Joule number, the same figure of merit employed for assessment of temperature rise of metal NPs by laser heating in Chapter 3. This approach is valid as long as the same amount of gold (total mass or mass concentration) is used among different samples, that is, if between two samples of different NPs the mass of gold is the same in both specimens, the one that provides the PA signal of higher intensity is the one with larger Joule number. This methodology can assist cost reduction in applications where maximum signal excursion is desirable over large quantities of material.

Our results shows that AuNSs of 50 nm size exhibits high $\mathrm{J_o}$ value and high performance on PA generation process, in accordance with theoretical predictions and contrast enhancement among different NP sizes were reported. Despite the limitations of our experiment to demonstrate the optimization effect on AuNRs, the phenomena was still observed within the error margin. A different approach using glass capillary instead of PVC tubing might be employed to mitigate the agglomeration effects.

Although the size of optimized nanoparticles were disclosed, attention must be given to

the desired application, as different interactions might change the thermo-physical parameters of the NP in the host medium. This is predominant mainly in bioapplications, where parameters that are also size dependent, such as NP toxicity, cellular uptake, NP internalization, surface charge and targeting become crucial. Furthermore, optimizing metallic nanoparticles for heat generation may lead to the reduction of the nanoheater concentration used or decrease light fluence for PA applications in the bio sciences, paving the way for the development of more economical contrast agents.

6 SPECTRAL JOULE NUMBER FOR BROADBAND OPTICAL HEATING EVALUATION

The ever-increasing demand for energy across the countries in the world imposes a constant growth in the global supply of energy to meet production and living needs. Such increase has been driven by population growth and/or the improvement of material conditions in some parts of the globe. This is particularly true in Asia, where recent economic growth led to a rise in energy demand driven mainly by industrial production, but also influenced by the search for appliances and personal equipment [203,204]. In this sense, energy production accounts for around 75% of global greenhouse gas emissions and is the largest contributor to climate change through the burning of fossil fuels and biomass [205]. Furthermore, as almost five million deaths each year are attributed to air pollution, the collateral damage caused by greenhouse gases (GHG) emissions are a concern to human health and have a direct impact in healthcare systems [205]. Assessments of global temperature increase driven by GHG emissions indicate that at 1.0 to 2.0 ^{o}C global warming, more than 200 million people, mainly those already vulnerable and marginalized, will likely be exposed to extreme mean annual temperatures and experience long-term sea-level rise [206].

The U.S. Energy Information Administration projects that world energy consumption will grow by nearly 50% until 2050 [203]. Therefore, to reduce global emissions it is crucial to shift our energy sources from fossil fuels to renewables, a challenge for developing countries that must grow their economies while providing access to good living conditions and services to its populations while reducing poverty, without relying on the extensively destructive pathways explored by developed economies in the past and present. Global progress towards large scale adoption of low-carbon sources has been slow, and improvement in energy efficiency is necessary to reduce the stress over the global natural resources, as the sustainable sources has to meet the additional demand each year while displacing existing non-sustainable sources.

Hereupon, plasmonic NPs have been applied for solar energy harvesting devices to improve their performance. In this work, a new approach is proposed for the identification of NPs optimized for absorption of broadband radiation. The approach is applied in the context of the use of nanostructures for solar collection, exploring DASC and nanofluids based on metallic (Au) and dielectric (PDA) nanoheaters.

6.1 INTRODUCTION

Considering the negative environmental and socio-economic consequences of energy generation with fossil fuels, the insertion of clean energy sources in the energy mix is a goal for global sustainable development. In this context, solar energy is expanding as a key renewable energy source due to its large availability and declining generation costs. Enabling technologies,

such as photonics and nanotechnology, support the development of solar energy harvesting equipment and techniques, allowing the expansion of the solar energy field. Following this trend, the use of nanoparticles as solar absorbers has become a subject of many investigations in recent years. Hence, the use of NPs for solar devices covers a variety of applications as photovoltaic [207] and photothermal energy conversion [19], photovoltaic/thermal spectral splitters [31], stills [208], and solar vapor generation [209].

Solar thermal applications rely on converting solar radiation into thermal energy and transferring heat to a medium. This energy can be stored and applied for processes such as water heating, air heating, cooling, drying, desalination, and conversion into electrical energy in concentrating solar power plants [210]. The solar thermal collector is the device employed to convert light into thermal energy, available in different designs and categorized according to the light collection modality (concentrating or non-concentrating), motion mode (stationary or non-stationary), and operating temperature (low, medium or high). For low-temperature applications, stationary non-concentrating collectors, such as flat plate and evacuated tube collectors, are the most adopted configurations. To achieve more efficient devices, the research community has put effort into developing new technologies for low-temperature apparatus, such as DASCs [211]. While most solar collectors typically rely on surface absorbers to gather energy, DASCs employs volumetric absorbers. In these systems, the working fluid within the collector converts solar radiation into heat. For this purpose, a colloidal suspension of NPs has been explored as base fluid known as nanofluid (NF) [211].

To maximize the performance of solar thermal devices, the absorption spectrum of the NF must match the solar emission spectrum. Moreover, the resonant wavelength of the NF can be tuned by changing NP material, morphology, concentration, and base fluid composition. Different types of NPs have been used in NFs, including metal NPs such as copper, silver, and gold, oxide NPs, nitrates, and carbon-based NPs [17]. The addition of transition metal impurities to noble metal NPs was shown to improve absorption. For instance, iron-doped gold nanoshells have been proposed to enhance the performance solar collectors, since the inclusion of up to 15% of iron in gold was reported to create new individual electrons that promote interband transitions at longer wavelengths, broadening the plasmon resonance peak and decreasing scattering, simultaneously [27]. Transition metal nitrides NPs have also been reported to possess small scattering cross sections and broad absorption peaks, leading to thermal efficiency higher than 80% for NFs with TiN, ZrN and HfN [19]. In all cases, absorption broadening is crucial to match the NF spectrum to solar radiation spectrum and improve photothermal conversion.

Gold nanoparticles is well used as a NF constituent, mainly due to its plasmonic resonance in the UV-Vis range, chemical stability, and well-measured optical properties [5]. In addition to stability, another advantage of using gold NPs for solar harvesting is the fact that its absorption peak matches the solar spectral irradiance distribution, that is maximized around 500 nm. Furthermore, considering the simplicity of their synthesis, nanospheres are the most common

particle morphology explored for solar harvesting applications [212]. However, the cost of gold is a considerable drawback for its use, and the search for new materials for efficient and scalable absorption remains an important topic. Alternatively, polydopamine (PDA) is an emerging material produced from the polymerization of dopamine and has attracted ample attention in recent years due to its versatility. Its synthesis involves the use of dopamine as a self-polymerizing adhesive building block in solution to form PDA films on substrates [213] and allows the formation of conformal coatings of controlled thicknesses on a variety of surfaces [28]. Moreover, during the deposition of PDA films, polymerization products present in solution precipitate in the form of PDA NPs [28]. This favors its use as templating agent, which coupled with PDA's strong metal ion bonding [213], facilitate the formation of composite nanomaterials.

PDA has desirable properties, and has been extensively explored in a variety of applications. For instance, antimicrobial activity and high optical absorption has been considered for the photothermal inactivation of bacteria and fungus [14,214] and for cancer treatment [215]. The use of PDA NPs has also been reported for sensing and imaging platforms [213,216], as well as drug release applications [28]. Furthermore, PDA NPs have also been employed previously for solar thermal energy. Hauser et al.[217] showed that hybrid PDA NPs are promising absorption nanoagents for NFs, and Iron-oxide PDA-capped NPs were also demonstrated as effective photothermal and stabilizing agent for solar evaporators, providing high evaporation efficiency and material reusability [218]. Additionally, solar desalination mediated by PDA NPs was also investigated through the construction of donor-acceptor pairs within the NP microstructures. This process decrease the energy bandgap and increase the electron delocalization, enhancing light absorption across most of the solar spectrum and enabling the tayloring of NP absorption [219].

The size dependence of PDA NP properties was previously examined by different studies, most of them related to bioapplications of PDA nanostructures, such as size dependent cytotoxicity in different types of tumors [220] and drug delivery [221–223]. Despite the aforementioned efforts, the size dependent generation of heat by PDA NPs has not been investigated yet. Here a size dependence approach based on Spectral Joule number (SJo) analysis is explored on the identification of effective nanoabsorbers for solar collector. Solar heating of gold and PDA NSs is evaluated based on theoretical and experimental approaches.

6.2 THEORETICAL BACKGROUND

6.2.1 Solar harvesting

For NFs, light absorption for a given wavelength (λ) is dependent on the absorption coefficient of the NP, $\alpha_{\mathrm{np}}(\lambda)$, and the absorption coefficient of the basefluid, $\alpha_{\mathrm{bf}}(\lambda)$. Thus, the effective absorption coefficient of the NF is $\alpha_{\mathrm{nf}}(\lambda) = \alpha_{\mathrm{bf}}(\lambda) + \alpha_{\mathrm{np}}(\lambda)$, and the attenuation of radiation propagating in the NF is given by the Beer-Lambert law:

$$E_\lambda(y) = E_\lambda \, e^{-\alpha_{nf}(\lambda)\, y} \, . \tag{6.1}$$

Here, y is the depth of penetrating light in reference to the top of the NF layer and E_λ is the incident spectral irradiance of the source. For homogeneous basefluids, $\alpha_{\mathrm{bf}}(\lambda) = 4\pi\kappa_{bf}/\lambda$, in which κ_{bf} is the basefluid optical extinction coefficient. The NP contribution to the absorption coefficient is given by:

$$\alpha_{np}(\lambda) = \frac{p}{V_{np}} \sigma_{abs}(\lambda) \, , \tag{6.2}$$

where V_{np} is the volume of a single NP and p is the sample volume fraction, defined as the ratio of the total volume of NPs to the volume of the NF.

To evaluate the absorption of solar energy by the NF layer of thickness H, the solar weighted absorption coefficient ($\mathrm{A_m}$) is used as an inportant FoM for the working fluid. The $\mathrm{A_m}$ is defined as the ratio between the absorbed energy and the incident solar energy [224]:

$$A_m = \frac{1}{E_0} \int_{\lambda_i}^{\lambda_f} E_\lambda \left[1 - e^{-\alpha_{nf}(\lambda) H}\right] d\lambda \, , \tag{6.3}$$

where $E_0 = \int_{\lambda_i}^{\lambda_f} E_\lambda d\lambda$ is the effective solar irradiance between λ_{i} and λ_{f}. Equation 6.3 shows that the efficiency of solar absorption is not only dependent on the optical parameters of the NF, but also relies on the thickness of the absorbing layer.

6.2.2 Spectral Joule number

Typically, a NP is considered efficient for photothermal applications if $\sigma_{\mathrm{sca}} < \sigma_{\mathrm{abs}}$ [86]. This criteria is the Albedo, defined as the ratio of the scattering cross section to the extinction cross section ($\sigma_{\mathrm{sca}}/\sigma_{\mathrm{ext}}$). Small Albedo is indicative of high absorption, while large Albedo denotes that most of the incident light is reflected. Moreover, the selection of NPs for colloidal nanofluids depends on several factors, such as desired thermal properties and cost-effectiveness. In general, the nanostructures used for solar harvesting should have a high absorption cross section across the broad solar emission spectrum. When choosing nanoparticles for thermal applications, those with a high absorption cross section (σ_{abs}) are preferred. High σ_{abs} values result in significant absorption of light energy, which in turn raises the temperature of the NPs. Increasing the size of particles generally enhances the absorption cross section. However, to achieve high light-to-heat conversion and effective heat loss, the volume of the NP should be minimized while its surface area should be maximized. Therefore, the size and morphology of NP are important in photothermal applications.

Joule number is a FoM that has been discussed in previous chapters for the appraisal of photothermal conversion. However, its use as a FoM to identify high performance nanoheaters is inappropriate when considering non-monocromatic (broadband) light excitation. To introduce an appropriate FoM, we need to assess broadband light sources influences photothermal performance. For a single nanosphere of radius $\mathrm{a_{np}}$ under solar irradiation, the steady-state heat equation is:

$$\begin{cases} \kappa_{np}\nabla^2 T_{np}(r) + \dot{Q}_{np} & = 0, \quad \mathrm{r} \leq \mathrm{a_{np}}, \\ \kappa_{nf}\nabla^2 T_{np}(r) & = 0, \quad \mathrm{r} > \mathrm{a_{np}}. \end{cases} \tag{6.4}$$

Here, κ_{np} and κ_{nf} are, respectively, the NP and NF thermal conductivities and $\dot{\mathrm{Q}}_{\mathrm{np}}$ is the NP heat source density ($\int_{\lambda_\mathrm{i}}^{\lambda_\mathrm{f}} \mathrm{E}_\lambda \sigma_{\mathrm{abs}}(\lambda)\mathrm{d}\lambda/\mathrm{V_{np}}$). Solving the conduction problem of Equation 6.4 in a medium of temperature T_∞ leads to solar contribution to the temperature:

$$T_{np}(r) - T_\infty = \begin{cases} \frac{\int_{\lambda_i}^{\lambda_f} E_\lambda \sigma_{abs}(\lambda) d\lambda}{4\pi\kappa_{np} a_{np}} \left[\frac{2\kappa_{np}+\kappa_{nf}}{2\kappa_{nf}} - \left(\frac{r}{a_{np}\sqrt{2}} \right)^2 \right] & , \quad \mathrm{r} \leq \mathrm{a_{np}} \\ \frac{\int_{\lambda_i}^{\lambda_f} E_\lambda \sigma_{abs}(\lambda) d\lambda}{4\pi\kappa_{nf} r} & , \quad \mathrm{r} > \mathrm{a_{np}}. \end{cases} \tag{6.5}$$

Notice that Equation 6.5 hold similarities to Equation 2.30. Therefore, for collective heating, the same assumption proposed in Equation 2.32 can be made, and the global temperature for an arbitrary macroscopic volume (V) becomes:

$$\Delta T_{global} = \frac{1}{4\pi\kappa_{nf}} \left[\frac{p}{V_{np}} \int_{\lambda_i}^{\lambda_f} E_\lambda \sigma_{abs}(\lambda) d\lambda \right] \int_V \frac{dV'}{r'} \, . \tag{6.6}$$

To select efficient nanoheaters for solar harvesting and assess NP efficacy to generate heat under broadband illumination, the Joule number (Equation 2.29) can be redefined considering the absorption cross section averaged over the illuminated spectral irradiance distribution, E_λ. Consequently, we introduce a new FoM, built upon Equation 6.6 and named Spectral Joule number ($\mathrm{SJ_o}$):

$$SJ_o = \frac{\lambda_{ref}}{2\pi V_{np}} \frac{\int_{\lambda_i}^{\lambda_f} E_\lambda \sigma_{abs}(\lambda)\, d\lambda}{\int_{\lambda_i}^{\lambda_f} E_\lambda \, d\lambda} = \frac{\lambda_{ref}}{2\pi V_{np} E_0} \int_{\lambda_i}^{\lambda_f} E_\lambda \sigma_{abs}(\lambda)\, d\lambda. \tag{6.7}$$

Notice that if volume fraction (p) is kept constant in Equation 6.6, the global temperature increase is proportional to Spectral Joule number ($\Delta\mathrm{T_{global}} \propto \mathrm{SJ_o}$). In particular, differently from $\mathrm{A_m}$, $\mathrm{SJ_o}$ does not depend on the DASC structural parameters (H), which makes $\mathrm{SJ_o}$ a suitable FoM to evaluate the capability of the NF to absorb solar radiation.

If the steady-state heat equation is directly applied to macroscopic heating, Beer absorption drives the heat source density ($\dot{\mathrm{Q}} = \int_{\lambda_i}^{\lambda_f} [\partial E_\lambda(y)/\partial y] d\lambda$):

$$\kappa_{nf} \nabla^2 T - \frac{p}{V_{np}} \int_{\lambda_i}^{\lambda_f} E_\lambda(y) \sigma_{abs}(\lambda) d\lambda = 0 \ . \tag{6.8}$$

For transparent samples, Equation 6.8 will result in global temperatures similar to Equation 6.6. However, Equation 6.8 reveals the heat source dependence on NF depth due to Beer attenuation, $\mathrm{E}_\lambda(\mathrm{y})$. If $\mathrm{y} = 0$, then $\mathrm{E}_\lambda(0) = \mathrm{E}_\lambda$, which implies that only absoption in transparent samples (small volume fractions) is proportional to $\mathrm{SJ_o}$. As solar irradiation penetrates the NF, the spectral irradiance is modified and $\mathrm{SJ_o}$ doesn't reflect the thermal performance anymore, which is better described by $\mathrm{A_m}$.

6.2.3 Finite Element Method simulation

FDM is an approximate method for solving partial differential equations. Its application involves the simple arithmetic derivation of the discretization equations to simplify the problem and compute solutions. Therefore, the original partial differential equation is transformed into a set of algebraic equations of which the solution is the approximate solution of the original boundary value problem [225]. In the simulation, solar radiation and the ambient temperature ($\mathrm{T_{amb}}$) are considered constant, and the flow velocity profile (U) is considered uniform. Temperature is obtained by solving the steady-state 2D heat transfer model, given, in this case, by [226]:

$$\kappa_{nf} \frac{\partial^2 T(x,y)}{\partial y^2} - \int_{\lambda_i}^{\lambda_f} \frac{\partial}{\partial y} E_\lambda(y) d\lambda = \rho_{nf} c_{nf} U \frac{\partial T(x,y)}{\partial x} \ , \tag{6.9}$$

where κ_{nf}, ρ_{nf} and $\mathrm{c_{nf}}$ are the thermal conductivity, density and specific heat of the NF, respectively. In Equation 6.9, heat is generated following absorption by Beer-Lambert law over the whole spectrum and is subjected to the following boundary conditions:

$$\kappa_{nf} \frac{\partial T(x,y)}{\partial y}\bigg|_{y=0} = h \left[T(0) - T_{amb} \right], \tag{6.10}$$

$$\kappa_{nf} \frac{\partial T(x,y)}{\partial y}\bigg|_{y=H} = 0, \text{ and} \tag{6.11}$$

$$T(x,y)\bigg|_{x=0} = T_{in} \ . \tag{6.12}$$

Equation 6.10 model thermal losses at the top of the collector due to convection, where h is the heat loss coefficient. As the collector is thermally insulated at the bottom, Equation 6.11 describes the adiabatic boundary condition, and the NF arrives at the inlet with initial temperature T_{in}, which is described by Equation 6.12. Furthermore, the outlet temperature of the collector is defined as the average NF temperature evaluated at x = L ($T_{out} = \langle T \rangle|_{x=L}$).

To solve Equation 6.9, the NF domain of Figure 27 was discretized into a rectangular mesh with horizontal (Δx) and vertical (Δy) spacing. The partial derivatives were approximated by [227]:

$$\frac{\partial T}{\partial x} = \frac{T(x+\Delta x) - T(x-\Delta x)}{2\Delta x}, \text{ and} \tag{6.13}$$

$$\frac{\partial^2 T}{\partial y^2} = \frac{T(y+\Delta y) - 2T(y) + T(y-\Delta y)}{\Delta y^2} \, . \tag{6.14}$$

6.3 MATERIALS AND METHODS

6.3.1 Polydopamine nanoparticle samples

Bovine serum albumin (BSA) stabilized samples of PDANSs were synthesized and gently provided to us by Ilia Goemaere (Biophotonics Research Group, Ghent University, Belgium). The physicochemical properties of the provided NPs are described in Table 4. For each NP size, vials containing total of $\sim$2 mL of PDA NPs were given.

Table 4 – Physicochemical properties of the provided polydopamine nanoparticles.

Hydrodynamic diameter (nm)	**Zeta potential (mV)**	**Concentration ($\mathbf{NPs/mL}$)**
135.3	-29.5	3.58×10^{12}
237.5	-19.1	2.82×10^{11}
290.8	-33.0	2.95×10^{12}
394.4	-26.8	2.30×10^{11}

All PDA NP samples studied were adjusted to equate the total mass of PDA among all samples. From the initial concentrations disclosed in Table 4, NP solutions were diluted in deionized water to produce a final volume of 500 $\mu\mathrm{L}$ containing 1.75 mg of PDA in the form of NPs. In sequence, the obtained dilutions were further diluted in 2.5 mL of deionized water, resulting in 3.0 mL samples with final mass concentration of 5.84×10^{-1} $\mathrm{mg/mL}$ ($\mathrm{p} = 3.8 \times 10^{-4}$).

6.3.2 Gold nanoparticle sample

Citrate-stabilized colloidal sample of 100 nm monodispersed AuNSs in deionized water (less than 12% variability in size and shape) was acquired from Sigma-Aldrich (Missouri, EUA).

2.0 mL of stock concentration at 2.55×10^{-2} $\mathrm{mg/mL}$ was reserved for solar irradiation.

6.3.3 Solar heating

Experimental evaluation of the photothermal conversion behavior of the NF involves the use of a solar simulator (Oriel LCS-100; Newport Corporation, Irvine, CA) as the light source to illuminate the samples, which are contained inside of a standard glass cuvette with optical length of 1 cm. The experimental setup is illustrated in Figure 26, in which a parabolic mirror (f = 100 mm) was used to directly focus solar radiation to the cuvette. The cuvette was placed within the Rayleigh length of beam to mimic a collimated source and beam width controlled adjusting the diaphragm. A thermal camera (Flir E4; Flir, Wilsonville, OR) was used to measure the average temperature of the illuminated section of the sample and record it with a frame rate of 3.7 fps. For each sample, the initial temperature equals the ambient temperature (25 ^{o}C), and the NF was irradiated for 30 minutes. The inset of Figure 26 contrasts the solar simulator spectral irradiance with the ASTM G173 AM 1.5 standard. In our experiments, we considered E_λ as the solar spectrum distribution of the ASTM International G173-based reference spectra, with AM1.5 between the wavelengths 280 nm and 980 nm, which covers nearly 73% of solar energy radiation.

Figure 26 – Experimental setup used to assess photothermal conversion of PDA bearing NFs. The simulator provides the solar irradiation that is focused by a fixed parabolic mirror (f = 100 mm). The beam width is controlled by a diaphragm. The cuvette is then filled by 3 mL of NF and positioned at the focus of the mirror. The thermal camera is used to acquire the temperature of the system and record the average increase over 30 minutes. Inset: spectral irradiance of solar simulator (red) and ASTM G173 AM 1.5 standard (black).

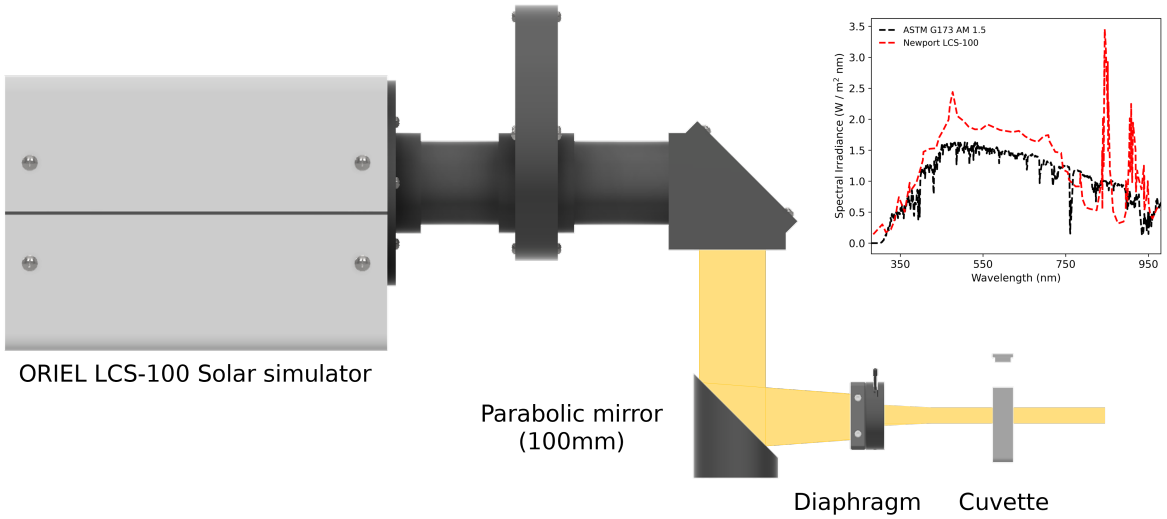

Source: belongs to the author.

6.3.4 Simulation of Direct Absorption Solar Collectors

The evaluation of solar collector performance is based on numerical modeling using the FDM to solve the heat equation for DASCs. For the sake of simplicity, the DASC was modeled in 2D and considered the flow of NF between two parallel surfaces, as shown in Figure 27. Figure 27A illustrates the DASC concept: solar radiation penetrates the DASC via the transparent cover perpendicularly and the energy absorbed by the NF is converted into heat, which is transported through the DASC for use elsewhere.

Figure 27 – **A.** DASC concept: solar radiation penetrates the DASC from the top, via the transparent cover. The energy absorbed by the NF is converted into heat and transported through the DASC. **B.** Schematic of 2D DASC illustrating the boundary conditions and the discretization strategy.

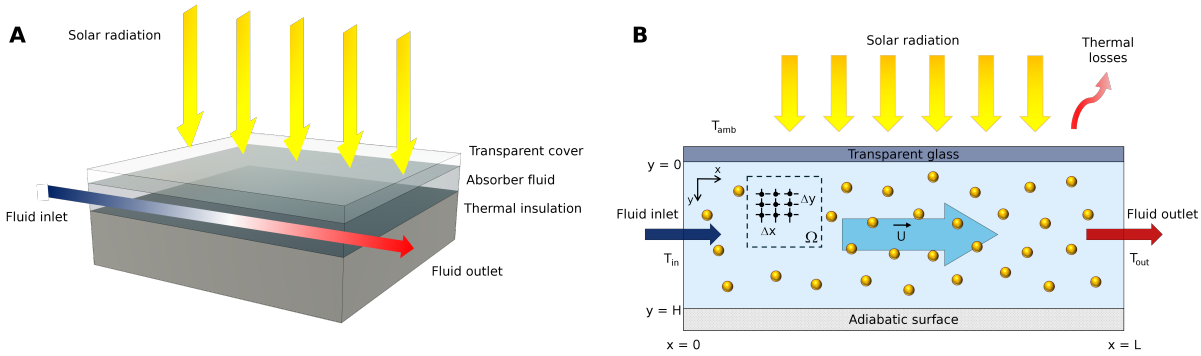

Source: belongs to the author.

Figure 27B portrays the 2D DASC model, where the top surface (y = 0) is the transparent glass cover of area $\mathrm{A_c} = 1$ m^2 and the bottom (y = H) is an adiabatic surface. Fluid flow occurs from inlet (x = 0) to outlet (x = L) and collector length is $\mathrm{L} = 1$ m. Thermal losses due to convection at the top of the collector are defined by the heat transfer coefficient ($\mathrm{h} = 10$ $\mathrm{W/m^2K}$ [228]). Figure 27 was discretized into a rectangular mesh with 5 mm spacing in the horizontal direction (Δx) and 1 μm spacing in the vertical direction (Δy). The obtained meshing configuration exhibited grid independence. To evaluate the temperature at the boundaries, one-sided finite difference schemes were used [227]. The Iterative Gauss-Seidel Method [225] was employed with convergence criterion of 10^{-4} of residual error in temperature values between consecutive iterations. An in-house FDM code was implemented using Python and is available in *Appendix A*. For low concentration of NPs, the thermophysical properties of NF are practically the same as those of the base fluid. Although in the present case the thermophysical characteristics of the NF won't change due to the low concentration regime, the dependence of such parameters was included in the code made available.

6.4 RESULTS AND DISCUSSIONS

Figure 28 illustrate the optical parameters of 100 nm PDANS in contrast with 100 nm AuNS within the spectral window of interest. Figures 28A and 28B are respectively the real and imaginary permittivities for gold (blue circles) and PDA (red triangles). The green dashed line of Figure 28A denotes the Fröhlich condition. The optical properties of PDA were extracted from ellipsometry data of thin films available in the literature [1]. Absorption in PDA NPs is dielectric (non-plasmonic) and arises from electronic transitions in conjugated π systems and cation-π interactions that are the product of the complex pathway of dopamine polymerization. This complexity provide sufficient conjugated structures within PDA NPs that can be understood as electron donor and acceptor pairs, which allows for a wide range of absorption [219].

Figure 28 – Optical parameters of 100 nm AuNS (blue circles) and 135 nm PDANS (red triangles). **A.** Real permittivity and Fröhlich condition (green dashed line). **B.** Imaginary permittivity. **C.** Normalized absorbance (experimental). **D**, **E** and **F.** absorption, scattering and extinction cross sections, respectively, obtained from Mie theory.

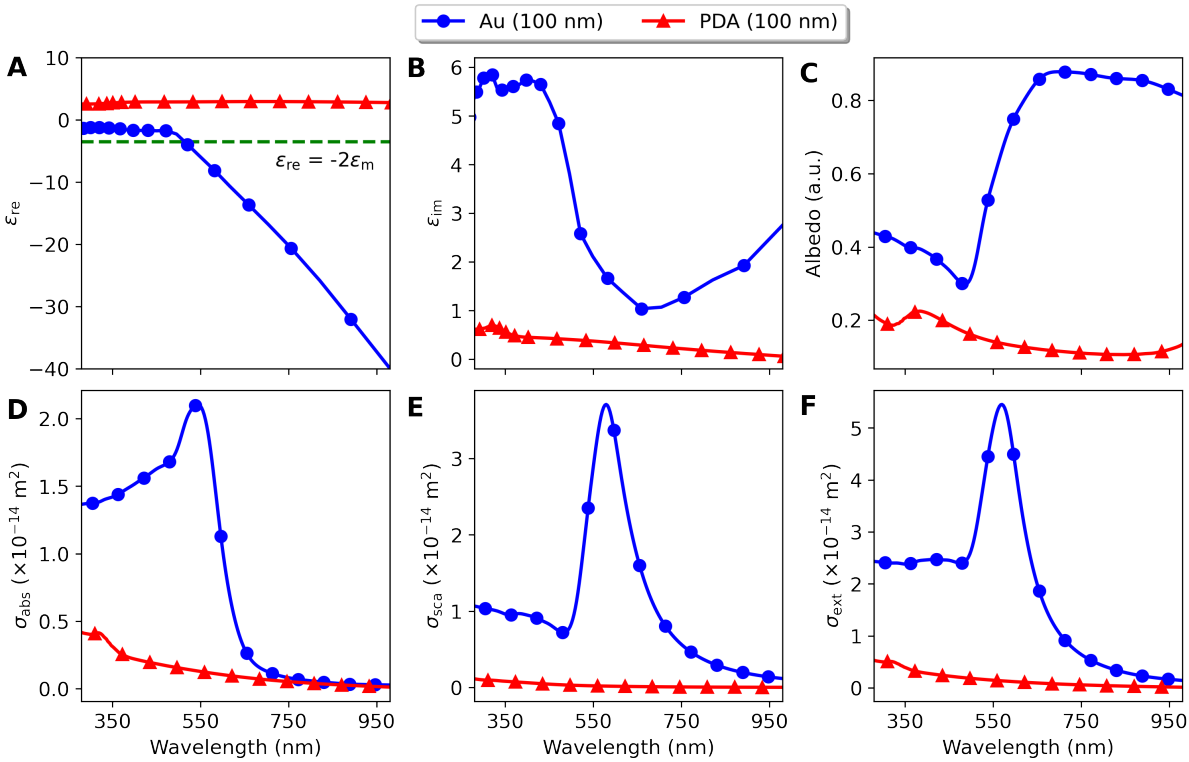

Source: belongs to the author.

Figure 28C delineate the wavelength dependence of the Albedo for 100 nm AuNS (blue circles) and 100 nm PDANS (red triangles). The AuNS show low Albedo (less than 50%) for wavelengths below 550 nm, but it rapidly increases for wavelengths above 550 nm. Simultaneously, the PDANS reveal Albedo values that remain under the AuNS across the whole analyzed spectrum (less than 35%). The sudden change in Albedo for the AuNS is due to its narrowband plasmon peak, that despite being pronounced, decays rapidly for wavelengths above

550 nm. Figures 28D, 28E and 28F are σ_{abs}, σ_{sca} and σ_{ext} for the 100 nm AuNS (blue circles) and PDANS (red triangles). In all cases, the optical cross sections for PDANS are about $10\times$ smaller than the cross sections for AuNS.

In complex nanomaterials such as PDA NPs, as the conjugated π system becomes larger, the bandgap of the NP becomes narrower and pushes the absorption to the visible spectrum [219]. The size dependence is illustrated in Figure 29, where the normalized extinction (experimental) of different PDANS samples are shown from dark red (135 nm) to dark blue (394 nm). The discontinuities observed in the spectra are likely caused by the change from UV to Vis illumination source in the spectrometer during acquisition.

Figure 29 – Normalized extinction (experimental) for PDANSs of size 135, 238, 291 and 394 nm. The discontinuities in spectrum are due to the change of illumination source in the spectrometer.

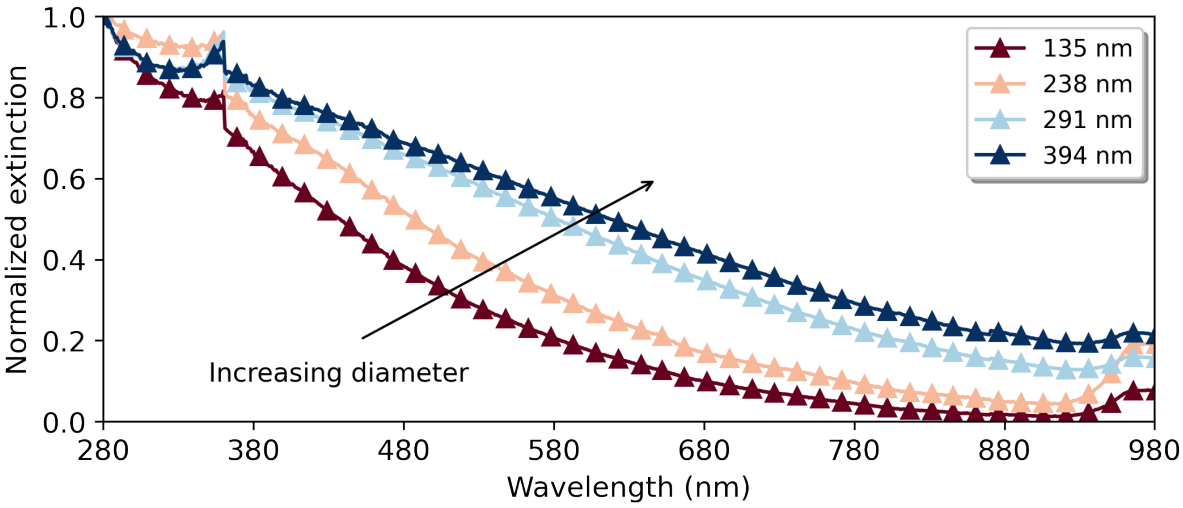

Source: belongs to the author.

For single NPs, the equilibrium temperature (ΔT_{np}) is small, as disclosed by Equation 6.5 and shown in Figure 30. Figures 30A and 30B are the equilibrium temperature profiles for AuNSs and PDANSs (respectively) for changing radius (a_{np}) as function normalized distance from the center of the NP (r/a_{np}). In both cases, the ΔT_{np} grows with NP radius. However, it rapidly saturates for AuNSs at small diameters (~ 90 nm), as scattering starts to dominate extinction and NP volume becomes too large. Such saturation is noticeable in the abrupt change of slope depicted in Figure 30C (blue circles), but doesn't occur for PDANSs at any of the considered radii, which results in larger ΔT_{np} for diameters larger than 400 nm (red triangles). For Figure 30C, ΔT_{np} at the surface of the NP was considered ($r = a_{np}$, gray dashed line). ΔT_{np} inside the NP ($r \leq a_{np}$) is highly dependent on NP thermal conductivity (κ_{np}). For gold ($\kappa_{np} = 315$ W/m K), high thermal conductivity promotes uniform heating inside the NP (Figure 30A), while for PDA ($\kappa_{np} = 0.2$ W/m K [216]), the low thermal conductivity highlights the parabolic equilibrium distribution inside the NP. Outside the NP ($r > a_{np}$), ΔT_{np} decays with $1/r$.

Figure 30 – **A.** Equilibrium temperature profile for AuNSs for changing radius as function normalized distance; **B.** Equilibrium temperature profile for PDANSs of changing radius as function normalized distance. The gray dashed line marks the NP surface ($r = a_{np}$). **C.** Equilibrium temperature profile of AuNSs (blue circles) and PDANSs (red circles) for different diameters. The equilibrium temperature at the NP surface was considered.

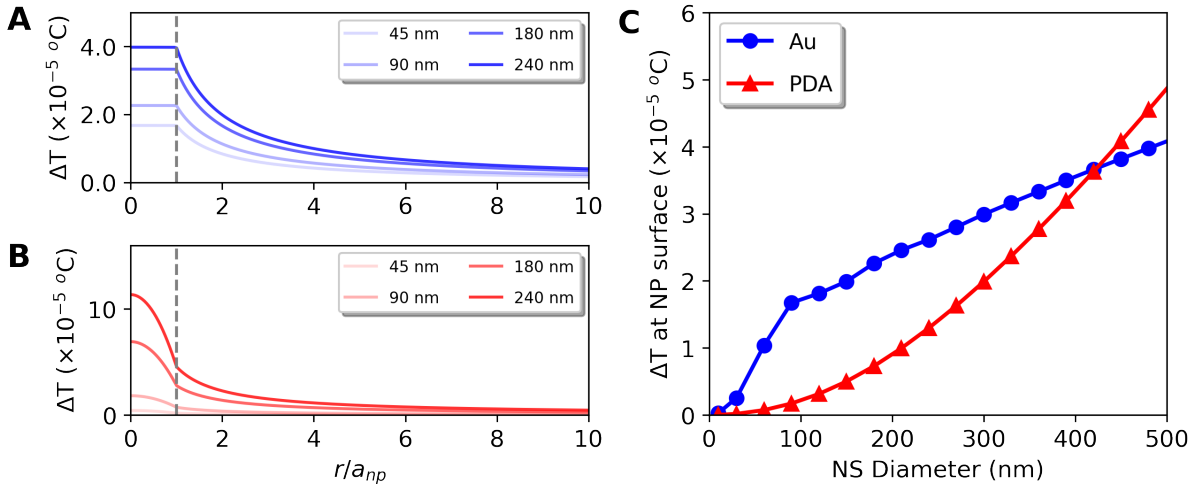

Source: belongs to the author.

The optimization of NPs for solar heating followed a theoretical approach using Mie Theory to obtain the optical cross sections of AuNSs and PDANSs in aqueous medium, with diameters ranging from 10 to 500 nm. The size dependent optical cross sections were then converted into SJ_o using Equation 6.7. Hence, SJ_o as function of NP diameter was obtained for differente sizes of AuNSs (blue circles) in Figure 31A and PDANSs (red triangles), as can be seen in Figure 31B. Spectral Joule number for AuNSs peaks around ∼60 nm with value of approximately 5.6, while PDANSs has maximum value $13\times$ smaller, about 0.44 at ∼180 nm.

Thermal evaluation was performed using the solar simulator source to compare the different samples of PDANSs. Figure 32A details the temperature behavior for each sample. The obtained results show that after 20 minutes of irradiation the temperature reached a plateau. Maximum temperature was obtained for the 238 nm PDANS sample, reaching an average of 34.9 °C, for an equivalent temperature increase of 9.9 °C. The worst performance was obtained for the sample of size 394 nm, reaching the average plateau temperature of 31.5 °C (temperature increase of 6.5 °C). In between the best and worse performances, the PDANSs of size 135 and 291 nm, the average temperature stabilized at around 33.1 °C and 32.4 °C, respectively, for a total temperature increase of 8.1 °C (135 nm) and 7.4 °C (291 nm). The trend indicate that temperature increase is proportional to the Spectral Joule number of the NP, as depicted in Figure 31B. Therefore, for increasing size, the final temperature followed the designated FoM. Similarly to what was observed for J_o (monochromatic light), the SJ_o can be used to infer the best NP size in a collective heating scenario, under broadband illumination.

Figure 31 – **A.** Spectral Joule number as function of AuNS diameter (blue circles) and **B.** Size dependence of Spectral Joule number for PDANSs (red triangles) of different sizes. The best $\mathrm{SJ_o}$ for AuNSs is $13\times$ larger than the best $\mathrm{SJ_o}$ for PDANSs.

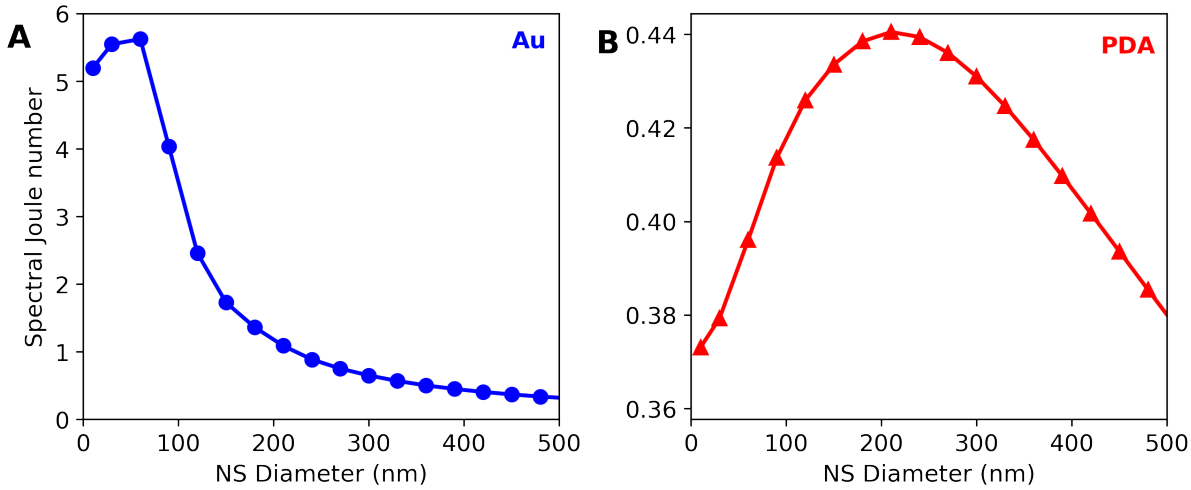

Source: belongs to the author.

Figures 32B–E are the thermographic stills taken under 30 minutes of continuous solar irradiation. The average temperature is the average value of the thermal pixels bounded by the boxed region. The results of the described thermal performances are summarized in Table 5.

Table 5 – Summary of the results obtained from the thermal evaluation among PDANS samples.

Diameter (nm)	$\mathbf{SJ_o}$	$\mathbf{T_{max}}$ **(°C)**	$\mathbf{\Delta T}$ **(°C)**
135.3	0.430	33.1	8.1
237.5	0.439	34.9	9.9
290.8	0.432	32.5	7.4
394.4	0.408	31.5	6.5

Subsequently, the thermo-optical performance of the NF containing the optimal PDANSs (238 nm, according to Table 5) was compared with a NF composed of 100 nm AuNSs, since gold is a reference material for photothermal plasmonic applications. Therefore, colloidal sample of AuNSs with diameter of 100 nm ($\mathrm{SJ_o} = 3.410$) was used. Following the intent of driving the costs of producing large scale solar collectors down, the seek for alternative solar absorbers is fundamental. Replacing Au by PDA as constituent of the NF for solar absorption might increase the competitiveness of DASC technologies. For a fair comparison, the total mass of material between the samples was made the same, thus, the 238 nm PDANS sample was further diluted to achieve the final concentration of 2.55×10^{-2} mg/mL, which was the stock concentration of the AuNS stock, resulting in a final sample volume of 2 mL. The volume fractions for the AuNS and PDANS specimens were 1.3×10^{-6} and 1.6×10^{-5}, respectively. Afterwards, the prepared samples were subjected to photothermal evaluation (Figure 33).

Figure 32 – Thermal evaluation of PDANS samples. **A.** Temporal evolution of the average temperature for each sample. All samples have the same mass concentration (5.84×10^{-1} mg/mL). Thermographic stills for samples of size **B.** 135 nm; **C.** 238 nm; **D.** 291 nm; and **E.** 394 nm under solar irradiation. The average temperature was defined as the average of the thermal pixels inside the boxed region.

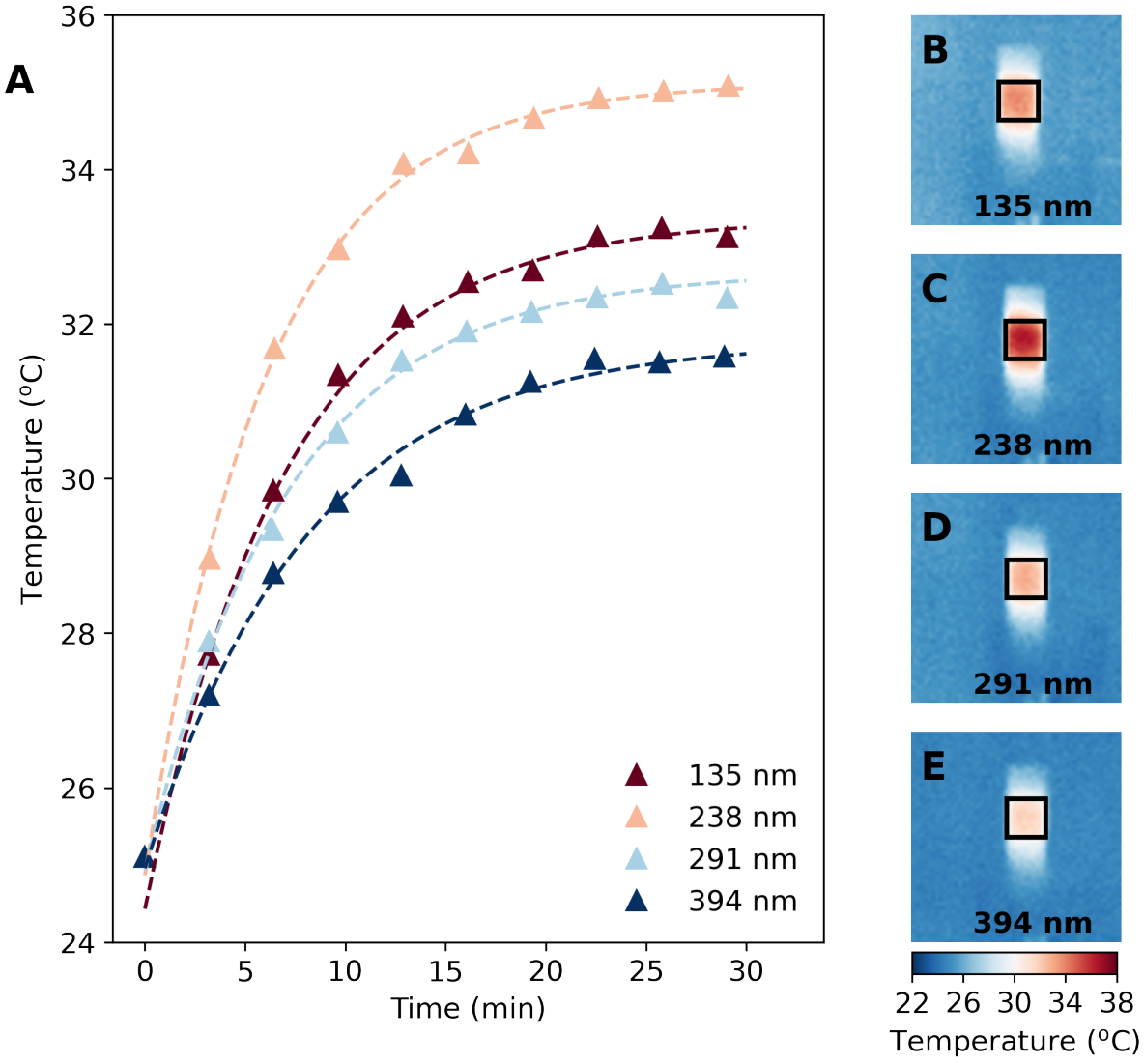

Source: belongs to the author.

Figure 33 – Comparison of photothermal performances of 238 nm PDANSs and 100 nm AuNSs under solar irradiation. **A.** Average temperature evolution for gold (blue circles) and PDA (red triangles) nanospheres. Solid lines with markers depict the best fit, while the background plot denotes the acquired data. Thermographic stills for **B.** 238 nm PDANSs; and **C.** 100 nm AuNSs after 30 minutes of solar irradiation.

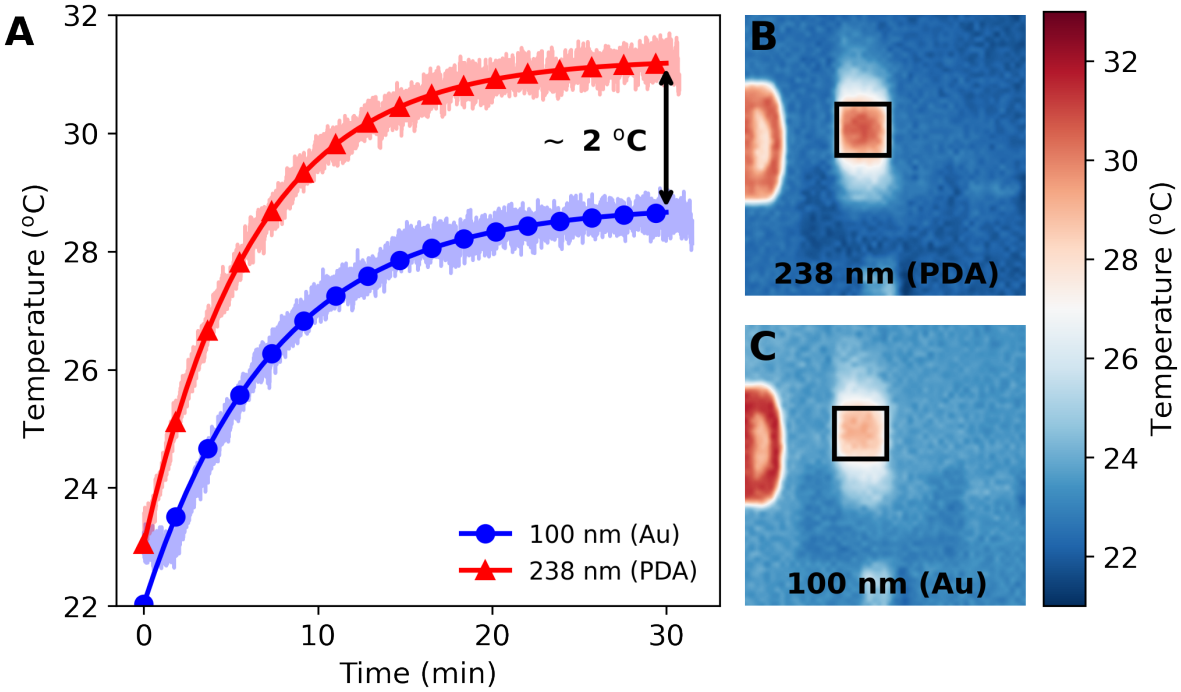

Source: belongs to the author.

In Figure 33A, the average temperatures for 238 nm PDANSs and 100 nm AuNSs are shown. The background plots (red and blue) are the actual measurements taken, while the solid lines with markers denotes the best fit of the experimental data. In average, the temperature of the NF containing AuNSs reached 28.1 °C, producing an effective temperature increase of approximately 5.2 °C. Despite of possessing smaller $\mathrm{SJ_o}$, the performance of 238 nm PDANS was superior to 100 nm AuNS. Nevertheless, the process of equating the total NP mass between samples implicate in volume fraction ratio of roughly $\mathrm{p_{PDA}}/\mathrm{p_{Au}} \approx 13\times$, which balances the difference in $\mathrm{SJ_o}$. Therefore, the same global equilibrium temperature was expected. However, the optimal PDA sample achieved 30.7 °C, for an effective temperature increase of 7.6 °C. Overall, while the comparison among PDA samples resulted in final temperature difference of almost 6 °C when contrasting the optimal (238 nm) and worst (394 nm) specimens (Figure 32A), the performance increase against the reference NF was of about 2 °C. Figures 33B and 33C are, respectively, the thermographic stills for the NFs containing 238 nm PDANSs and 100 nm AuNSs after 30 minutes of solar photothermal heating. Again, the average temperature was taken as the average thermal pixel inside the region bounded by the black box. Comparably, Zhang et al.[229] reported solar heating of gold nanoparticles in the range of 15 to 30 nm using solar simulator. For a concentration of 11.2×10^{-2} mg/mL, the bulk temperature of the sample

increased by $\sim 13\ \mathrm{K}$ in 5 minutes, without reaching thermal equilibrium.

Proceeding with the analysis of the photothermal performance of PDA nanospheres for enhanced solar absorption, the optimal NP size, disclosed in the previous assessment, was explored for DASC applications. Alongside, the performance of NFs containing 100 nm AuNSs in DASCs was also evaluated. As solar radiation penetrates the collector, energy is absorbed by the NF and the light intensity is reduced in accordance to Equation 6.1. Figures 34A and 34B are colormap depictions of the transmitted solar spectral irradiance through the DASC. Here, $\mathrm{H} = 1\ \mathrm{cm}$. In our FDM simulation, the volume fraction (p) was adjusted for each NP. This was done to keep the mass of NPs constant between NFs for each solar collector. The volume fraction was computed as:

$$p_{np} = \frac{M_{tot}}{\rho_{np}(A_c H) + M_{tot}}\ , \tag{6.15}$$

in which $\mathrm{M_{tot}}$ is the total mass of NP in the NF and ρ_{np} is the density of the NP material. Here, $\mathrm{m_{tot}}$ was upscaled taking into consideration the total mass of NPs used in the solar heating experiment $(5.09 \times 10^{-2}\ \mathrm{mg})$ and a scaling factor of 10^4 accounting for the dimensions of the solar collector, resulting in volume fractions of $\mathrm{p_{Au}} = 1.05 \times 10^{-5}$ and $\mathrm{p_{PDA}} = 1.34 \times 10^{-4}$. Again, the order of magnitude disparity observed between volume fractions arise from material density differences. For instance, the density of gold is 19.32 $\mathrm{g/cm^3}$, while the density of polydopamine was reported as 1.52 $\mathrm{g/cm^3}$ [230]. Figures 34C and 34E show the spectral irradiance at the top $(\mathrm{y/H} = 0)$ and bottom $(\mathrm{y/H} = 1)$ of the DASC. The blue and red filled area correspond to the absorbed radiation. The Au NF absorbs only 70% of the incident radiation due to its transparency between 650 nm and 980 nm, whereas, at the same conditions, the PDA NF absorbs most of the solar radiation, mostly due to its higher p.

The solar weighted coefficient (Equation 6.3) indicates that the transmitted light relies not only on the volumetric fraction of the NP, but also on the thickness of the DASC. Therefore, the optimization of absorption might also be pursued changing the NF thickness. Naturally, the thicker the NF layer, the best is the absorption. However, this is only advantageous until a certain height, as thicker absorbing layers accommodate NF volumes that can't sustain photothermal conversion, decreasing the overall temperature and hindering the thermal efficiency of the solar collector. Similarly, if volume fraction grows too large, the solar irradiation is quickly deposited near the DASC's surface, and the volumetric absorber strategy fails in the limit that it approaches a surface absorber, relapsing into the same issues that arose from thickness. The choice of p and H must, therefore, be carefully considered. Figure 35 illustrate the solar weighted coefficients for gold and PDA NFs with thicknesses up to $2.5\ \mathrm{cm}$ and volume fractions up to 5×10^{-5}. The results revealed that for the current configuration, AuNS NF present the highest $\mathrm{A_m}$ values for the majority of height and concentration scenarios (Figure 35A). For the designated height $(1\ \mathrm{cm})$, Figure 35B shows that larger PDA concentrations in the NF are needed for better use of the

Figure 34 – Spectral irradiance colormap along a NF layer ($\mathrm{H} = 1$ cm) for **A.** 100 nm AuNSs ($\mathrm{p} = 1.05 \times 10^{-5}$); and **B.** 238 nm PDANSs ($\mathrm{p} = 1.34 \times 10^{-4}$). Spectral irradiance for the normalized DASC thickness for **C.** 100 nm AuNSs ($\mathrm{p} = 1.05 \times 10^{-5}$); and **D.** 238 nm PDANSs ($\mathrm{p} = 1.34 \times 10^{-4}$). The blue and red dashed line correspond, respectively, to the spectral irradiance at the bottom of the collector. The filled area in between spectral irradiances correspond to the absorbed irradiation.

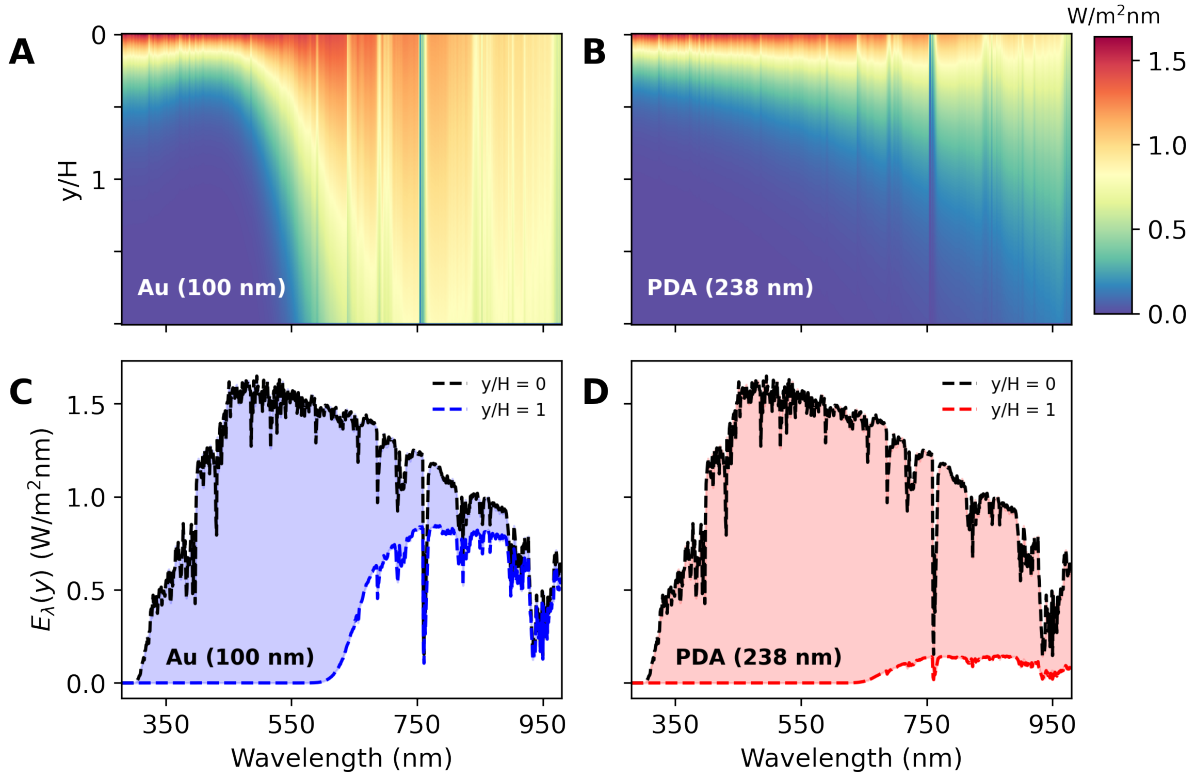

Source: belongs to the author.

solar irradiance, which corroborates the calculated volume fraction (1.34×10^{-4}).

Figure 35 – Solar weighted absorption coefficient as a function of volume fraction and height for **A.** 100 nm gold NF; and **B.** 238 nm PDA NF. $\mathrm{A_m}$ represents the percentage of the available solar power absorbed.

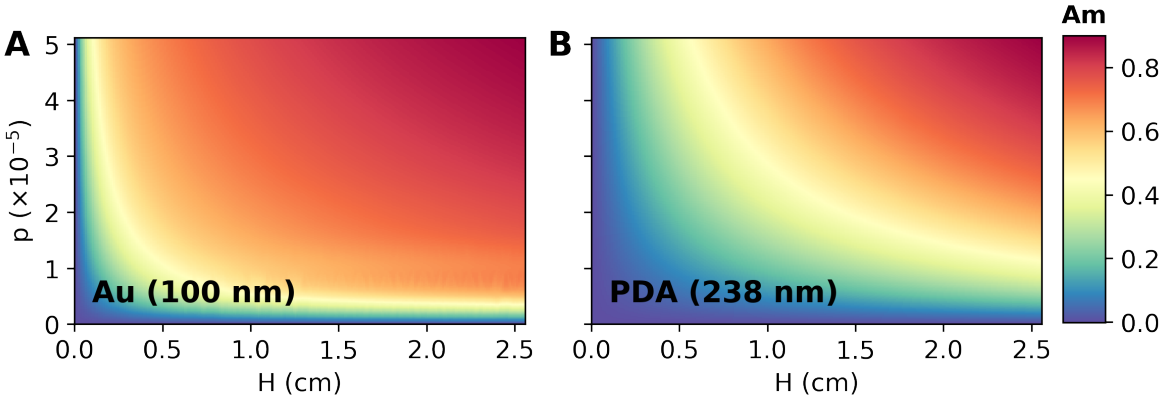

Source: belongs to the author.

Although $\mathrm{A_m}$ plots are generally good at showing the percentage of solar radiation absorbed by the DASC, they are incomplete and can't adequately predict other performance metrics of solar collectors. Numerical analysis of the temperature distribution in the solar collector domain helps to identify other DASC key performance parameters, such as output temperature, thermal efficiency and exergy efficiency. The DASC temperature distribution for gold and PDA nanofluids are shown in Figure 36. Here, $\mathrm{T_{in}} = \mathrm{T_{amb}} = 298\ \mathrm{K}$ and $U = 0.002\ \mathrm{m/s}$. The DASC using PDA NF has the best performance, with a temperature gain ($\Delta\mathrm{T} = \mathrm{T_{out}} - \mathrm{T_{in}}$) of 4.0 K (Figure 36B), while the DASC using the reference gold NF has $\Delta\mathrm{T} = 2.8\ \mathrm{K}$ (Figure 36A), a value 30% lower than the optimal PDA NF. Thermal efficiency of AuNS NF sample was estimated as $\eta_{\mathrm{th}} = 32.2\%$, while $\eta_{\mathrm{th}} = 45.6\%$ for the PDANS NF sample, and exergy efficiency was calculated to be $\eta_{\mathrm{ex}} = 0.3\%$ and $\eta_{\mathrm{ex}} = 0.6\%$ for 100 nm AuNSs and PDANSs, respectively.

Figure 36 – Temperature distribution for DASCs using **A.** gold (100 nm, $\mathrm{p} = 1.05 \times 10^{-5}$); and **B.** PDA (238 nm, $\mathrm{p} = 1.34 \times 10^{-4}$) NFs. The temperature profiles were obtained using FDM. For all simulations, $\mathrm{U} = 0.002\ \mathrm{m/s}$ and $\mathrm{H} = 1\ \mathrm{cm}$.

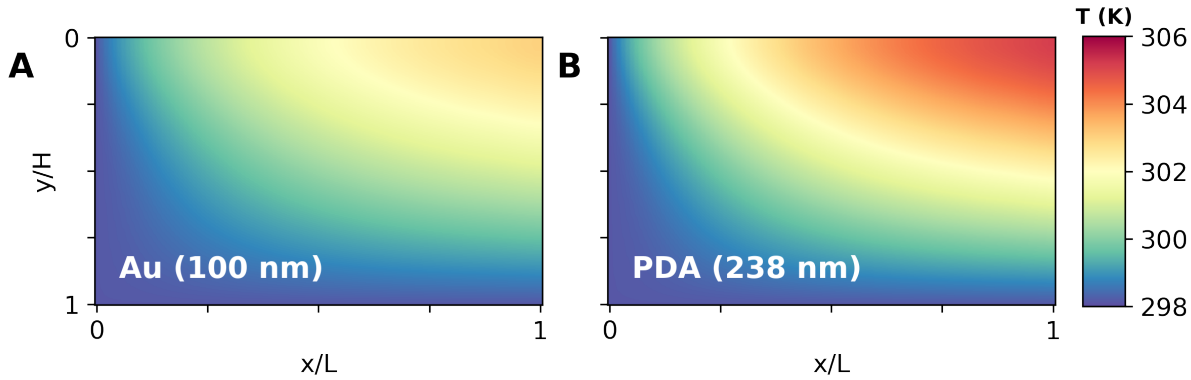

Source: belongs to the author.

The reported results for the PDA–based DASC implies that superior thermal performance can be achieved if PDA is used instead of Au in NFs for solar harvesting. Simultaneously, providing that the total mass of PDA and Au are equal, cost reduction can be achieved with no deterrent to thermal performance. Moreover, at volume fractions in which most of the solar radiation is absorbed for the NF containing PDANSs, the solar weighted coefficient for AuNS NF has far saturated and entered an inefficient thermal regime, which contributes to poor thermal performance in the Au–based DASC.

6.5 CONCLUSIONS

In this chapter, we established a framework for the optimization of photothermal performance for NFs employed in thermal solar harvesting. For this purpose, a new FoM was introduced, the Spectral Joule number ($\mathrm{SJ_o}$), that accounts for the collective contribution of all wavelengths within a spectral range to photothermal conversion, based on the absorption properties of the NP or NF system. As case study, the $\mathrm{SJ_o}$ was applied for the optimization of

polydopamine nanospheres, promising nanostructures with excellent absorption properties, following a size dependence approach. The theoretical analysis of $\mathrm{SJ_o}$ revealed that the optimal size for PDA nanospheres in water based NF has diameter of approximately $180\ \mathrm{nm}$. Additionally, the processes that influence the size dependence of optical absorption by polydopamine NPs were discussed.

To further test the hypothesis proposed with the introduction of the $\mathrm{SJ_o}$, an experimental photothermal assay using a commercial solar simulator to mimic the spectral solar irradiance in a controlled environment allowed the appraisal of light-to-heat capabilities in PDA nanospheres of distinct sizes, distributed around the predicted optimal nanosphere size. Therefore, diameters of 135, 238, 291 and 394 nm were selected for experimentation. The obtained results showed that maximum temperature was obtained for 238 nm, in which an average of 34.9 ºC was obtained, an equivalent temperature increase of 9.9 ºC against the 6.5 ºC achieved by the worst performer (394 nm). The observed trend suggest that the size dependence effect on temperature increase follow (or is proportional to) the calculated Spectral Joule number.

Furthermore, the use of PDA NFs as cost-effective alternatives to Au NFs was discussed. To this end, the performance of the NF containing polydopamine nanospheres of optimal diameter (238 nm) was compared to the effect of the same broadband heating in NF containing 100 nm AuNSs, maintaining the same total mass of NPs between samples. Experimentally, the optimal PDANS sample promoted temperature ~ 2.0 ºC above the Au–based NF. In average, the AuNS NF produced temperature increase of approximately 5.2 ºC, while the optimal PDANS NF achieved 7.6 ºC increase in temperature. Additionally, degradation of the absorber NPs in solar fluids over time is one of the key challenges for long term operation of DASCs. The stability of BSA stabilized PDA NPs was reported to remain stable after UV irradiation equivalent to 6.5 years of sunlight exposure [217].

To ascertain the relevance of this cost-reduction strategy for real world applications, the optical properties of NFs composed of polydopamine and gold NSs were calculated and applied to a two-dimensional heat transfer model, which allowed the evaluation of the photothermal performance of DASCs. Numerical analysis revealed that PDA provides better thermal efficiency (45.5%) when compared to gold NFs (32.2%), with temperature gains of $4.0\ \mathrm{K}$ and $2.8\ \mathrm{K}$, respectively. In spite of the obtained results, a more thorough analysis is necessary to evaluate key performance parameters of DASCs for changing inputs. For instance, the thermal performance of DASCs must be evaluated for PDA nanospheres of different diameters to assess the implications of size dependence to output temperature, thermal and exergy efficiencies. In-depth analysis of key performance parameters enable the forecast of more reliable results and facilitate the search for nanoheaters that might drive cost reduction of DASCs, increase the technology readiness level necessary to promote efficient low temperature solar heating and simplify the deployment of the technology.

Furthermore, the proposed FoM can be extended for use with other sources of broadband

light, such as LEDs. Nevertheless, for efficient nanoheater optimization under broadband light sources, the Spectral Joule number ($\mathrm{SJ_o}$) must be employed in conjunction with the solar weighted absorption coefficient ($\mathrm{A_m}$) to provide adequate estimates for each application.

7 CONCLUSIONS AND FUTURE PROSPECTS

7.1 CONCLUSIONS

In this thesis, the photothermal conversion reliance on NP size was the main concern of investigation. The understanding of photothermal and thermo-optical processes at the nanoscale is of fundamental importance to introduce new methodologies for the selection of efficient nanoheaters.

In this regard, first, **we focused on the establishment and use of optimization metrics upon which the evaluation of the photothermal behavior of NPs**, of distinct materials and shapes, could be performed under monochromatic and broadband excitation. Consequently, **three FoM were described for such purpose: (i) the Joule number** ($\mathbf{J_o}$) **for pulsed and cumulative heating; (ii) the Steady-State Factor** ($\mathbf{S^2F}$) **for CW irradiation in the context of an isolated single NP; and (iii) the Spectral Joule number** ($\mathbf{SJ_o}$) **for broadband illumination. The FoM were, thus, exploited in a framework in which the size (dimensions) of the NPs were modified to obtain optimized nanostructures.** As case study, AuNSs and AuNRs were chosen for theoretical optimization. The theoretical optimization was followed by the experimental assessment to verify the claims made, based on the FoM findings.

For AuNSs, theoretical analysis and thermal lens measurements allowed the identification of micro-degree temperature increase of laser heated colloidal samples of varying sizes. **The measurements show that the achieved TL global temperature resembles $\mathbf{J_o}$ behavior, and the optimal AuNS diameter for efficient colloidal laser heating in water was identified to be 50 nm. TL technique also enabled the estimation of intermediate steady-state temperature of a single particle, which was shown to resemble $\mathbf{S^2F}$ behavior with maximum performance expected for a diameter of 80 nm.**

For AuNRs in aqueous medium, optimization was performed for different laser lines (808 and 1064 nm). Our findings revealed that, **for AuNRs, smaller AuNR sizes are more efficient for photothermal conversion, as disclosed by $\mathbf{J_o}$. For single AuNRs, however, $\mathbf{S^2F}$ suggests that optimal performance is achieved for samples of size 90×25 and 150×30 nm for 808 and 1064 nm, respectively.** The assessment of AuNR was performed using thermal cameras, and the experiments corroborated theoretical findings through the evaluation of collective heating. Here, the **experimental results showed that if the same total mass of gold is used, collective heating follows the trend of $\mathbf{J_o}$.**

With the sizes of the optimized AuNSs and AuNRs in hand, **the effects of the optimal and sub-optimal NPs were examined in selected applications as PTI of *Candida albicans*, PTT of S180 in mice, PA generation and solar heating.**

The photothermal performance of the optimal and sub-optimal was probed for the the thermo-optic inactivation of *Candida albicans*, where we demonstrated that high temperatures of AuNR-fungal suspensions can be achieved (up to 55 ^{o}C) under 808 nm irradiation (1 W/cm^2). To properly analyse the effects of distinct NP size, the cytotoxicity of different PEGylated AuNR concentrations in the fungal samples were identified. Therefore, to avoid significant toxicity of the 90×25 nm AuNRs, sample concentrations used on photothermal assays were limited at 12.5 $\mu\mathrm{g/mL}$. In accordance with theoretical predictions, colloidal samples of AuNRs of size 41×10 nm achieved higher temperatures than 90×25 nm, under the same irradiation conditions.

In vivo photothermal therapy in S180-bearing mice was another selected application for the appraisal of size dependent temperature increase mediated by AuNRs. The obtained results showed that tumors inoculated with AuNRs demonstrated highly localized therapy, while irradiated groups with saline were not observed to reach useful temperatures, with the AuNR of size 41×10 nm producing temperatures capable of promoting cell death. This was further confirmed through the histological analysis, where the photothermal damage inflicted to tumor cells injected with AuNRs showed the formation of solid blocks of coagulative necrosis.

Following with the use of optimal and sub-optimal NPs in selected applications, AuNSs and AuNRs were probed to assess plasmon-mediated photoacoustic generation, where gold NPs in capillary tubes were used as a model for the investigation of the effect of NP size. Here, a PAM setup was explored. Distinct samples were prepared, accommodating fluids of colloidal gold of different shapes (NSs and NRs) and distinct sizes. Image analysis of PAM shown that AuNSs of 50 nm exhibits high $\mathrm{J_o}$ value and high performance on PA generation process, in accordance with theoretical predictions. Furthermore, the contrast enhancement among different NP sizes were reported. Despite the limitations of our experiment to demonstrate the optimization effect on AuNRs, the phenomena was still observed within the error margin.

Lastly, **the optimization framework was extended to support photothermal heating by broadband sources of light.** As case study, the photothermal performance of polydopamine based NFs for thermal solar harvesting was employed. For this purpose, **a new FoM was introduced, the Spectral Joule number ($\mathbf{SJ_o}$), that accounts for the collective contribution of all wavelengths within a spectral range to photothermal conversion, based on the absorptive properties of the system.** Following optimization protocol similar to the one used for the previously described FoM, the **$\mathbf{SJ_o}$ was applied for polydopamine nanospheres of different diameters. The theoretical analysis of $\mathbf{SJ_o}$ revealed that the optimal size for PDA nanospheres in water based NF has diameter of approximately 180 nm.** A commercial solar simulator was used to experimentally test PDA nanospheres of distinct sizes, distributed around the predicted optimal diameter. Therefore, diameters of 135, 238, 291 and 394 nm were selected for experimentation. The obtained results showed that maximum temperature was obtained for 238 nm, and **the observed trend suggested that the size dependence effect on temperature increase follows the calculated Spectral Joule number, as initially hypothesized.**

Furthermore, the performance of the NF containing polydopamine nanospheres of optimal diameter (238 nm) was compared with NF containing 100 nm AuNSs, maintaining the same total mass of NPs between samples as strategy to evaluate PDA–based NFs as a cost-effective alternative for Au–based NFs. Here, the optimal PDANS NF achieved temperatures higher than the 100 nm AuNS NF, despite of expecting similar thermal performance. Additionally, the optical properties of NFs composed of polydopamine and gold NSs were calculated and applied to a two-dimensional heat transfer model, which allowed the evaluation of the photothermal performance of DASCs. The numerical analysis revealed that PDA provides better thermal efficiency (45.5%) when compared to gold NFs (32.2%).

Moreover, all three figures of merit presented ($\mathrm{J_o}$, $\mathrm{S^2F}$ and $\mathrm{SJ_o}$) may be applied to optimize nanoheaters with materials other than the ones used to illustrate the applications. **The use of optimal nanoheaters may lead to a reduction in the amount of assimilated nanoparticles required to produce significant temperature increase. For PTI and PTT, this means enough temperature variation to induce cell death, while for PAM, it means higher imaging contrast, promoted by the stronger PA wave produced by the thermoelastic expansion of the medium. In bioapplications, the administration of doses containing smaller quantities of NPs may lead to less cytotoxicity, while simultaneously reducing the laser fluence required below the MPE to promote effective therapies. For solar applications, the use of alternative NP–based NFs increase has the potential to drive cost reduction without hindering thermal performances and simplify the deployment of DASCs.** Furthermore, the proposed FoM can be extended for use with other sources of broadband light, such as LEDs.

7.2 FUTURE PROSPECTS

Despite the experimental approaches used to assess the validity of the proposed FoM, the single NP nature of the Steady-state Factor imposes the evaluation of isolated NPs, if the proper assessment of $\mathrm{S^2F}$ is desired. Here, $\mathrm{S^2F}$ was evaluated using an indirect method that explores thermal lens heating of colloidal solutions of NPs. From the measured collective heating, a mathematical approach is used to estimate the intermediate temperature of a single NP before thermalization [87,91]. A direct (and consequently more precise) approach to evaluate $\mathrm{S^2F}$ is to dry cast a very diluted solution of NPs on coverslip and use dual thermal lens microscopy (TLM) to properly evaluate single NPs. The interparticle distance promoted by sample dilution might be enough to allow spatial probing of a single NP and appraise the size dependence of $\mathrm{S^2F}$ for both AuNSs and AuNRs. The technique is also suitable to optically assess the photoacoustic response of the mixture [231], which can be used to identify isolated NPs.

Furthermore, the described FoM are limited to NPs that doesn't have radiative transitions. Therefore, the FoM may be further modified to accommodate NPs with radiative relaxation, such as semiconductor NPs and quantum dots, by considering the quantum yield of radiative samples.

During photoheating experiments using anisotropic NPs such as AuNRs, results may

vary due to random angular orientation of AuNRs throughout the sample, as its orientation in reference to the polarization of the laser affects the absorption of light [27]. Therefore, the energy absorbed by the sample effectively decreases in half. NPs such as nanostars may be used to overcome this limitation, as they are quasi-isotropic and absorb the laser line in virtually any orientation. Additionally, they are capable of absorbing light at NIR wavelengths and have large surface area to volume ratio [147], traits suitable for thermal bioapplications.

Moreover, NP accumulation in the kidney lead to further complications. In general, AuNPs with diameters smaller than 5 nm can undergo renal clearance, while for larger NPs, surface charge and chemistry can optimize the excretion pathway [232,233]. The low melting point of gold-based NPs is another property that may be explored to promote innovative therapeutic approaches. Anisotropic NP shapes have the tendency to melt into spheres, the shape of maximum thermodynamic stability [8,234]. In this sense, to overcome kidney accumulation, the use of gold dimers [235,236] must be considered in engineering metamolecules capable of NIR PTT followed by breaking or detachment of the structure into pieces that can be excreted. NP melting and dimer splitting might be also probed using TLM coupled with dark-field mediated white light spectroscopy to detect structural changes.

In the realm of solar harvesting, in spite of the obtained results, a more thorough analysis is needed to properly evaluate key performance parameters of DASCs for changing inputs. This enables the forecast of more reliable results and facilitate the search for nanoheaters that will lead to the reduction of the concentration of NPs necessary to promote efficient solar harvesting for low temperature applications. Furthermore, the thermal performance of DASCs must be evaluated for PDA nanospheres of different diameters to assess the implications of size dependence to output temperature, thermal and exergy efficiencies.

7.3 CONTRIBUTIONS

The partial realization of this project resulted in the following works published in peer-reviewed journals:

- PEDROSA, T. L.; OLIVEIRA, G. M. F. ; PEREIRA, A. C. M. V. ; CRISPIM, M. J. B. DA S. ; SILVA, L. A. ; SILVA, M. S. ; SOUZA, I. A. ; MELO, A. M. M. A. ; GOMES, A. S. L. ; ARAUJO, R. E. **Tailoring Plasmonic Nanoheaters Size for Enhanced Theranostic Agent Performance**. Bioengineering-Basel, v. 11, p. 934, 2024. doi: 10.3390/bioengineering11090934 (Impact Factor = 3.8).

- OLIVEIRA, G. M. F. ; PEDROSA, T. L. ; ARAUJO, R. E. **Near Infrared photothermal inactivation of Candida albicans assisted by plasmonic nanorods**. Photodiagnosis and Photodynamic Therapy, v. 1, p. 104309, 2024. doi: 10.1016/j.pdpdt.2024.104309 (Impact Factor = 3.1).

- DE PEDROSA, TÚLIO L.; BOUDEBS, GEORGES; DE ARAUJO, RENATO E. **Evaluation of Plasmonic Optical Heating by Thermal Lens Spectroscopy**. Plasmonics. , v.1, p.1 - 6, 2023. doi: 10.1007/s11468-023-02120-4 (Impact Factor = 3.0).
- PEDROSA, TÚLIO DE L.; FAROOQ, SAJID; DE ARAUJO, RENATO E. **Selecting High-Performance Gold Nanorods for Photothermal Conversion**. Nanomaterials. , v.12, p.4188 - , 2022. doi: 10.3390/nano12234188 (Impact Factor = 5.3).
- PEDROSA, T. L.; ESTUPIÑÁN-LÓPEZ, C.; DE ARAUJO, R. E. **Temperature evaluation of colloidal nanoparticles by the thermal lens technique**. OPTICS EXPRESS. , v.28, p.31457 - , 2020. doi: 10.1364/OE.405172 (Impact Factor = 3.8).

Furthermore, an article authored by Túlio de L. Pedrosa, Gabrielli M. F. de Oliveira and Renato E. de Araujo, regarding PTI of *Candida albicans* and entitled *Near Infrared photothermal inactivation of Candida albicans assisted by plasmonic nanorods*, has been submitted for publication in Photodiagnosis and Photodynamic Therapy (Elsevier, Impact Factor = 3.1) and is currently under review. Other results reported in this thesis and not yet submitted will also be compiled into article format for future submission to peer reviewed journals.

The interaction with other researchers working on themes related to this project resulted in the publication or presentation of some works in conferences:

- PEDROSA, T. L.; PEREIRA, A. C. M. V. ; GOMES, A. S. L. ; ARAUJO, RENATO E. . **Size-dependence gold nanosphere mediated photoacoustic generation**. In: Nanoscale Imaging, Sensing and Actuation for Biomedical Applications XXI, SPIE Photonics West, Society of Photo-Optical Instrumentation Engineers (SPIE), 2024, San Francisco.
- PEDROSA, T. L.; OLIVEIRA, G. M. F. ; ARAUJO, RENATO E. . **Selecting plasmonic nanoheaters for photothermal inactivation of fungi**. In: Photonics North (PN 2023), 2023, Montreal.
- PEDROSA, T. L.; VITAL, C. V. P.; RATIVA, D.; GOMEZ-MALAGON, L. A.; ARAUJO, R. E. **Solar Harvesting Application with Gold Nanospheres: the Influence of Particle Size**. In: 2022 SBfoton International Optics and Photoncics Conference, 2022, Recife.
- PEDROSA, T. L. ; ESTUPIÑAN LOPEZ, CARLOS ; ARAUJO, RENATO E. . **Dual-beam thermal lens temperature measurement of colloidal nanoparticles**. In: Plasmonics: Design, Materials, Fabrication, Characterization, and Applications XIX, 2021, San Diego. Plasmonics: Design, Materials, Fabrication, Characterization, and Applications XIX, 2021. p. 65.
- PEDROSA, T. L. ; FAROOQ, S. ; ARAUJO, R. E. . **Otimização de Nanobastões de Ouro para Terapia Fototérmica de Alta Performance**. In: XXVII Congresso Brasileiro de Engenharia Biomédica (CBEB 2020), 2020, Vitória. Proceedings CBEB 2020, 2020.

- PEDROSA, TÚLIO L.; FAROOQ, SAJID ; DE ARAUJO, RENATO E. . **Selecting High Performance Plasmonic Nanostructures for Photothermal Therapy**. In: Clinical and Translational Biophotonics, 2020, Washington. Biophotonics Congress: Biomedical Optics 2020 (Translational, Microscopy, OCT, OTS, BRAIN). Washington: OSA, 2020. p. TW2B.6

The interaction with other researchers working on themes not directly related to this Project resulted in the publication or presentation of the following works in conferences:

- PEDROSA, T. L.; WACHSMANN-HOGIU, S. ; ARAUJO, RENATO E. . **Contact-mode fluorescence measurements on a lensless CMOS image sensor**. In: Nanoscale Imaging, Sensing and Actuation for Biomedical Applications XXI, SPIE Photonics West, Society of Photo-Optical Instrumentation Engineers (SPIE), 2024, San Francisco.
- BENEVIDES, C. ; PEDROSA, T. L. ; NEVES, W. ; MOURA, D. ; LIMA-NETO, R. ; ARAUJO, R. E. . **Desenvolvimento e Avaliação de Cabine de Radiação Ultravioleta para Desinfecção de Máscaras Hospitalares Descartáveis Durante a Pandemia de COVID-19**. In: XXVII Congresso Brasileiro de Engenharia Biomédica (CBEB 2020), 2020, Vitória. Proceedings CBEB 2020, 2020. p. 271-274.

Awards received for scientific and technical production:

- **Prizmatix Young Investigator Award** - Nanoscale Imaging, Sensing and Actuation for Biomedical Applications XXI, SPIE Photonics West, Society of Photo-Optical Instrumentation Engineers (SPIE), 2024.
- **1st Place - Antonio Fernando Catelli Infantosi Award - Best works** - XXVII Congresso Brasileiro de Engenharia Biomédica, Sociedade Brasileira de Engenharia Biomédica (SBEB), 2020.

BIBLIOGRAPHY

1 QIE, R.; MOGHADDAM, S. Z.; THORMANN, E. Parameterization of the optical constants of polydopamine films for spectroscopic ellipsometry studies. **Physical Chemistry Chemical Physics**, Royal Society of Chemistry (RSC), v. 23, n. 9, p. 5516–5526, 2021. ISSN 1463-9084. Disponível em: <http://dx.doi.org/10.1039/D0CP04796A>. Citado 3 vezes nas páginas 15, 92, and 148.

2 ALAMDARI, S. G. et al. Recent advances in nanoparticle-based photothermal therapy for breast cancer. **Journal of Controlled Release**, Elsevier BV, v. 349, p. 269–303, set. 2022. ISSN 0168-3659. Disponível em: <http://dx.doi.org/10.1016/j.jconrel.2022.06.050>. Citado na página 27.

3 KIM, M.; LEE, J.; NAM, J. Plasmonic photothermal nanoparticles for biomedical applications. **Advanced Science**, Wiley, v. 6, n. 17, jul. 2019. ISSN 2198-3844. Disponível em: <http://dx.doi.org/10.1002/advs.201900471>. Citado na página 27.

4 LI, Y. et al. Nanoparticle-on-mirror metamaterials for full-spectrum selective solar energy harvesting. **Nano Letters**, American Chemical Society (ACS), v. 22, n. 14, p. 5659–5666, jun. 2022. ISSN 1530-6992. Disponível em: <http://dx.doi.org/10.1021/acs.nanolett.2c00322>. Citado na página 27.

5 BAFFOU, G. **Thermoplasmonics Heating Metal Nanoparticles Using Light**. [S.l.]: Cambridge University Press, 2017. Citado 7 vezes nas páginas 27, 37, 39, 40, 42, 43, and 84.

6 NAEF, A. et al. Light-driven thermo-optical effects in nanoresonator arrays. **Advanced Optical Materials**, Wiley, v. 11, n. 20, set. 2023. ISSN 2195-1071. Disponível em: <http://dx.doi.org/10.1002/adom.202300698>. Citado na página 27.

7 MAHMOUDI, M. et al. Variation of protein corona composition of gold nanoparticles following plasmonic heating. **Nano Letters**, American Chemical Society (ACS), v. 14, n. 1, p. 6–12, dez. 2013. ISSN 1530-6992. Disponível em: <http://dx.doi.org/10.1021/nl403419e>. Citado na página 27.

8 TAYLOR, A. B.; SIDDIQUEE, A. M.; CHON, J. W. M. Below melting point photothermal reshaping of single gold nanorods driven by surface diffusion. **ACS Nano**, American Chemical Society (ACS), v. 8, n. 12, p. 12071–12079, nov. 2014. Disponível em: <https://doi.org/10.1021/nn5055283>. Citado 3 vezes nas páginas 27, 81, and 106.

9 BAFFOU, G. et al. Super-heating and micro-bubble generation around plasmonic nanoparticles under CW illumination. **The Journal of Physical Chemistry C**, American Chemical Society (ACS), v. 118, n. 9, p. 4890–4898, jan. 2014. Disponível em: <https://doi.org/10.1021/jp411519k>. Citado na página 27.

10 JONES, S. et al. Ultrafast modulation of thermoplasmonic nanobubbles in water. **Nano Letters**, American Chemical Society (ACS), v. 19, n. 11, p. 8294–8302, out. 2019. Disponível em: <https://doi.org/10.1021/acs.nanolett.9b03895>. Citado na página 27.

11 BURKETT, B. J. et al. A review of theranostics: Perspectives on emerging approaches and clinical advancements. **Radiology: Imaging Cancer**, Radiological

Society of North America (RSNA), v. 5, n. 4, jul. 2023. ISSN 2638-616X. Disponível em: <http://dx.doi.org/10.1148/rycan.220157>. Citado na página 27.

12 KRISHNAN, S.; DIAGARADJANE, P.; CHO, S. H. Nanoparticle-mediated thermal therapy: Evolving strategies for prostate cancer therapy. **International Journal of Hyperthermia**, Informa UK Limited, v. 26, n. 8, p. 775–789, set. 2010. Disponível em: <https://doi.org/10.3109/02656736.2010.485593>. Citado na página 27.

13 ABADEER, N. S.; MURPHY, C. J. Recent progress in cancer thermal therapy using gold nanoparticles. **The Journal of Physical Chemistry C**, American Chemical Society (ACS), v. 120, n. 9, p. 4691–4716, fev. 2016. Disponível em: <https://doi.org/10.1021/acs.jpcc.5b11232>. Citado 3 vezes nas páginas 27, 41, and 57.

14 LEI, W. et al. Polydopamine nanocoating for effective photothermal killing of bacteria and fungus upon near-infrared irradiation. **Adv. Mater. Interfaces**, Wiley, v. 3, n. 22, p. 1600767, nov. 2016. Citado 4 vezes nas páginas 27, 30, 56, and 85.

15 DOUGHTY, A. et al. Nanomaterial applications in photothermal therapy for cancer. **Materials**, MDPI AG, v. 12, n. 5, p. 779, mar. 2019. Disponível em: <https://doi.org/10.3390/ma12050779>. Citado na página 27.

16 SMITH, A. M.; MANCINI, M. C.; NIE, S. Second window for in vivo imaging. **Nature Nanotechnology**, Springer Science and Business Media LLC, v. 4, n. 11, p. 710–711, nov. 2009. Disponível em: <https://doi.org/10.1038/nnano.2009.326>. Citado na página 28.

17 MOGHAIEB, H. S. et al. Nanofluids for direct-absorption solar collectors—dascs: A review on recent progress and future perspectives. **Nanomaterials**, MDPI AG, v. 13, n. 7, p. 1232, mar. 2023. ISSN 2079-4991. Disponível em: <http://dx.doi.org/10.3390/nano13071232>. Citado 2 vezes nas páginas 28 and 84.

18 WANG, L. et al. A holistic and state-of-the-art review of nanotechnology in solar cells. **Sustain. Energy Technol. Assessments**, Elsevier BV, v. 54, n. 102864, p. 102864, dez. 2022. Citado na página 28.

19 VITAL, C. V. P. et al. Numerical assessment of transition metal nitrides nanofluids for improved performance of direct absorption solar collectors. **Appl. Therm. Eng.**, Elsevier BV, v. 190, n. 116799, p. 116799, maio 2021. Citado 3 vezes nas páginas 28, 33, and 84.

20 TYAGI, H.; PHELAN, P.; PRASHER, R. Predicted efficiency of a low-temperature nanofluid-based direct absorption solar collector. **Journal of Solar Energy Engineering**, ASME International, v. 131, n. 4, set. 2009. ISSN 1528-8986. Disponível em: <http://dx.doi.org/10.1115/1.3197562>. Citado na página 28.

21 IVANCIC, A. et al. **Solar Heating and Cooling Technology Roadmap**. [S.l.]: European Technology Platform on Renewable Heating and Cooling, 2014. <https://www.rhc-platform.org/content/uploads/2019/05/Solar_Thermal_Roadmap.pdf>. [Accessed 27-03-2024]. Citado na página 28.

22 CALDERONE, R. A.; FONZI, W. A. Virulence factors of candida albicans. **Trends in Microbiology**, Elsevier BV, v. 9, n. 7, p. 327–335, jul. 2001. Disponível em: <https://doi.org/10.1016/s0966-842x(01)02094-7>. Citado 2 vezes nas páginas 29 and 57.

23 SRIDHARAN, B.; LIM, H. G. Advances in photoacoustic imaging aided by nano contrast agents: special focus on role of lymphatic system imaging for cancer theranostics. **Journal of Nanobiotechnology**, Springer Science and Business Media LLC, v. 21, n. 1, nov. 2023. ISSN 1477-3155. Disponível em: <http://dx.doi.org/10.1186/s12951-023-02192-8>. Citado na página 29.

24 HYSI, E. et al. A tutorial in photoacoustic microscopy and tomography signal processing methods. **Journal of Applied Physics**, AIP Publishing, v. 129, n. 14, p. 141102, abr. 2021. Disponível em: <https://doi.org/10.1063/5.0040783>. Citado 3 vezes nas páginas 29, 72, and 73.

25 GUSEV, V. E.; KARABUTOV, A. A.; HENDZEL, K. **Laser Optoacoustics**. New York, NY: American Institute of Physics, 1993. Citado 2 vezes nas páginas 29 and 74.

26 NIEMZ, M. H. **Laser-Tissue Interactions**. Springer Berlin Heidelberg, 2007. Disponível em: <https://doi.org/10.1007/978-3-540-72192-5>. Citado 6 vezes nas páginas 29, 47, 63, 64, 66, and 75.

27 FAROOQ, S. et al. Thermo-optical performance of iron-doped gold nanoshells-based nanofluid on direct absorption solar collectors. **Solar Energy**, Elsevier BV, v. 208, p. 1181–1188, set. 2020. ISSN 0038-092X. Disponível em: <http://dx.doi.org/10.1016/j.solener.2020.08.068>. Citado 4 vezes nas páginas 29, 71, 84, and 106.

28 BALL, V. Polydopamine nanomaterials: Recent advances in synthesis methods and applications. **Frontiers in Bioengineering and Biotechnology**, Frontiers Media SA, v. 6, ago. 2018. ISSN 2296-4185. Disponível em: <http://dx.doi.org/10.3389/fbioe.2018.00109>. Citado 2 vezes nas páginas 30 and 85.

29 MATEO, D. et al. Fundamentals and applications of photo-thermal catalysis. **Chemical Society Reviews**, Royal Society of Chemistry (RSC), v. 50, n. 3, p. 2173–2210, 2021. ISSN 1460-4744. Disponível em: <http://dx.doi.org/10.1039/D0CS00357C>. Citado na página 33.

30 BOUCANOVA, M. d. P. et al. Single slope solar distiller performance using metallic nanofluids. **Solar Energy**, Elsevier BV, v. 245, p. 1–10, out. 2022. ISSN 0038-092X. Disponível em: <http://dx.doi.org/10.1016/j.solener.2022.08.065>. Citado na página 33.

31 DINIZ, F. L.; VITAL, C. V.; GóMEZ-MALAGóN, L. A. Parametric analysis of energy and exergy efficiencies of a hybrid pv/t system containing metallic nanofluids. **Renewable Energy**, Elsevier BV, v. 186, p. 51–65, mar. 2022. ISSN 0960-1481. Disponível em: <http://dx.doi.org/10.1016/j.renene.2021.12.151>. Citado 2 vezes nas páginas 33 and 84.

32 NGUYEN, V. P. et al. Chain-like gold nanoparticle clusters for multimodal photoacoustic microscopy and optical coherence tomography enhanced molecular imaging. **Nature Communications**, Springer Science and Business Media LLC, v. 12, n. 1, jan. 2021. ISSN 2041-1723. Disponível em: <http://dx.doi.org/10.1038/s41467-020-20276-z>. Citado na página 33.

33 ROCHE, P. J. R. et al. Real time plasmonic qpcr: how fast is ultra-fast? 30 cycles in 54 seconds. **The Analyst**, Royal Society of Chemistry (RSC), v. 142, n. 10, p. 1746–1755, 2017. ISSN 1364-5528. Disponível em: <http://dx.doi.org/10.1039/C7AN00304H>. Citado na página 33.

34 MOHAMMADYOUSEF, P. et al. Plasmonic and label-free real-time quantitative pcr for point-of-care diagnostics. **The Analyst**, Royal Society of Chemistry (RSC), v. 146, n. 18, p. 5619–5630, 2021. ISSN 1364-5528. Disponível em: <http://dx.doi.org/10.1039/D0AN02496A>. Citado na página 33.

35 SHIN, G.; LIM, D.; SHIN, D. Plasmonic heating effect in sers-based nanoplastic detection. **Sensors and Actuators B: Chemical**, Elsevier BV, v. 393, p. 134196, out. 2023. ISSN 0925-4005. Disponível em: <http://dx.doi.org/10.1016/j.snb.2023.134196>. Citado na página 33.

36 LIU, X. et al. Highly localized, efficient, and rapid photothermal therapy using gold nanobipyramids for liver cancer cells triggered by femtosecond laser. **Scientific Reports**, Springer Science and Business Media LLC, v. 13, n. 1, fev. 2023. ISSN 2045-2322. Disponível em: <http://dx.doi.org/10.1038/s41598-023-30526-x>. Citado 2 vezes nas páginas 33 and 73.

37 PORNNOPPADOL, G. et al. Cancer-targeting gold-decorated melanin nanoparticles for in vivo near-infrared photothermal therapy. **Molecular Systems Design & Engineering**, Royal Society of Chemistry (RSC), v. 9, n. 5, p. 507–517, 2024. ISSN 2058-9689. Disponível em: <http://dx.doi.org/10.1039/D3ME00173C>. Citado na página 33.

38 KOTSIFAKI, D. G.; CHORMAIC, S. N. The role of temperature-induced effects generated by plasmonic nanostructures on particle delivery and manipulation: a review. **Nanophotonics**, Walter de Gruyter GmbH, v. 11, n. 10, p. 2199–2218, abr. 2022. ISSN 2192-8614. Disponível em: <http://dx.doi.org/10.1515/nanoph-2022-0014>. Citado na página 33.

39 VASISTA, A. B. et al. Non–steady state thermometry with optical diffraction tomography. **Science Advances**, American Association for the Advancement of Science (AAAS), v. 10, n. 12, mar. 2024. ISSN 2375-2548. Disponível em: <http://dx.doi.org/10.1126/sciadv.adk5440>. Citado na página 33.

40 LEVI, A. F. J. The drude model. In: **Essential Classical Mechanics for Device Physics**. Morgan & Claypool Publishers, 2016, (2053-2571). p. 6–1 to 6–20. ISBN 978-1-6817-4413-1. Disponível em: <https://dx.doi.org/10.1088/978-1-6817-4413-1ch6>. Citado na página 33.

41 ROSS, M.; SCHATZ, G. Radiative effects in plasmonic aluminum and silver nanospheres and nanorods. **Journal of Physics D: Applied Physics**, v. 48, 05 2015. Citado 2 vezes nas páginas 34 and 39.

42 CORONADO, E.; SCHATZ, G. Surface plasmon broadening for arbitrary shape nanoparticles: A geometrical probability approach. **The Journal of Chemical Physics**, v. 119, p. 3926–3934, 08 2003. Citado na página 34.

43 BERCIAUD, S. et al. Observation of intrinsic size effects in the optical response of individual gold nanoparticles. **Nano Letters**, American Chemical Society (ACS), v. 5, n. 3, p. 515–518, mar. 2005. Disponível em: <https://doi.org/10.1021/nl050062t>. Citado 2 vezes nas páginas 34 and 35.

44 SöNNICHSEN, C. et al. Drastic reduction of plasmon damping in gold nanorods. **Physical Review Letters**, American Physical Society (APS), v. 88, n. 7, jan. 2002. Disponível em: <https://doi.org/10.1103/physrevlett.88.077402>. Citado na página 34.

45 PINCHUK, A.; KREIBIG, U.; HILGER, A. Optical properties of metallic nanoparticles: influence of interface effects and interband transitions. **Surface Science**, Elsevier BV, v. 557, n. 1–3, p. 269–280, maio 2004. ISSN 0039-6028. Disponível em: <http://dx.doi.org/10.1016/j.susc.2004.03.056>. Citado na página 34.

46 KREIBIG, U. Interface-induced dephasing of mie plasmon polaritons. **Applied Physics B**, Springer Science and Business Media LLC, v. 93, n. 1, p. 79–89, set. 2008. ISSN 1432-0649. Disponível em: <http://dx.doi.org/10.1007/s00340-008-3213-1>. Citado na página 34.

47 JOHNSON, P. B.; CHRISTY, R. W. Optical constants of the noble metals. **Physical Review B**, American Physical Society (APS), v. 6, n. 12, p. 4370–4379, dez. 1972. Disponível em: <https://doi.org/10.1103/physrevb.6.4370>. Citado 2 vezes nas páginas 34 and 47.

48 HERRERA, L. J. M. et al. Determination of plasma frequency, damping constant, and size distribution from the complex dielectric function of noble metal nanoparticles. **Journal of Applied Physics**, AIP Publishing, v. 116, n. 23, p. 233105, dez. 2014. Disponível em: <https://doi.org/10.1063/1.4904349>. Citado na página 35.

49 KHEIRANDISH, A.; JAVAN, N. S.; MOHAMMADZADEH, H. Modified drude model for small gold nanoparticles surface plasmon resonance based on the role of classical confinement. **Scientific Reports**, Springer Science and Business Media LLC, v. 10, n. 1, abr. 2020. ISSN 2045-2322. Disponível em: <http://dx.doi.org/10.1038/s41598-020-63066-9>. Citado na página 35.

50 KREIBIG, U.; VOLLMER, M. Introduction. In: **Optical Properties of Metal Clusters**. Springer Berlin Heidelberg, 1995. p. 1–12. Disponível em: <https://doi.org/10.1007/978-3-662-09109-8_1>. Citado na página 34.

51 BOHREN, C.; HUFFMAN, D. R. **Absorption and Scattering of Light by Small Particles**. [S.l.]: Wiley Science Paperback Series, 1983. Citado 4 vezes nas páginas 35, 36, 37, and 38.

52 XU, X. et al. Discrete dipole approximation simulation of the surface plasmon resonance of core/shell nanostructure and the study of resonance cavity effect. **The Journal of Physical Chemistry C**, American Chemical Society (ACS), v. 116, n. 45, p. 24046–24053, nov. 2012. Disponível em: <https://doi.org/10.1021/jp306238x>. Citado 2 vezes nas páginas 37 and 132.

53 COMSOL. **The Finite Element Method (FEM)**. 2016. <https://br.comsol.com/multiphysics/finite-element-method>. [Online; accessed 04-January-2019]. Citado 2 vezes nas páginas 37 and 135.

54 EUSTIS, S.; EL-SAYED, M. A. Determination of the aspect ratio statistical distribution of gold nanorods in solution from a theoretical fit of the observed inhomogeneously broadened longitudinal plasmon resonance absorption spectrum. **Journal of Applied Physics**, AIP Publishing, v. 100, n. 4, ago. 2006. ISSN 1089-7550. Disponível em: <http://dx.doi.org/10.1063/1.2244520>. Citado na página 37.

55 LINK, S.; MOHAMED, M. B.; EL-SAYED, M. A. Simulation of the optical absorption spectra of gold nanorods as a function of their aspect ratio and the effect of the medium dielectric constant. **The Journal of Physical Chemistry B**, American Chemical Society (ACS), v. 103, n. 16, p. 3073–3077, abr. 1999. ISSN 1520-5207. Disponível em: <http://dx.doi.org/10.1021/jp990183f>. Citado na página 37.

56 KELLY, K. L. et al. The optical properties of metal nanoparticles: the influence of size, shape, and dielectric environment. **The Journal of Physical Chemistry B**, American Chemical Society (ACS), v. 107, n. 3, p. 668–677, jan. 2003. Disponível em: <https://doi.org/10.1021/jp026731y>. Citado 2 vezes nas páginas 38 and 140.

57 LANGHAMMER, C. et al. Plasmonic properties of supported pt and pd nanostructures. **Nano Letters**, American Chemical Society (ACS), v. 6, n. 4, p. 833–838, mar. 2006. ISSN 1530-6992. Disponível em: <http://dx.doi.org/10.1021/nl060219x>. Citado na página 38.

58 KUMAR, C. (Ed.). **UV-VIS and Photoluminescence Spectroscopy for Nanomaterials Characterization**. Springer Berlin Heidelberg, 2013. Disponível em: <https://doi.org/10.1007/978-3-642-27594-4>. Citado na página 39.

59 THAKORE, V. et al. Thermoplasmonic response of semiconductor nanoparticles: A comparison with metals. **Advanced Theory and Simulations**, Wiley, v. 2, n. 1, p. 1800100, out. 2018. Disponível em: <https://doi.org/10.1002/adts.201800100>. Citado na página 39.

60 ZHAO, J. et al. Ag nanoframes: controllable reduction of AgClxBr1-x nanocubes. **Chemical Communications**, Royal Society of Chemistry (RSC), v. 55, n. 39, p. 5571–5574, 2019. Disponível em: <https://doi.org/10.1039/c9cc02240f>. Citado na página 39.

61 CLARK, B. D. et al. Aluminum nanocubes have sharp corners. **ACS Nano**, American Chemical Society (ACS), v. 13, n. 8, p. 9682–9691, ago. 2019. Disponível em: <https://doi.org/10.1021/acsnano.9b05277>. Citado na página 39.

62 YIN, Z. et al. Cu_3N nanocubes for selective electrochemical reduction of CO_2 to ethylene. **Nano Letters**, American Chemical Society (ACS), v. 19, n. 12, p. 8658–8663, nov. 2019. Disponível em: <https://doi.org/10.1021/acs.nanolett.9b03324>. Citado na página 39.

63 STEWART, J. W. et al. Ultrafast pyroelectric photodetection with on-chip spectral filters. **Nature Materials**, Springer Science and Business Media LLC, nov. 2019. Disponível em: <https://doi.org/10.1038/s41563-019-0538-6>. Citado na página 39.

64 SHERRY, L. et al. Localized surface plasmon resonance spectroscopy of single silver nanocubes. **Nano Letters**, v. 5, p. 2034–8, 11 2005. Citado na página 39.

65 JEON, H. B.; TSALU, P. V.; HA, J. W. Shape effect on the refractive index sensitivity at localized surface plasmon resonance inflection points of single gold nanocubes with vertices. **Scientific Reports**, Springer Science and Business Media LLC, v. 9, n. 1, set. 2019. Disponível em: <https://doi.org/10.1038/s41598-019-50032-3>. Citado 2 vezes nas páginas 39 and 73.

66 GENÇ, A. et al. Hollow metal nanostructures for enhanced plasmonics: synthesis, local plasmonic properties and applications. **Nanophotonics**, Walter de Gruyter GmbH, v. 6, n. 1, p. 193–213, set. 2016. Disponível em: <https://doi.org/10.1515/nanoph-2016-0124>. Citado na página 39.

67 FRANK, A. J. et al. Synthesis of silver nanoprisms with variable size and investigation of their optical properties: A first-year undergraduate experiment exploring plasmonic nanoparticles. **Journal of Chemical Education**, American Chemical Society (ACS), v. 87, n. 10, p. 1098–1101, out. 2010. Disponível em: <https://doi.org/10.1021/ed100166g>. Citado na página 39.

68 HABER, J.; SOKOLOV, K. Synthesis of stable citrate-capped silver nanoprisms. **Langmuir**, American Chemical Society (ACS), v. 33, n. 40, p. 10525–10530, set. 2017. Disponível em: <https://doi.org/10.1021/acs.langmuir.7b01362>. Citado na página 39.

69 ZHUO, X. et al. Colour routing with single silver nanorods. **Light: Science & Applications**, Springer Science and Business Media LLC, v. 8, n. 1, abr. 2019. Disponível em: <https://doi.org/10.1038/s41377-019-0150-1>. Citado na página 39.

70 CHEN, H. et al. Gold nanorods and their plasmonic properties. **Chem. Soc. Rev.**, Royal Society of Chemistry (RSC), v. 42, n. 7, p. 2679–2724, 2013. Disponível em: <https://doi.org/10.1039/c2cs35367a>. Citado na página 39.

71 GUTIÉRREZ, M. V.; SCARPETTINI, A. F. Kinetic and plasmonic properties of gold nanorods adsorbed on glass substrates. **Colloid and Interface Science Communications**, Elsevier BV, v. 33, p. 100213, nov. 2019. Disponível em: <https://doi.org/10.1016/j.colcom.2019.100213>. Citado na página 39.

72 BECKER, J. et al. The optimal aspect ratio of gold nanorods for plasmonic bio-sensing. **Plasmonics**, v. 5, p. 161–167, 06 2010. Citado na página 39.

73 VERRE, R. et al. Transition metal dichalcogenide nanodisks as high-index dielectric mie nanoresonators. **Nature Nanotechnology**, Springer Science and Business Media LLC, v. 14, n. 7, p. 679–683, maio 2019. Disponível em: <https://doi.org/10.1038/s41565-019-0442-x>. Citado na página 39.

74 ZORIĆ, I. et al. Gold, platinum, and aluminum nanodisk plasmons: Material independence, subradiance, and damping mechanisms. **ACS Nano**, American Chemical Society (ACS), v. 5, n. 4, p. 2535–2546, mar. 2011. Disponível em: <https://doi.org/10.1021/nn102166t>. Citado na página 39.

75 LAL, S. et al. Light interaction between gold nanoshells plasmon resonance and planar optical waveguides. **The Journal of Physical Chemistry B**, American Chemical Society (ACS), v. 106, n. 22, p. 5609–5612, jun. 2002. Disponível em: <https://doi.org/10.1021/jp014154s>. Citado na página 39.

76 RADLOFF, C.; HALAS, N. J. Plasmonic properties of concentric nanoshells. **Nano Letters**, American Chemical Society (ACS), v. 4, n. 7, p. 1323–1327, jul. 2004. Disponível em: <https://doi.org/10.1021/nl049597x>. Citado na página 39.

77 HUANG, L. et al. Plasmonic silver nanoshells for drug and metabolite detection. **Nature Communications**, Springer Science and Business Media LLC, v. 8, n. 1, ago. 2017. Disponível em: <https://doi.org/10.1038/s41467-017-00220-4>. Citado na página 39.

78 TRAN, K. T. M.; NGUYEN, T. D. Lithography-based methods to manufacture biomaterials at small scales. **Journal of Science: Advanced Materials and Devices**, Elsevier BV, v. 2, n. 1, p. 1–14, mar. 2017. Disponível em: <https://doi.org/10.1016/j.jsamd.2016.12.001>. Citado na página 39.

79 BALACHANDRAN, A. et al. Nanoparticle production via laser ablation synthesis in solution method and printed electronic application - a brief review. **Results in Engineering**, Elsevier BV, v. 16, p. 100646, dez. 2022. ISSN 2590-1230. Disponível em: <http://dx.doi.org/10.1016/j.rineng.2022.100646>. Citado na página 39.

80 ZULOAGA, J.; PRODAN, E.; NORDLANDER, P. Quantum plasmonics: Optical properties and tunability of metallic nanorods. **ACS Nano**, American Chemical Society (ACS), v. 4, n. 9, p. 5269–5276, ago. 2010. Disponível em: <https://doi.org/10.1021/nn101589n>. Citado na página 39.

81 MILAN, J.; NIEMCZYK, K.; KUS-LIśKIEWICZ, M. Treasure on the earth—gold nanoparticles and their biomedical applications. **Materials**, MDPI AG, v. 15, n. 9, p. 3355, maio 2022. ISSN 1996-1944. Disponível em: <http://dx.doi.org/10.3390/ma15093355>. Citado na página 39.

82 BAFFOU, G.; RIGNEAULT, H. Femtosecond-pulsed optical heating of gold nanoparticles. **Physical Review B**, American Physical Society (APS), v. 84, n. 3, jul. 2011. ISSN 1550-235X. Disponível em: <http://dx.doi.org/10.1103/physrevb.84.035415>. Citado na página 41.

83 KEBLINSKI, P. et al. Limits of localized heating by electromagnetically excited nanoparticles. **Journal of Applied Physics**, AIP Publishing, v. 100, n. 5, p. 054305, set. 2006. Disponível em: <https://doi.org/10.1063/1.2335783>. Citado 4 vezes nas páginas 41, 44, 45, and 76.

84 PEDROSA, T. de L.; FAROOQ, S.; ARAUJO, R. E. de. Selecting high-performance gold nanorods for photothermal conversion. **Nanomaterials**, MDPI AG, v. 12, n. 23, p. 4188, nov. 2022. Disponível em: <https://doi.org/10.3390/nano12234188>. Citado 9 vezes nas páginas 42, 44, 45, 53, 54, 55, 64, 74, and 131.

85 JAQUE, D. et al. Nanoparticles for photothermal therapies. **Nanoscale**, Royal Society of Chemistry (RSC), v. 6, n. 16, p. 9494–9530, 2014. Disponível em: <https://doi.org/10.1039/c4nr00708e>. Citado na página 41.

86 LALISSE, A. et al. Quantifying the efficiency of plasmonic materials for near-field enhancement and photothermal conversion. **The Journal of Physical Chemistry C**, American Chemical Society (ACS), v. 119, n. 45, p. 25518–25528, out. 2015. Disponível em: <https://doi.org/10.1021/acs.jpcc.5b09294>. Citado 2 vezes nas páginas 43 and 86.

87 PEDROSA, T. L. de; BOUDEBS, G.; ARAUJO, R. E. de. Evaluation of plasmonic optical heating by thermal lens spectroscopy. **Plasmonics**, Springer, p. 1–6, nov. 2023. Citado 8 vezes nas páginas 44, 45, 48, 51, 52, 55, 74, and 105.

88 BAFFOU, G.; QUIDANT, R.; ABAJO, J. Garcia de. Nanoscale control of optical heating in complex plasmonic systems. **ACS nano**, v. 4, p. 709–16, 02 2010. Citado 2 vezes nas páginas 44 and 45.

89 HAISS, W. et al. Determination of size and concentration of gold nanoparticles from UV-vis spectra. **Analytical Chemistry**, American Chemical Society (ACS), v. 79, n. 11, p. 4215–4221, abr. 2007. Disponível em: <https://doi.org/10.1021/ac0702084>. Citado na página 47.

90 PEREZJUSTE, J. et al. Gold nanorods: Synthesis, characterization and applications. **Coordination Chemistry Reviews**, Elsevier BV, v. 249, n. 17-18, p. 1870–1901, set. 2005. Disponível em: <https://doi.org/10.1016/j.ccr.2005.01.030>. Citado na página 48.

91 PEDROSA, T. L.; ESTUPIñáN-LóPEZ, C.; ARAUJO, R. E. de. Temperature evaluation of colloidal nanoparticles by the thermal lens technique. **Optics Express**, Optica

Publishing Group, v. 28, n. 21, p. 31457, out. 2020. ISSN 1094-4087. Disponível em: <http://dx.doi.org/10.1364/OE.405172>. Citado 2 vezes nas páginas 51 and 105.

92 HODAK, J. H.; HENGLEIN, A.; HARTLAND, G. V. Size dependent properties of au particles: Coherent excitation and dephasing of acoustic vibrational modes. **The Journal of Chemical Physics**, AIP Publishing, v. 111, n. 18, p. 8613–8621, nov. 1999. Disponível em: <https://doi.org/10.1063/1.480202>. Citado na página 52.

93 KAUR, S. et al. Photo-thermally enhanced antimicrobial efficacy of silver nanoplates against gram-negative, gram-positive bacterial and fungal pathogens. **Journal of Applied Microbiology**, Oxford University Press (OUP), v. 133, n. 2, p. 569–578, ago. 2022. ISSN 1364-5072. Disponível em: <http://dx.doi.org/10.1111/jam.15588>. Citado na página 56.

94 YAN, Z.; WANG, D.; GAO, Y. Nanomaterials for the treatment of bacterial infection by photothermal/photodynamic synergism. **Frontiers in Bioengineering and Biotechnology**, Frontiers Media SA, v. 11, maio 2023. Disponível em: <https://doi.org/10.3389/fbioe.2023.1192960>. Citado na página 56.

95 DEDIU, V. et al. Trends in photothermal nanostructures for antimicrobial applications. **International Journal of Molecular Sciences**, MDPI AG, v. 24, n. 11, p. 9375, maio 2023. Disponível em: <https://doi.org/10.3390/ijms24119375>. Citado na página 56.

96 SANTOS, K. F. dos et al. Fractal analysis and mathematical models for the investigation of photothermal inactivation of candida albicans using carbon nanotubes. **Colloids and Surfaces B: Biointerfaces**, Elsevier BV, v. 180, p. 393–400, ago. 2019. ISSN 0927-7765. Disponível em: <http://dx.doi.org/10.1016/j.colsurfb.2019.05.002>. Citado na página 56.

97 GHONIEM, D. F. et al. Novel photodynamic/photothermal treatment of fungal keratitis using rose bengal-loaded polypyrrole-gold nanoparticles in wistar albino rats. **J. Ocul. Pharmacol. Ther.**, Mary Ann Liebert Inc, v. 39, n. 6, p. 379–388, jul. 2023. Citado na página 56.

98 BERMúDEZ-JIMéNEZ, C. et al. Effective control of biofilms by photothermal therapy using a gold nanorod hydrogel. **Journal of Biomedical Materials Research Part B: Applied Biomaterials**, Wiley, v. 108, n. 2, p. 333–342, abr. 2019. ISSN 1552-4981. Disponível em: <http://dx.doi.org/10.1002/jbm.b.34392>. Citado na página 56.

99 RODRIGUES, M. L.; NOSANCHUK, J. D. Recognition of fungal priority pathogens: What next? **PLOS Neglected Tropical Diseases**, Public Library of Science (PLoS), v. 17, n. 3, p. e0011136, mar. 2023. Disponível em: <https://doi.org/10.1371/journal.pntd.0011136>. Citado na página 56.

100 RAYENS, E.; NORRIS, K. A. Prevalence and healthcare burden of fungal infections in the united states, 2018. **Open Forum Infectious Diseases**, Oxford University Press (OUP), v. 9, n. 1, jan. 2022. Disponível em: <https://doi.org/10.1093/ofid/ofab593>. Citado na página 56.

101 TURNER, S. A.; BUTLER, G. The candida pathogenic species complex. **Cold Spring Harbor Perspectives in Medicine**, Cold Spring Harbor Laboratory, v. 4, n. 9, p. a019778–a019778, set. 2014. Disponível em: <https://doi.org/10.1101/cshperspect.a019778>. Citado na página 56.

102 SANTOS, G. C. de O. et al. Candida infections and therapeutic strategies: Mechanisms of action for traditional and alternative agents. **Frontiers in Microbiology**, Frontiers Media SA, v. 9, jul. 2018. Disponível em: <https://doi.org/10.3389/fmicb.2018.01351>. Citado na página 57.

103 ALI, M. R. K.; WU, Y.; EL-SAYED, M. A. Gold-nanoparticle-assisted plasmonic photothermal therapy advances toward clinical application. **The Journal of Physical Chemistry C**, American Chemical Society (ACS), v. 123, n. 25, p. 15375–15393, maio 2019. ISSN 1932-7455. Disponível em: <http://dx.doi.org/10.1021/acs.jpcc.9b01961>. Citado na página 57.

104 HUANG, X. et al. Advances and applications of nanoparticles in cancer therapy. **MedComm – Oncology**, Wiley, v. 3, n. 1, mar. 2024. ISSN 2769-6448. Disponível em: <http://dx.doi.org/10.1002/mog2.67>. Citado na página 57.

105 DING, X. et al. Surface plasmon resonance enhanced light absorption and photothermal therapy in the second near-infrared window. **Journal of the American Chemical Society**, American Chemical Society (ACS), v. 136, n. 44, p. 15684–15693, out. 2014. Disponível em: <https://doi.org/10.1021/ja508641z>. Citado na página 57.

106 MENDES, R. et al. Photothermal enhancement of chemotherapy in breast cancer by visible irradiation of gold nanoparticles. **Scientific Reports**, Springer Science and Business Media LLC, v. 7, n. 1, set. 2017. Disponível em: <https://doi.org/10.1038/s41598-017-11491-8>. Citado na página 57.

107 HIRSCH, L. R. et al. Nanoshell-mediated near-infrared thermal therapy of tumors under magnetic resonance guidance. **Proceedings of the National Academy of Sciences**, Proceedings of the National Academy of Sciences, v. 100, n. 23, p. 13549–13554, nov. 2003. Disponível em: <https://doi.org/10.1073/pnas.2232479100>. Citado na página 57.

108 DICKERSON, E. B. et al. Gold nanorod assisted near-infrared plasmonic photothermal therapy (PPTT) of squamous cell carcinoma in mice. **Cancer Letters**, Elsevier BV, v. 269, n. 1, p. 57–66, set. 2008. Disponível em: <https://doi.org/10.1016/j.canlet.2008.04.026>. Citado na página 57.

109 WANG, Y. et al. Comparison study of gold nanohexapods, nanorods, and nanocages for photothermal cancer treatment. **ACS Nano**, American Chemical Society (ACS), v. 7, n. 3, p. 2068–2077, fev. 2013. Disponível em: <https://doi.org/10.1021/nn304332s>. Citado 3 vezes nas páginas 57, 60, and 66.

110 MACKEY, M. A. et al. The most effective gold nanorod size for plasmonic photothermal therapy: Theory and in vitro experiments. **The Journal of Physical Chemistry B**, American Chemical Society (ACS), v. 118, n. 5, p. 1319–1326, jan. 2014. Disponível em: <https://doi.org/10.1021/jp409298f>. Citado na página 57.

111 PATTANI, V. P. et al. Role of apoptosis and necrosis in cell death induced by nanoparticle-mediated photothermal therapy. **Journal of Nanoparticle Research**, Springer Science and Business Media LLC, v. 17, n. 1, jan. 2015. Disponível em: <https://doi.org/10.1007/s11051-014-2822-3>. Citado 3 vezes nas páginas 57, 69, and 70.

112 ZHANG, Y. et al. Temperature-dependent cell death patterns induced by functionalized gold nanoparticle photothermal therapy in melanoma cells. **Scientific Reports**, Springer Science and Business Media LLC, v. 8, n. 1, jun. 2018. Disponível em: <https://doi.org/10.1038/s41598-018-26978-1>. Citado 3 vezes nas páginas 57, 64, and 69.

113 CHEN, J. et al. Immuno gold nanocages with tailored optical properties for targeted photothermal destruction of cancer cells. **Nano Letters**, American Chemical Society (ACS), v. 7, n. 5, p. 1318–1322, maio 2007. Disponível em: <https://doi.org/10.1021/nl070345g>. Citado na página 57.

114 CHEN, J. et al. Gold nanocages as photothermal transducers for cancer treatment. **Small**, Wiley, v. 6, n. 7, p. 811–817, abr. 2010. Disponível em: <https://doi.org/10.1002/smll.200902216>. Citado na página 57.

115 ZHANG, B. et al. Self-reporting gold nanourchins for tumor-targeted chemo-photothermal therapy integrated with multimodal imaging. **Advanced Therapeutics**, Wiley, v. 3, n. 10, jul. 2020. ISSN 2366-3987. Disponível em: <http://dx.doi.org/10.1002/adtp.202000114>. Citado na página 57.

116 XIONG, Y. et al. Nanoparticle-based photothermal therapy for breast cancer noninvasive treatment. **Advanced Materials**, Wiley, nov. 2023. ISSN 1521-4095. Disponível em: <http://dx.doi.org/10.1002/adma.202305140>. Citado na página 57.

117 KUMAR, P.; SRIVASTAVA, R. **Nanomedicine for Cancer Therapy**. Springer International Publishing, 2017. Disponível em: <https://doi.org/10.1007/978-3-319-45826-7>. Citado na página 57.

118 BERTRAND, N. et al. Cancer nanotechnology: The impact of passive and active targeting in the era of modern cancer biology. **Advanced Drug Delivery Reviews**, Elsevier BV, v. 66, p. 2–25, fev. 2014. Disponível em: <https://doi.org/10.1016/j.addr.2013.11.009>. Citado na página 57.

119 CUENCA, A. G. et al. Emerging implications of nanotechnology on cancer diagnostics and therapeutics. **Cancer**, Wiley, v. 107, n. 3, p. 459–466, 2006. Disponível em: <https://doi.org/10.1002/cncr.22035>. Citado na página 57.

120 PAN, Y.; BARTNECK, M.; JAHNEN-DECHENT, W. Cytotoxicity of gold nanoparticles. In: **Methods in Enzymology**. Elsevier, 2012. p. 225–242. Disponível em: <https://doi.org/10.1016/b978-0-12-391858-1.00012-5>. Citado na página 57.

121 ZHU, X. et al. Cellular uptake behaviour, photothermal therapy performance, and cytotoxicity of gold nanorods with various coatings. **Nanoscale**, Royal Society of Chemistry (RSC), v. 6, n. 19, p. 11462–11472, ago. 2014. Disponível em: <https://doi.org/10.1039/c4nr03865g>. Citado 2 vezes nas páginas 57 and 61.

122 CONTINI, C. et al. Size dependency of gold nanoparticles interacting with model membranes. **Communications Chemistry**, Springer Science and Business Media LLC, v. 3, n. 1, set. 2020. ISSN 2399-3669. Disponível em: <http://dx.doi.org/10.1038/s42004-020-00377-y>. Citado na página 57.

123 SOUSA-JUNIOR, A. A. et al. Immunogenic cell death photothermally mediated by erythrocyte membrane-coated magnetofluorescent nanocarriers improves survival in sarcoma model. **Pharmaceutics**, MDPI AG, v. 15, n. 3, p. 943, mar. 2023. ISSN 1999-4923. Disponível em: <http://dx.doi.org/10.3390/pharmaceutics15030943>. Citado na página 57.

124 STOCK, C. C. et al. Sarcoma 180 inhibition screening data. **Cancer Research**, American Association for Cancer Research, n. 15, p. 179, dez. 1955. ISSN 1538-7445.

Disponível em: <https://aacrjournals.org/cancerres/article/15/Supplement_2/179/473242/Sarcoma-180-Inhibition-Screening-Data1>. Citado na página 57.

125 SOUSA, E. L. d. et al. Antitumor activity of leaves of himatanthus drasticus (mart.) plumel-apocynaceae (janaguba) in the treatment of sarcoma 180 tumor. **Brazilian Journal of Pharmaceutical Sciences**, FapUNIFESP (SciELO), v. 46, n. 2, p. 199–203, jun. 2010. ISSN 1984-8250. Disponível em: <http://dx.doi.org/10.1590/S1984-82502010000200005>. Citado na página 58.

126 JANA, S. et al. Antitumorigenic potential of linalool is accompanied by modulation of oxidative stress: An in vivo study in sarcoma-180 solid tumor model. **Nutrition and Cancer**, Informa UK Limited, v. 66, n. 5, p. 835–848, abr. 2014. ISSN 1532-7914. Disponível em: <http://dx.doi.org/10.1080/01635581.2014.904906>. Citado na página 58.

127 AFLAKIAN, F. et al. Nanoparticles-based therapeutics for the management of bacterial infections: A special emphasis on fda approved products and clinical trials. **European Journal of Pharmaceutical Sciences**, Elsevier BV, v. 188, p. 106515, set. 2023. ISSN 0928-0987. Disponível em: <http://dx.doi.org/10.1016/j.ejps.2023.106515>. Citado na página 58.

128 SIBUYI, N. R. S. et al. Multifunctional gold nanoparticles for improved diagnostic and therapeutic applications: A review. **Nanoscale Research Letters**, Springer Science and Business Media LLC, v. 16, n. 1, dez. 2021. ISSN 1556-276X. Disponível em: <http://dx.doi.org/10.1186/s11671-021-03632-w>. Citado na página 58.

129 National Academies Press. **Guide for the care and use of laboratory animals**. 8. ed. Washington, D.C., DC: National Academies Press, 2014. Citado na página 59.

130 JETT, B. D. et al. Simplified agar plate method for quantifying viable bacteria. **BioTechniques**, Future Science Ltd, v. 23, n. 4, p. 648–650, out. 1997. Disponível em: <https://doi.org/10.2144/97234bm22>. Citado na página 60.

131 HOSHYAR, N. et al. The effect of nanoparticle size on in vivo pharmacokinetics and cellular interaction. **Nanomedicine**, Future Medicine Ltd, v. 11, n. 6, p. 673–692, mar. 2016. Disponível em: <https://doi.org/10.2217/nnm.16.5>. Citado na página 61.

132 ZHANG, Y. et al. Cytotoxicity of organic surface coating agents used for nanoparticles synthesis and stability. **Toxicology in Vitro**, Elsevier BV, v. 29, n. 4, p. 762–768, jun. 2015. ISSN 0887-2333. Disponível em: <http://dx.doi.org/10.1016/j.tiv.2015.01.017>. Citado na página 63.

133 SCHULZ, F. et al. Effective PEGylation of gold nanorods. **Nanoscale**, Royal Society of Chemistry (RSC), v. 8, n. 13, p. 7296–7308, 2016. Disponível em: <https://doi.org/10.1039/c6nr00607h>. Citado na página 63.

134 HANNON, G. et al. The effects of localized heat on the hallmarks of cancer. **Advanced Therapeutics**, Wiley, v. 4, n. 7, maio 2021. Disponível em: <https://doi.org/10.1002/adtp.202000267>. Citado na página 64.

135 LARSSON, P. et al. Optimization of cell viability assays to improve replicability and reproducibility of cancer drug sensitivity screens. **Scientific Reports**, Springer Science and Business Media LLC, v. 10, n. 1, abr. 2020. ISSN 2045-2322. Disponível em: <http://dx.doi.org/10.1038/s41598-020-62848-5>. Citado na página 66.

136 American National Standard. **ANSI Z136.1- 2014 for Safe Use of Lasers**. [S.l.]: Laser Institute of America, 2014. Citado na página 66.

137 PUCCI, B.; KASTEN, M.; GIORDANO, A. Cell cycle and apoptosis. **Neoplasia**, Elsevier BV, v. 2, n. 4, p. 291–299, jul. 2000. ISSN 1476-5586. Disponível em: <http://dx.doi.org/10.1038/sj.neo.7900101>. Citado na página 68.

138 COLEMAN, W. B.; RUBINAS, T. C. Neoplasia. In: ____. **Essential Concepts in Molecular Pathology**. Elsevier, 2010. p. 45–61. ISBN 9780123744180. Disponível em: <http://dx.doi.org/10.1016/B978-0-12-374418-0.00004-9>. Citado na página 69.

139 NCI Dictionary of Cancer Terms — cancer.gov. 2011. <https://www.cancer.gov/publications/dictionaries/cancer-terms/def/infiltrating-cancer>. [Accessed 06-06-2024]. Citado na página 69.

140 SAMBRI, A. et al. Margin assessment in soft tissue sarcomas: Review of the literature. **Cancers**, MDPI AG, v. 13, n. 7, p. 1687, abr. 2021. ISSN 2072-6694. Disponível em: <http://dx.doi.org/10.3390/cancers13071687>. Citado na página 69.

141 MELAMED, J. R.; EDELSTEIN, R. S.; DAY, E. S. Elucidating the fundamental mechanisms of cell death triggered by photothermal therapy. **ACS Nano**, American Chemical Society (ACS), v. 9, n. 1, p. 6–11, jan. 2015. ISSN 1936-086X. Disponível em: <http://dx.doi.org/10.1021/acsnano.5b00021>. Citado na página 69.

142 RYCHLY, J. et al. Dna cytometric and histologic findings in mouse tumors (bp and s 180) with different response to treatment with tumor necrosis factor. **Acta Oncologica**, Informa UK Limited, v. 29, n. 1, p. 47–51, jan. 1990. ISSN 1651-226X. Disponível em: <http://dx.doi.org/10.3109/02841869009089991>. Citado na página 69.

143 SANTOS, S. A. et al. Antitumor profile of combined matricaria recutita flower extract and 5-fluorouracil chemotherapy in sarcoma 180 in vivo model. **Toxics**, MDPI AG, v. 11, n. 4, p. 375, abr. 2023. ISSN 2305-6304. Disponível em: <http://dx.doi.org/10.3390/toxics11040375>. Citado na página 69.

144 HUSSAIN, H. et al. Determination of cell viability using acridine orange/propidium iodide dual-spectrofluorometry assay. **Cogent Food & Agriculture**, Informa UK Limited, v. 5, n. 1, p. 1582398, jan. 2019. ISSN 2331-1932. Disponível em: <http://dx.doi.org/10.1080/23311932.2019.1582398>. Citado na página 70.

145 REN, Y. et al. Thermal dosage investigation for optimal temperature distribution in gold nanoparticle enhanced photothermal therapy. **International Journal of Heat and Mass Transfer**, Elsevier BV, v. 106, p. 212–221, mar. 2017. ISSN 0017-9310. Disponível em: <http://dx.doi.org/10.1016/j.ijheatmasstransfer.2016.10.067>. Citado na página 70.

146 DENTON, M. L. et al. Effect of ambient temperature and intracellular pigmentation on photothermal damage rate kinetics. **Journal of Biomedical Optics**, SPIE-Intl Soc Optical Eng, v. 24, n. 06, p. 1, jun. 2019. ISSN 1083-3668. Disponível em: <http://dx.doi.org/10.1117/1.JBO.24.6.065002>. Citado na página 70.

147 SIEGEL, A. L.; BAKER, G. A. Bespoke nanostars: synthetic strategies, tactics, and uses of tailored branched gold nanoparticles. **Nanoscale Advances**, Royal Society of Chemistry (RSC), v. 3, n. 14, p. 3980–4004, 2021. ISSN 2516-0230. Disponível em: <http://dx.doi.org/10.1039/d0na01057j>. Citado 2 vezes nas páginas 71 and 106.

148 SIM, J. Y. et al. In vivo microscopic photoacoustic spectroscopy for non-invasive glucose monitoring invulnerable to skin secretion products. **Scientific Reports**, Springer Science and Business Media LLC, v. 8, n. 1, jan. 2018. ISSN 2045-2322. Disponível em: <http://dx.doi.org/10.1038/s41598-018-19340-y>. Citado na página 72.

149 WANG, P. et al. Mapping lipid and collagen by multispectral photoacoustic imaging of chemical bond vibration. **Journal of Biomedical Optics**, SPIE-Intl Soc Optical Eng, v. 17, n. 9, p. 0960101, set. 2012. ISSN 1083-3668. Disponível em: <http://dx.doi.org/10.1117/1.JBO.17.9.096010>. Citado na página 72.

150 REGENSBURGER, A. P. et al. Detection of collagens by multispectral optoacoustic tomography as an imaging biomarker for duchenne muscular dystrophy. **Nature Medicine**, Springer Science and Business Media LLC, v. 25, n. 12, p. 1905–1915, dez. 2019. ISSN 1546-170X. Disponível em: <http://dx.doi.org/10.1038/s41591-019-0669-y>. Citado na página 72.

151 PAULUS, L.-P. et al. Multispectral optoacoustic tomography of the human intestine – temporal precision and the influence of postprandial gastrointestinal blood flow. **Photoacoustics**, Elsevier BV, v. 30, p. 100457, abr. 2023. ISSN 2213-5979. Disponível em: <http://dx.doi.org/10.1016/j.pacs.2023.100457>. Citado na página 72.

152 MARI, J. M. et al. Interventional multispectral photoacoustic imaging with a clinical ultrasound probe for discriminating nerves and tendons: anex vivopilot study. **Journal of Biomedical Optics**, SPIE-Intl Soc Optical Eng, v. 20, n. 11, p. 110503, nov. 2015. ISSN 1083-3668. Disponível em: <http://dx.doi.org/10.1117/1.JBO.20.11.110503>. Citado na página 72.

153 MATSUMOTO, Y. et al. Label-free photoacoustic imaging of human palmar vessels: a structural morphological analysis. **Scientific Reports**, Springer Science and Business Media LLC, v. 8, n. 1, jan. 2018. ISSN 2045-2322. Disponível em: <http://dx.doi.org/10.1038/s41598-018-19161-z>. Citado na página 72.

154 NA, S. et al. Massively parallel functional photoacoustic computed tomography of the human brain. **Nature Biomedical Engineering**, Springer Science and Business Media LLC, v. 6, n. 5, p. 584–592, maio 2021. ISSN 2157-846X. Disponível em: <http://dx.doi.org/10.1038/s41551-021-00735-8>. Citado na página 72.

155 LIU, Y.-H.; XU, Y.; THAKOR, N. Photoacoustic imaging tools for neurological applications. In: ____. **Handbook of Neuroengineering**. Springer Singapore, 2022. p. 1–47. ISBN 9789811528484. Disponível em: <http://dx.doi.org/10.1007/978-981-15-2848-4_82-1>. Citado na página 72.

156 LIN, L. et al. Single-breath-hold photoacoustic computed tomography of the breast. **Nature Communications**, Springer Science and Business Media LLC, v. 9, n. 1, jun. 2018. ISSN 2041-1723. Disponível em: <http://dx.doi.org/10.1038/s41467-018-04576-z>. Citado na página 72.

157 HESTER, S. C. et al. Role of ultrasound and photoacoustic imaging in photodynamic therapy for cancer. **Photochemistry and Photobiology**, Wiley, v. 96, n. 2, p. 260–279, mar. 2020. ISSN 1751-1097. Disponível em: <http://dx.doi.org/10.1111/php.13217>. Citado na página 73.

158 MALLIDI, S. et al. Prediction of tumor recurrence and therapy monitoring using ultrasound-guided photoacoustic imaging. **Theranostics**, Ivyspring International Publisher, v. 5, n. 3, p. 289–301, 2015. ISSN 1838-7640. Disponível em: <http://dx.doi.org/10.7150/thno.10155>. Citado na página 73.

159 LARINA, I. V.; LARIN, K. V.; ESENALIEV, R. O. Real-time optoacoustic monitoring of temperature in tissues. **Journal of Physics D: Applied Physics**, IOP Publishing, v. 38, n. 15, p. 2633–2639, jul. 2005. ISSN 1361-6463. Disponível em: <http://dx.doi.org/10.1088/0022-3727/38/15/015>. Citado na página 73.

160 SHI, J. et al. High-resolution, high-contrast mid-infrared imaging of fresh biological samples with ultraviolet-localized photoacoustic microscopy. **Nature Photonics**, Springer Science and Business Media LLC, v. 13, n. 9, p. 609–615, maio 2019. ISSN 1749-4893. Disponível em: <http://dx.doi.org/10.1038/s41566-019-0441-3>. Citado na página 73.

161 WANG, Y. et al. Mid-infrared photoacoustic gas monitoring driven by a gas-filled hollow-core fiber laser. **Scientific Reports**, Springer Science and Business Media LLC, v. 11, n. 1, fev. 2021. ISSN 2045-2322. Disponível em: <http://dx.doi.org/10.1038/s41598-021-83041-2>. Citado na página 73.

162 PLEITEZ, M. A. et al. Label-free metabolic imaging by mid-infrared optoacoustic microscopy in living cells. **Nature Biotechnology**, Springer Science and Business Media LLC, v. 38, n. 3, p. 293–296, dez. 2019. ISSN 1546-1696. Disponível em: <http://dx.doi.org/10.1038/s41587-019-0359-9>. Citado na página 73.

163 ATTIA, A. B. E. et al. A review of clinical photoacoustic imaging: Current and future trends. **Photoacoustics**, Elsevier BV, v. 16, p. 100144, dez. 2019. ISSN 2213-5979. Disponível em: <http://dx.doi.org/10.1016/j.pacs.2019.100144>. Citado na página 73.

164 BISWAS, D.; ROY, S.; VASUDEVAN, S. Biomedical application of photoacoustics: A plethora of opportunities. **Micromachines**, MDPI AG, v. 13, n. 11, p. 1900, nov. 2022. ISSN 2072-666X. Disponível em: <http://dx.doi.org/10.3390/mi13111900>. Citado na página 73.

165 LEE, H. et al. A review on the roles of photoacoustic imaging for conventional and novel clinical diagnostic applications. **Photonics**, MDPI AG, v. 10, n. 8, p. 904, ago. 2023. ISSN 2304-6732. Disponível em: <http://dx.doi.org/10.3390/photonics10080904>. Citado na página 73.

166 JOHN, S. et al. Niche preclinical and clinical applications of photoacoustic imaging with endogenous contrast. **Photoacoustics**, Elsevier BV, v. 32, p. 100533, ago. 2023. ISSN 2213-5979. Disponível em: <http://dx.doi.org/10.1016/j.pacs.2023.100533>. Citado na página 73.

167 PARK, B. et al. Functional photoacoustic imaging: from nano- and micro- to macro-scale. **Nano Convergence**, Springer Science and Business Media LLC, v. 10, n. 1, jun. 2023. ISSN 2196-5404. Disponível em: <http://dx.doi.org/10.1186/s40580-023-00377-3>. Citado na página 73.

168 ZHOU, Y.; YAO, J.; WANG, L. V. Tutorial on photoacoustic tomography. **Journal of Biomedical Optics**, SPIE-Intl Soc Optical Eng, v. 21, n. 6, p. 061007, abr. 2016. ISSN 1083-3668. Disponível em: <http://dx.doi.org/10.1117/1.JBO.21.6.061007>. Citado na página 73.

169 UPPUTURI, P. K.; PRAMANIK, M. Recent advances toward preclinical and clinical translation of photoacoustic tomography: a review. **Journal of Biomedical Optics**, SPIE-Intl Soc Optical Eng, v. 22, n. 4, p. 041006, nov. 2016. ISSN 1083-3668. Disponível em: <http://dx.doi.org/10.1117/1.JBO.22.4.041006>. Citado na página 73.

170 PALTAUF, G.; NUSTER, R.; FRENZ, M. Progress in biomedical photoacoustic imaging instrumentation toward clinical application. **Journal of Applied Physics**, AIP Publishing, v. 128, n. 18, p. 180907, nov. 2020. Disponível em: <https://doi.org/10.1063/5.0028190>. Citado na página 73.

171 MANOHAR, S.; RAZANSKY, D. Photoacoustics: a historical review. **Advances in Optics and Photonics**, The Optical Society, v. 8, n. 4, p. 586, out. 2016. ISSN 1943-8206. Disponível em: <http://dx.doi.org/10.1364/AOP.8.000586>. Citado na página 73.

172 ZHU, Y. et al. Light emitting diodes based photoacoustic imaging and potential clinical applications. **Sci. Rep.**, Springer Science and Business Media LLC, v. 8, n. 1, jun. 2018. Citado na página 73.

173 ZHU, Y. et al. Towards clinical translation of led-based photoacoustic imaging: A review. **Sensors**, MDPI AG, v. 20, n. 9, p. 2484, abr. 2020. ISSN 1424-8220. Disponível em: <http://dx.doi.org/10.3390/s20092484>. Citado na página 73.

174 SHARMA, A. et al. Photoacoustic imaging depth comparison at 532-, 800-, and 1064-nm wavelengths: Monte carlo simulation and experimental validation. **Journal of Biomedical Optics**, SPIE-Intl Soc Optical Eng, v. 24, n. 12, p. 1, ago. 2019. Disponível em: <https://doi.org/10.1117/1.jbo.24.12.121904>. Citado 2 vezes nas páginas 73 and 74.

175 HANNAH, A. et al. Indocyanine green-loaded photoacoustic nanodroplets: Dual contrast nanoconstructs for enhanced photoacoustic and ultrasound imaging. **ACS Nano**, American Chemical Society (ACS), v. 8, n. 1, p. 250–259, December 2013. ISSN 1936-086X. Disponível em: <http://dx.doi.org/10.1021/nn403527r>. Citado na página 74.

176 XAVIERSELVAN, M. et al. Photoacoustic nanodroplets for oxygen enhanced photodynamic therapy of cancer. **Photoacoustics**, Elsevier BV, v. 25, p. 100306, March 2022. ISSN 2213-5979. Disponível em: <http://dx.doi.org/10.1016/j.pacs.2021.100306>. Citado na página 74.

177 KIM, J. et al. Gold nanoparticles conjugated with dna aptamer for photoacoustic detection of human matrix metalloproteinase-9. **Photoacoustics**, Elsevier BV, v. 25, p. 100307, March 2022. ISSN 2213-5979. Disponível em: <http://dx.doi.org/10.1016/j.pacs.2021.100307>. Citado na página 74.

178 ALCHERA, E. et al. Early diagnosis of bladder cancer by photoacoustic imaging of tumor-targeted gold nanorods. **Photoacoustics**, Elsevier BV, v. 28, p. 100400, December 2022. ISSN 2213-5979. Disponível em: <http://dx.doi.org/10.1016/j.pacs.2022.100400>. Citado na página 74.

179 ZHENG, N. et al. Photoacoustic carbon nanotubes embedded silk scaffolds for neural stimulation and regeneration. **ACS Nano**, American Chemical Society (ACS), v. 16, n. 2, p. 2292–2305, January 2022. ISSN 1936-086X. Disponível em: <http://dx.doi.org/10.1021/acsnano.1c08491>. Citado na página 74.

180 HAN, S. et al. Contrast agents for photoacoustic imaging: A review focusing on the wavelength range. **Biosensors**, MDPI AG, v. 12, n. 8, p. 594, August 2022. ISSN 2079-6374. Disponível em: <http://dx.doi.org/10.3390/bios12080594>. Citado na página 74.

181 BOUTOPOULOS, C.; BERGERON, E.; MEUNIER, M. Cell perforation mediated by plasmonic bubbles generated by a single near infrared femtosecond laser pulse. **Journal of Biophotonics**, Wiley, v. 9, n. 1-2, p. 26–31, jul. 2015. Disponível em: <https://doi.org/10.1002/jbio.201500135>. Citado na página 74.

182 INZUNZA-IBARRA, M. A. et al. Enhanced visibility through microbubble-induced photoacoustic fluctuation imaging. **JASA Express Letters**, Acoustical Society of America (ASA), v. 2, n. 1, January 2022. ISSN 2691-1191. Disponível em: <http://dx.doi.org/10.1121/10.0009129>. Citado na página 74.

183 MANTRI, Y.; JOKERST, J. V. Engineering plasmonic nanoparticles for enhanced photoacoustic imaging. **ACS Nano**, American Chemical Society (ACS), v. 14, n. 8, p. 9408–9422, ago. 2020. Disponível em: <https://doi.org/10.1021/acsnano.0c05215>. Citado na página 74.

184 GANDOLFI, M.; BANFI, F.; GLORIEUX, C. Optical wavelength dependence of photoacoustic signal of gold nanofluid. **Photoacoustics**, Elsevier BV, v. 20, p. 100199, December 2020. ISSN 2213-5979. Disponível em: <http://dx.doi.org/10.1016/j.pacs.2020.100199>. Citado na página 74.

185 SUN, J.-P. et al. Dependence of the nonlinear photoacoustic response of gold nanoparticles on the heat-transfer process. **The Journal of Physical Chemistry C**, American Chemical Society (ACS), v. 126, n. 7, p. 3489–3501, January 2022. ISSN 1932-7455. Disponível em: <http://dx.doi.org/10.1021/acs.jpcc.1c09245>. Citado na página 74.

186 SUN, J.-P. et al. Photoacoustic response optimization of gold nanorods in the near-infrared region. **Results in Physics**, Elsevier BV, v. 34, p. 105209, March 2022. ISSN 2211-3797. Disponível em: <http://dx.doi.org/10.1016/j.rinp.2022.105209>. Citado na página 74.

187 LIU, X. et al. Strong size-dependent photoacoustic effect on gold nanoparticles: a sensitive tool for aggregation-based colorimetric protein detection. **Anal. Methods**, Royal Society of Chemistry (RSC), v. 4, n. 1, p. 309–311, 2012. ISSN 1759-9679. Disponível em: <http://dx.doi.org/10.1039/c1ay05497j>. Citado na página 74.

188 EL-BROLOSSY, T. A. et al. Shape and size dependence of the surface plasmon resonance of gold nanoparticles studied by photoacoustic technique. **The European Physical Journal Special Topics**, Springer Science and Business Media LLC, v. 153, n. 1, p. 361–364, January 2008. ISSN 1951-6401. Disponível em: <http://dx.doi.org/10.1140/epjst/e2008-00462-0>. Citado na página 74.

189 PANG, G. A. et al. Theoretical and experimental study of photoacoustic excitation of silica-coated gold nanospheres in water. **The Journal of Physical Chemistry C**, American Chemical Society (ACS), v. 124, n. 1, p. 1088–1098, December 2019. ISSN 1932-7455. Disponível em: <http://dx.doi.org/10.1021/acs.jpcc.9b09040>. Citado na página 74.

190 DAS, A. et al. Plasmonically enhanced two-photon absorption induced photoacoustic microscopy with laser-synthesized tin nanoparticles. **Applied Physics Letters**, AIP Publishing, v. 121, n. 8, ago. 2022. ISSN 1077-3118. Disponível em: <http://dx.doi.org/10.1063/5.0101658>. Citado na página 75.

191 CHANEY, R. C. et al. Ultrasonic method for evaluation of annular seals for wells and instrument holes. **Geotech. Test. J.**, ASTM International, v. 20, n. 1, p. 17, 1997. Citado na página 75.

192 BRONGERSMA, M. L.; HALAS, N. J.; NORDLANDER, P. Plasmon-induced hot carrier science and technology. **Nature Nanotechnology**, Springer Science and Business Media LLC, v. 10, n. 1, p. 25–34, jan. 2015. Disponível em: <https://doi.org/10.1038/nnano.2014.311>. Citado na página 76.

193 BURGHOLZER, P. et al. Resolution limits in photoacoustic imaging caused by acoustic attenuation. **Journal of Imaging**, MDPI AG, v. 5, n. 1, p. 13, jan. 2019. ISSN 2313-433X. Disponível em: <http://dx.doi.org/10.3390/jimaging5010013>. Citado na página 76.

194 YAO, J.; WANG, L. V. Photoacoustic microscopy. **Laser Photon. Rev.**, Wiley, v. 7, n. 5, p. 758–778, set. 2013. Citado na página 77.

195 HAI, P. et al. Near-infrared optical-resolution photoacoustic microscopy. **Opt. Lett.**, The Optical Society, v. 39, n. 17, p. 5192–5195, set. 2014. Citado na página 77.

196 MAKI, K.; SAGARA, J.; KAWAI, A. A cationic detergent, cetyltrimethylammonium bromide (CTAB), selectively dissociates the intermediate filament of the fibroblast. **Biochem. Biophys. Res. Commun.**, Elsevier BV, v. 175, n. 3, p. 768–774, mar. 1991. Citado na página 78.

197 CAI, H. et al. Enhanced hydrophilic and electrophilic properties of polyvinyl chloride (PVC) biofilm carrier. **Polymers (Basel)**, MDPI AG, v. 12, n. 6, p. 1240, maio 2020. Citado na página 78.

198 AGGARWAL, S.; IKRAM, S. Surface modification of polysaccharide nanocrystals. In: **Innovation in Nano-Polysaccharides for Eco-sustainability**. [S.l.]: Elsevier, 2022. p. 133–161. Citado na página 78.

199 CAVIGLI, L. et al. Impact of kapitza resistance on the stability and efficiency of photoacoustic conversion from gold nanorods. **J. Colloid Interface Sci.**, Elsevier BV, v. 578, p. 358–365, out. 2020. Citado na página 79.

200 MANTRI, Y. et al. Photoacoustic enhancement of ferricyanide-treated silver chalcogenide-coated gold nanorods. **J. Phys. Chem. C Nanomater. Interfaces**, American Chemical Society (ACS), v. 126, n. 17, p. 7605–7614, maio 2022. Citado na página 79.

201 YU, L. et al. High-contrast photoacoustic imaging through scattering media using correlation detection of adaptive time window. **Sci. Rep.**, Springer Science and Business Media LLC, v. 9, n. 1, p. 17262, nov. 2019. Citado na página 80.

202 GONZÁLEZ-RUBIO, G.; GUERRERO-MARTÍNEZ, A.; LIZ-MARZÁN, L. M. Reshaping, fragmentation, and assembly of gold nanoparticles assisted by pulse lasers. **Acc. Chem. Res.**, American Chemical Society (ACS), v. 49, n. 4, p. 678–686, abr. 2016. Citado na página 81.

203 KAHAN, A. **EIA projects nearly 50% increase in world energy usage by 2050, led by growth in Asia - U.S. Energy Information Administration (EIA) — eia.gov**. 2019. <https://www.eia.gov/todayinenergy/detail.php?id=41433>. [Accessed 10-06-2024]. Citado na página 83.

204 RITCHIE, H.; ROSADO, P.; ROSER, M. Energy production and consumption. **Our World in Data**, 2020. Https://ourworldindata.org/energy-production-consumption. Citado na página 83.

205 RITCHIE, H.; ROSADO, P. Energy mix. **Our World in Data**, 2020. Https://ourworldindata.org/energy-mix. Citado na página 83.

206 ROCKSTRöM, J. et al. Safe and just earth system boundaries. **Nature**, Springer Science and Business Media LLC, v. 619, n. 7968, p. 102–111, maio 2023. ISSN 1476-4687. Disponível em: <http://dx.doi.org/10.1038/s41586-023-06083-8>. Citado na página 83.

207 CARDOZO, O. et al. Zinc oxide nanodiffusers to enhance p3ht:pcbm organic solar cells performance. **Journal of Materials Science: Materials in Electronics**, Springer Science and Business Media LLC, v. 33, n. 6, p. 3225–3236, jan. 2022. ISSN 1573-482X. Disponível em: <http://dx.doi.org/10.1007/s10854-021-07524-8>. Citado na página 84.

208 KABEEL, A. et al. Experimental study on tubular solar still using graphene oxide nano particles in phase change material (npcm's) for fresh water production. **Journal of Energy Storage**, Elsevier BV, v. 28, p. 101204, abr. 2020. ISSN 2352-152X. Disponível em: <http://dx.doi.org/10.1016/j.est.2020.101204>. Citado na página 84.

209 JIN, H. et al. Steam generation in a nanoparticle-based solar receiver. **Nano Energy**, Elsevier BV, v. 28, p. 397–406, out. 2016. ISSN 2211-2855. Disponível em: <http://dx.doi.org/10.1016/j.nanoen.2016.08.011>. Citado na página 84.

210 EVANGELISTI, L.; VOLLARO, R. D. L.; ASDRUBALI, F. Latest advances on solar thermal collectors: A comprehensive review. **Renewable and Sustainable Energy Reviews**, Elsevier BV, v. 114, p. 109318, out. 2019. ISSN 1364-0321. Disponível em: <http://dx.doi.org/10.1016/j.rser.2019.109318>. Citado na página 84.

211 SAINZ-MAñAS, M. et al. Direct absorption nanofluid-based solar collectors for low and medium temperatures. a review. **Energy**, Elsevier BV, v. 260, p. 124916, dez. 2022. ISSN 0360-5442. Disponível em: <http://dx.doi.org/10.1016/j.energy.2022.124916>. Citado na página 84.

212 SEO, J. et al. Tailoring the spectral absorption coefficient of a blended plasmonic nanofluid using a customized genetic algorithm. **Scientific Reports**, Springer Science and Business Media LLC, v. 10, n. 1, jun. 2020. ISSN 2045-2322. Disponível em: <http://dx.doi.org/10.1038/s41598-020-65811-6>. Citado na página 85.

213 YANG, P. et al. Recent developments in polydopamine fluorescent nanomaterials. **Materials Horizons**, Royal Society of Chemistry (RSC), v. 7, n. 3, p. 746–761, 2020. ISSN 2051-6355. Disponível em: <http://dx.doi.org/10.1039/C9MH01197H>. Citado na página 85.

214 CARMIGNANI, A. et al. In vitro and ex vivo investigation of the effects of polydopamine nanoparticle size on their antioxidant and photothermal properties: Implications for biomedical applications. **ACS Applied Nano Materials**, American Chemical Society (ACS), v. 5, n. 1, p. 1702–1713, jan. 2022. ISSN 2574-0970. Disponível em: <http://dx.doi.org/10.1021/acsanm.1c04536>. Citado na página 85.

215 ACTER, S. et al. Polydopamine nanomaterials for overcoming current challenges in cancer treatment. **Nanomaterials**, MDPI AG, v. 13, n. 10, p. 1656, maio 2023. ISSN 2079-4991. Disponível em: <http://dx.doi.org/10.3390/nano13101656>. Citado na página 85.

216 SOTOMA, S. et al. In situ measurements of intracellular thermal conductivity using heater-thermometer hybrid diamond nanosensors. **Science Advances**, American Association for the Advancement of Science (AAAS), v. 7, n. 3, jan. 2021. ISSN 2375-2548. Disponível em: <http://dx.doi.org/10.1126/sciadv.abd7888>. Citado 2 vezes nas páginas 85 and 93.

217 HAUSER, D. et al. Polydopamine nanoparticle doped nanofluid for solar thermal energy collector efficiency increase. **Advanced Sustainable Systems**, Wiley, v. 4, n. 1, dez. 2019. ISSN 2366-7486. Disponível em: <http://dx.doi.org/10.1002/adsu.201900101>. Citado 2 vezes nas páginas 85 and 101.

218 WANG, Q. et al. Recyclable fe3o4@polydopamine (pda) nanofluids for highly efficient solar evaporation. **Green Energy & Environment**, Elsevier BV, v. 7, n. 1, p. 35–42, fev. 2022. ISSN 2468-0257. Disponível em: <http://dx.doi.org/10.1016/j.gee.2020.07.020>. Citado na página 85.

219 ZOU, Y. et al. Regulating the absorption spectrum of polydopamine. **Science Advances**, American Association for the Advancement of Science (AAAS), v. 6, n. 36, set. 2020. ISSN 2375-2548. Disponível em: <http://dx.doi.org/10.1126/sciadv.abb4696>. Citado 3 vezes nas páginas 85, 92, and 93.

220 NIETO, C. et al. Size matters in the cytotoxicity of polydopamine nanoparticles in different types of tumors. **Cancers**, MDPI AG, v. 11, n. 11, p. 1679, out. 2019. ISSN 2072-6694. Disponível em: <http://dx.doi.org/10.3390/cancers11111679>. Citado na página 85.

221 ACTER, S. et al. Bowl-shaped mesoporous polydopamine nanoparticles for size-dependent endocytosis into hela cells. **ACS Applied Nano Materials**, American Chemical Society (ACS), v. 4, n. 9, p. 9536–9546, ago. 2021. ISSN 2574-0970. Disponível em: <http://dx.doi.org/10.1021/acsanm.1c01897>. Citado na página 85.

222 MENICHETTI, A.; MORDINI, D.; MONTALTI, M. Polydopamine nanosystems in drug delivery: Effect of size, morphology, and surface charge. **Nanomaterials (Basel)**, MDPI AG, v. 14, n. 3, p. 303, fev. 2024. Citado na página 85.

223 ZHANG, P. et al. Polydopamine nanoparticles with different sizes for NIR-promoted gene delivery and synergistic photothermal therapy. **Colloids Surf. B Biointerfaces**, Elsevier BV, v. 208, n. 112125, p. 112125, dez. 2021. Citado na página 85.

224 DROTNING, W. D. Optical properties of solar-absorbing oxide particles suspended in a molten salt heat transfer fluid. **Solar Energy**, Elsevier BV, v. 20, n. 4, p. 313–319, 1978. ISSN 0038-092X. Disponível em: <http://dx.doi.org/10.1016/0038-092X(78)90123-8>. Citado na página 86.

225 ZHOU, P.-b. Finite difference method. In: ____. **Numerical Analysis of Electromagnetic Fields**. Springer Berlin Heidelberg, 1993. p. 63–94. ISBN 9783642503191. Disponível em: <http://dx.doi.org/10.1007/978-3-642-50319-1_3>. Citado 2 vezes nas páginas 88 and 91.

226 BHALLA, V.; KHULLAR, V.; TYAGI, H. Investigation of factors influencing the performance of nanofluid-based direct absorption solar collector using taguchi method. **Journal of Thermal Analysis and Calorimetry**, Springer Science and Business Media LLC, v. 135, n. 2, p. 1493–1505, set. 2018. ISSN 1588-2926. Disponível em: <http://dx.doi.org/10.1007/s10973-018-7721-x>. Citado na página 88.

227 MAZUMDER, S. The finite difference method. In: ____. **Numerical Methods for Partial Differential Equations**. Elsevier, 2016. p. 51–101. ISBN 9780128498941. Disponível em: <http://dx.doi.org/10.1016/B978-0-12-849894-1.00002-0>. Citado 2 vezes nas páginas 89 and 91.

228 DUAN, H. et al. Effect of plasmonic nanoshell-based nanofluid on efficiency of direct solar thermal collector. **Applied Thermal Engineering**, Elsevier BV, v. 133, p. 188–193, mar. 2018. ISSN 1359-4311. Disponível em: <http://dx.doi.org/10.1016/j.applthermaleng.2018.01.042>. Citado na página 91.

229 ZHANG, H. et al. Photothermal conversion characteristics of gold nanoparticle dispersions. **Solar Energy**, Elsevier BV, v. 100, p. 141–147, fev. 2014. ISSN 0038-092X. Disponível em: <http://dx.doi.org/10.1016/j.solener.2013.12.004>. Citado na página 97.

230 YANG, W. et al. Nanoparticles of polydopamine for improving mechanical and flame-retardant properties of an epoxy resin. **Composites Part B: Engineering**, Elsevier BV, v. 186, p. 107828, abr. 2020. ISSN 1359-8368. Disponível em: <http://dx.doi.org/10.1016/j.compositesb.2020.107828>. Citado na página 98.

231 CAPELOTO, O. A. et al. Induction and detection of pressure waves by pulsed thermal lens technique in water–ethanol mixtures. **Applied Optics**, Optica Publishing Group, v. 60, n. 13, p. 4029, abr. 2021. ISSN 2155-3165. Disponível em: <http://dx.doi.org/10.1364/AO.420275>. Citado na página 105.

232 CHOI, H. S. et al. Renal clearance of quantum dots. **Nature Biotechnology**, Springer Science and Business Media LLC, v. 25, n. 10, p. 1165–1170, set. 2007. Disponível em: <https://doi.org/10.1038/nbt1340>. Citado na página 106.

233 LONGMIRE, M.; CHOYKE, P. L.; KOBAYASHI, H. Clearance properties of nano-sized particles and molecules as imaging agents: considerations and caveats. **Nanomedicine**, Future Medicine Ltd, v. 3, n. 5, p. 703–717, out. 2008. Disponível em: <https://doi.org/10.2217/17435889.3.5.703>. Citado na página 106.

234 LIU, Y. et al. Photothermal therapy and photoacoustic imaging via nanotheranostics in fighting cancer. **Chemical Society Reviews**, Royal Society of Chemistry (RSC), v. 48, n. 7, p. 2053–2108, 2019. ISSN 1460-4744. Disponível em: <http://dx.doi.org/10.1039/c8cs00618k>. Citado na página 106.

235 FONTANA, J. et al. Rise of the charge transfer plasmon: Programmable concatenation of conductively linked gold nanorod dimers. **ACS Photonics**, American Chemical Society (ACS), v. 3, n. 5, p. 904–911, maio 2016. Disponível em: <https://doi.org/10.1021/acsphotonics.6b00184>. Citado na página 106.

236 YOON, J. H. et al. Surface plasmon coupling in dimers of gold nanoparticles: Experiment and theory for ideal (spherical) and nonideal (faceted) building blocks. **ACS Photonics**, American Chemical Society (ACS), v. 6, n. 3, p. 642–648, fev. 2019. ISSN 2330-4022. Disponível em: <http://dx.doi.org/10.1021/acsphotonics.8b01424>. Citado na página 106.

237 EL-BAHRAWI, M. et al. Birefringence of muscovite mica. **Optics & Laser Technology**, Elsevier BV, v. 30, n. 6–7, p. 411–415, set. 1998. ISSN 0030-3992. Disponível em: <http://dx.doi.org/10.1016/s0030-3992(98)00074-7>. Citado na página 145.

238 LIU, E. et al. Ultrasound findings of monosodium urate aggregates in patients with gout. **Gout, Urate, and Crystal Deposition Disease**, MDPI AG, v. 1, n. 2, p. 83–88, abr. 2023. ISSN 2813-4583. Disponível em: <http://dx.doi.org/10.3390/gucdd1020008>. Citado na página 146.

APPENDIX A – THERMOPLASMONICS LIBRARY

Thermoplasmonics is a library developed during the course of my graduate studies to aid theoretical investigations in the field of photothermal heating of plasmonic nanoparticles and provide a framework to standardize image/plot formatting and perform data processing. The libraby can be easily accessed, downloaded and used for free in <https://github.com/pedrosatulio/Thermoplasmonics>.

The library relies on Mie and Mie-Gans theories to calculate the optical cross sections of NPs (mostly plasmonic) and translate the results to thermal simulation environments for further photothermal conversion analysis. FoM [84] are extensively used for characterization, and collective temperature increase is also modeled.

Furthermore, a collection of refractive indexes for different optical materials was included, and their permittivities are compensated following the size dependent Drude model (Equation 2.3). While the computation of nanospheres and nanoshells use Mie theory (Equations 2.4–2.8), nanorods are modeled as prolate spheroids with optical cross sections determined by Rayleigh-Gans approximation (Equations 2.13–2.14) with polarizability correction using Modified Long Wavelength Approximation (MLWA) (Equation 2.17).

Moreover, the framework integrate optical calculations to a thermal module that uses FDM to simulate DASCs and extract temperature increase, as well as the device's thermodynamic performance.

This library was used extensively during the execution of this project. A set of curated tutorials were cataloged to facilitate the use of this tool: <https://github.com/pedrosatulio/Thermoplasmonics/blob/main/README.md>.

TUTORIALS

Simple optical cross-section calculation

The optical cross sections of a gold nanosphere of diameter 100 nm in water are calculated. Absorption, scattering, extinction and backscattering are shown. The norm of the electric and magnetic fields, as well as the heat source density are also depicted.
Link: <https://github.com/pedrosatulio/Thermoplasmonics/blob/main/Thermoplasmonics.md>

Parametric sweep #1: 1D sweep

Parametric sweep on gold nanospheres for increasing radius (from 5 to 100 nm) is illustrated. Absorption maxima for each size is stored and used to calculate the size dependent FoM. The obtained results are plotted.

Link: <https://github.com/pedrosatulio/Thermoplasmonics/blob/main/Parametric%20sweep.md>

Parametric sweep #2: colormaps

Multidimensional parametric sweep is introduced exploring LSPR tunability of nanorods. Gold nanorod length and diameter are swept and absorption cross section extracted. Plasmon peak wavelength and FoM colormaps are elaborated based length and diameter changes.
Link: <https://github.com/pedrosatulio/Thermoplasmonics/blob/main/Colormap.md>

Collective heating in cuvette

Here, a generic solution to the macroscopic transient heating of gold colloid in a cuvette suffering from convective heat losses (h) is shown. Three gold nanosphere sizes are modeled (5, 50 and 100 nm) maintaining the same total mass of NPs among calculations. Temperature increase in the steady-state is then compared with FoM.
Link: <https://github.com/pedrosatulio/Thermoplasmonics/blob/main/Thermal.md>

FDM for DASCs

DASCs are simulated using FMD. Thermo-optical and thermophysical properties of nanofluids are modeled, considering the basefluid and NP characteristics. The solar spectral irradiance is explored and a nanofluid containing 100 nm gold nanospheres is simulated for solar heating. Furthermore, spectral absorption is discussed from Beer attenuation analysis and solar weighted absorption coefficient evaluated. Moreover, all data are plotted and DASC performance exported.
Link: <https://github.com/pedrosatulio/Thermoplasmonics/blob/main/DASC.md>

FUTURE ADDITIONS

The library is incomplete in its current form. To further support thermoplasmonic investigations, a new set of features are planned to be introduced in future releases. Below, we highlight a non-exhaustive list of intended additions:

- Add support for spheroidal nanoshells;
- Model NP monodispersity: *include a distribution of NP sizes to mimic the spectral broadening seen in experimental data*;
- Add support for direct import of external files of nanofluid spectrum for solar simulation;
- Add DDA [52] support for NPs of arbitrary shape;
- Expand FDM implementation to include the thermal simulation of single NP and plasmonic metamolecules:

1. *Steady-state heat transfer*
2. *Transient heat transfer*
3. *Add support for different laser pulse regimes*

- Add support for photoacoustics.

APPENDIX B – FINITE ELEMENT METHOD SIMULATIONS

OVERVIEW OF FINITE ELEMENT METHOD

The Finite Element Method (FEM) is a numeric computational procedure applied for solving multiphysics systems described by differential equations under the influence of specific boundary value problems. The use FEM enables the analysis of physical phenomena with high accuracy, yielding results in good agreement with experimental data if a reasonable approach in modeling is performed, which leads to a substantial cost reduction in designing and engineering real solutions.

The applicability of the FEM method assumes that the problem is subjected to an integral law or differential equation, which enables the equations to be replaced, in all domains, by a finite summation of discretized sub-domains. Each sub-domain features a simple geometry in which the problem preserves continuity and differentiability. Equation B.1 describes the reconstitution of a discretized problem, while Equation B.2 shows the discretization of a domain *V* into sub-domains $\mathrm{V_i}$.

$$\int_V f dV = \sum_{i=1}^{n} \int_{Vi} f dV \ , \tag{B.1}$$

in which

$$V = \sum_{i=1}^{n} V_i \ . \tag{B.2}$$

Furthermore, f is approximated as a linear combination of a base of building orthogonal functions ($\mathrm{f_i} = \sum_{\mathrm{n}} \mathrm{f_n} \lambda_{\mathrm{n}}$). The discretized geometry form the mesh cells. In each mesh cell, the number of physical variables associated to the problem (that are infinitely many real variables) are replaced by a limited number of well behaved variables. The accuracy of the FEM is related to the mesh type associated to the model. Figure 37 shows a spherical region partitioned in many sub-domains to endure FEM computation. An increase in mesh number can lead to a refinement in accuracy, but processing times also increase. Moreover, the increase in mesh number won't necessarily lead to increased accuracy.

In problems where EM fields are involved, the FEM approximation is implemented in Maxwell Equations for electrodynamics. In order to be resolvable, a set of boundary conditions and material constitutive relations are needed. The COMSOL formulation of Maxwell equations is the same for both the Radio-Frequency - *Frequency Domain* module and the Waveoptics - *Wavelength Domain* module, based on the solution of the non-homogeneous wave equation:

Figure 37 – Sub-domains in a model undergoing FEM analysis. The blue shell depict the perfect matched layer (PML) of the model. The region is said to be meshed.

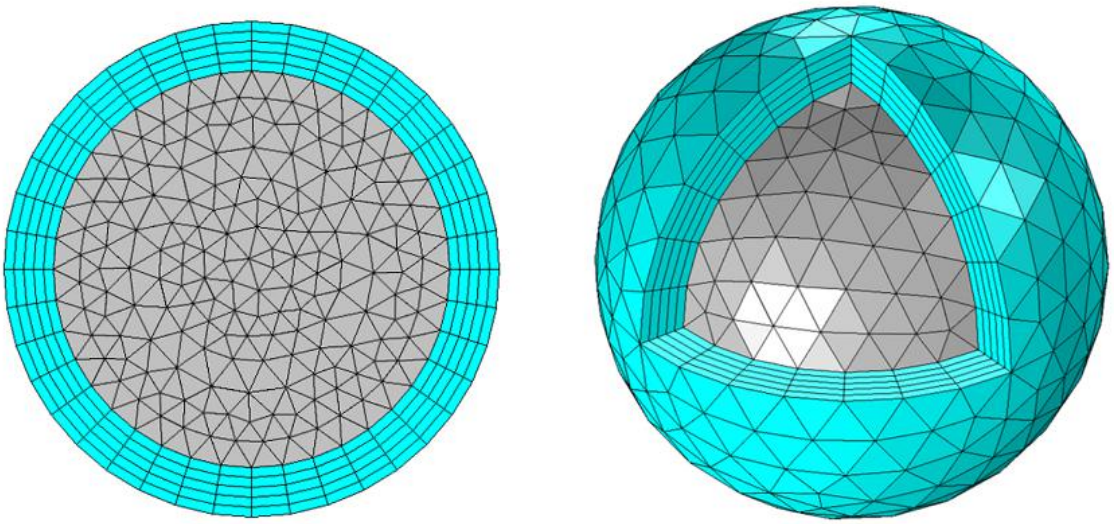

Source: adapted from COMSOL[53].

$$\vec{\nabla} \times \left[\mu_r^{-1}\left(\vec{\nabla} \times \vec{E}\right)\right] - \omega^2 \epsilon_0 \mu_0 \left(\epsilon_r - j\frac{\sigma}{\omega\epsilon_0}\right)\vec{E} = 0 \tag{B.3}$$

in which μ_0 and ϵ_0 are respectively the vacuum magnetic permeability and electric permittivity, and μ_r and ϵ_r designate, respectively, the relative permeability and relative permittivity of the material medium associated to the problem.

Similarly, in problems where transient conductive heat transfer is involved, Poisson's equation is implemented by FEM method. COMSOL formulation for a generic heat-transfer problem is given by equation B.4, where $\vec{u}$ is the fluid velocity and Q is the volumetric power density.

$$\rho C_p \frac{\partial T}{\partial t} + \rho C_p \, \vec{u} \cdot \nabla T + \nabla \cdot (-\kappa \nabla T) = Q \tag{B.4}$$

SIMULATION OF METALLIC NANOSTRUCTURES IN COMSOL MULTIPHYSICS

This tutorial describes the procedures performed to simulate gold nanoparticles using the Electromagnetic Waves model of COMSOL. Here, at the end of the simulation, the optical cross sections (scattering, absorption and extinction) of a gold nanorod will be obtained, as well as the Joule number and the Steady-state factor of a single nanorod. Furthermore, this tutorial can be employed as a basic framework for the simulation of nanoparticles of any other material or shape of interest. The specs of the workstation used in our simulations are 128 GB of RAM, 512 GB (SSD NVMe) + 1 TB (HD) of storage, Intel Core i9 7920X (12 cores @ 2.90 GHz).

After opening COMSOL, you will come across the New project window. In the window *New*, click on Model Wizard, and after that, select *3D* in the space dimension menu. It's necessary now to select the physical module that will be used to analyze the problem. In *Select Physics*, expand the drop-down bar *Radio Frequency*, and select the *Frequency Domain (emw)* option and click on *Add*. With such physics interface selected, click on *Study* and in the *Select Study* screen click on *Frequency Domain* and after that, click on *Done*. A new screen with many elements will show, as can be seen in Figure 38. Take the opportunity to save the project in a desired location.

Figure 38 – Screen after the project setup. This is the main project screen of COMSOL.

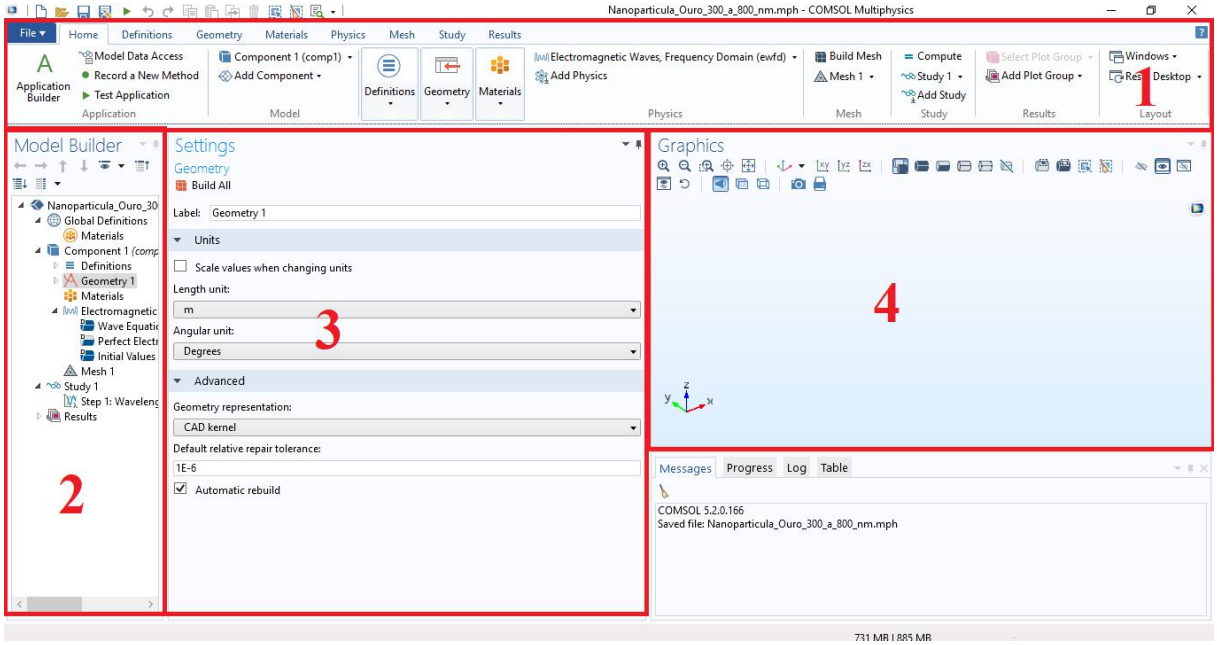

Source: belongs to the author.

In Figure 38, the main screen is divided into four parts. Section 1 is the *Toolbar*, and has, among its functions, the role of adding new and diverse elements to the project. Section 2 (*Model Builder*) is the menu that allows the user to navigate throughout the project. Here, it is also possible to perform some of the *Toolbar* functionalities. Section 3 (*Settings*) has all adjustable properties (parameters) for a selected object, and section 4 (*Graphics*) exhibits the system geometry and resulting curves obtained from the simulation. It's possible to rotate the geometry by holding the left click button and moving the mouse. Translation can be accomplished by holding the right button of the mouse and dragging the cursor. In possession of such information, let's begin the construction of our project by defining some global parameters associated to it. To do so, click on *Home* (toolbar), after that click on *Definitions*. Then, select *Parameters*. Notice now that the *Setting* session has changed, and it now contains a table to be filled with global parameters. Fill this table accordingly to Table 6.

With the table filled, click on *Geometry 1* (model builder) and in the *Length unit* drop down bar replace *m* by *nm*. Right click *Geometry 1* and select a sphere. At the sphere *Settings* section, fill the field *Radius* and *z* with the parameters *radius* and *length/2*, respectively. In the

Table 6 – Global simulation parameters in COMSOL.

Name	Expression	Value	Description
length	L-D	-	-
D	L/AR	-	Nanorod diameter
radius	D/2	-	Nanorod radius
L	45	-	Nanorod length
AR	4.0	-	Nanorod aspect ratio
r_pml	3500	-	PML radius
lambda_ref	1240[nm]	-	-
lambda	1064	-	Wavelength
t_pml	1000	-	PML thickness
E_0	1[V/m]	-	Incident electric field
n_water	1.33	-	Water refractive index
Vol	(pi*((D[nm]) ^ 3)/2)*(AR/2 - 1/6)	-	Nanorod volume
S_{in}	((n_water*(E0 ^ 2))/(2*Z0_const))	-	Poynting vector of incident EM wave
beta	1 + 0.096587*(ln(AR)^2)	-	S2F shape factor
Req	(3*Vol/(4*pi))^(1/3)	-	Equivalent radius

Source: belongs to the author.

superior part of the settings menu, click *Build All Objects*. Repeat the step to add a second sphere. Fill the field *Radius* and *z* with the parameters *radius* and *-length/2*, respectively. Now, add a cylinder. Fill the field *Radius* and *z* with the parameters *radius* and *-length/2*, respectively. The field *Height* must be filled with *length*. Click on *Build All Objects*. After that, in the *Graphics* section, click on *Go to Default View*. You should now be able to see a nanorod. It is now necessary to connect all geometries into a single entity. To do so, left click *Geometry 1* in the model builder, go to *Booleans and partitions* and click on *Union*. In the *Graphics* screen, select the three geometries placed, and uncheck the field *Keep interior boundaries*. Click on *Build All Objects*. The nanorod now must be a single entity.

Add another sphere to the problem, and fill the *Radius* field with *r_pml*. In the bottom of the page, still in the *Settings* menu, expand the *Layers* field and add a new layer of thickness *t_pml*. In *Graphics*, click on *Go to Default View*. With the full view of the outside sphere that limits the nanorod domain, it is now necessary to define the domains and boundaries of the problem. click on *Definitions* (toolbar) and then click on *Explicit*. In *Geometry*, enable the option *Click and Hide*, and hide the spherical shell as a whole (click on the pieces to hide them). Disable the option *Click and Hide* and select the remaining surface. Enable the option *Click and Hide* once again, hide the surface (exposing the nanorod), disable the option *Click and Hide* and select the nanoparticle. In the settings panel you must be able to notice domains 5 and 6 selected. Rename the label *Explicit 1* to *Physical Domains*. In *Graphics*, click on *Reset Hiding*.

In *Definitions* (toolbar), click on *Complement* and rename its label to *PML Domains*. Still in the settings, look for the field *Input Entities* and click on *Add* in *Selections to invert*. A

pop-up will appear. Select *Physical Domains* and click on *OK*. Now, add a new *Explicit* and rename it as *Nanoparticle*. Hide once again the external sphere and the surface, and select the nanorod. Add another explicit, click on *Zoom Extents* (graphics) and in the parameter *Geometric Entity Level* (settings), replace *Domain* with *Boundary*. Select all the pieces of the nanoparticle surface and then rename the explicit to *Nanoparticle surface*. Add a fourth Explicit, click on *Reset Hiding*, *Zoom Extents* and change the *Geometric Entity Level* from *Domain* to *Boundary*. Select all parts of the external surface and rename the explicit as *External PML Surface*. Add a fifth and a last *Explicit*, change the option *Domain* with *Boundary* and rename it to *Internal PML Surface*. Hide the spherical shell and select only the remaining surface.

To define the PML, click on *Definitions* (toolbar) and click on *Perfectly Matched Layer*. In *Domain Selection* (settings) change *Manual* with *PML Domains*. In the bottom part of the menu, change the option *Geometry* from *Cartesian* to *Spherical*. Look for the field *PML Scaling factor* and define it as 0.5. Now, we proceed to add the materials of the problem. With the real and imaginary permittivity of gold nanorods in hand, go to *Definitions*, and select *Interpolations*. Click on *Load from File*, browser to the real permittivity file and select it. In *Interpolation and Extrapolation* bars, change *Interpolation* from *Linear* to *Cubic Spline*. In the field *Function name*, write *eps_real*. Repeat this process to the imaginary permittivity, and fill the field *Function name* with *eps_img*.

In the *Model builder* toolbar, right click *Materials*. Select *Blank material*. In the *Geometric Entity Section* change the drop down bar *Selection* from *Manual* to *Nanoparticle*. In *Material Contents*, fill the Relative permittivity value with *eps_real(lambda)-i*eps_img(lambda)*. The Relative permeability and electrical conductivity must be filled with 1 and 0 respectively. Add a new *Blank material*. In *Selection*, replace *Manual* with *All domains*. click on domains *6* (nanoparticle) and click to *Remove from Selection*. Fill the permittivity, permeability and conductivity fields with *n_waterˆ2*, *1* and *0* respectively. Now, we have to define the incident electromagnetic wave that will interact with the nanorod. To do so, in *Model Builder* click on *Electromagnetic Waves, Frequency Domain*. In *Settings*, replace the option *Solver* from *Full field* by *Scattered field*. Bellow, in *Background electric field*, fill the *z* component with *E0*exp(-j*2*n_water*pi/(lambda[nm])*x)*, while keeping *x* and *y* components null. Right click *Electromagnetic Waves, Frequency Domain* and select *Scattering Boundary Condition*. In *Boundary selection* replace *manual* with *Internal PML Surface*.

It is necessary to mesh the structure in order to proceed with calculations. To do so, in *Model Builder*, right click on *Mesh*, expand the *More Operations* option and select *Free triangular*. In *Boundary selection* change the option from *Manual* to *External PML Surface*. click on *Build All*. Right click once again in *Mesh*, but this time, select the *Swept* option. Change the *Geometric Entity Level* from *Remaining* to *Domain*, and change *Selection* from *Manual* to *PML Domains*. Right click *Swept* and select *Distribution*. Verify if the field *Number of elements* is defined as 5, and click on *Build All*. Right click *Mesh* once again, but this time, choose *Free*

Tetrahedral. Right click *Free Tetrahedral* and select *Size*. In the option *Element size*, expand the drop down bar and change from *Normal* to *Extra Fine*. click on *Build All*.

To define the analysis to be performed, the parametrization of frequency excitation is necessary. In *Model Builder* right click on *Study*, and select *Parametric Sweep*. In *Study Settings* click on *Add*. In the new parameter that showed up, select *lambda*. Fill the column *Parameter Value List* with *range(650,5,1050)*. In *Model Builder* click on *Step 1: Frequency Domain*, and in the field *Frequency unit*, write *Hz*. Replace the field *Frequencies* with *c_const/(lambda[nm])*. In the *Model Builder* click on *Component 1*. In the *toolbar* field *Definitions*, click on *Component Couplings* and select *Integration*. Modify the field *Operator Name* from *intop1* to *intop_vol*, and change the *Selection* field from *Manual* to *Nanoparticle*. Repeat the same procedure, but instead, the name of the new operator is *intop_surf*. In *Source Selection*, modify the *Geometric Entity Level* from *Domain* to *Boundary* and choose the *Selection* field as *Nanoparticle Surface*. Right click *Definitions* in *Model Build*, and select *Variables*. Fill the table that pops up accordingly to Table 7. Now we are ready to start the simulation. click on *Study* and select *Compute*. Wait until the simulation is finished. The resulting absorption cross section is presented in Figure 39.

Table 7 – Thermoplasmonic variables to be appraised in COMSOL.

Name	Expression	Value	Description
nrelPoav	nx*emw.relPoavx + ny*emw.relPoavy +	-	
	nz*emw.relPoavz	-	Poynting vector
sigma_sc	intop_surf(nrelPoav)/S_in	-	Scattering
sigma_abs	intop_vol(emw.Qh)/S_in	-	Absorption
sigma_ext	sigma_sc + sigma_abs	-	Extinction
J0	(lambda_ref/(2*pi))*(sigma_abs/Vol)	-	Joule number
S2F	sigma_abs/(beta*Req)	-	Steady-state Factor

Source: belongs to the author.

Figure 39 – Simulated absorption cross section for a 45×11 nm AuNR obtained by FEM using COMSOL.

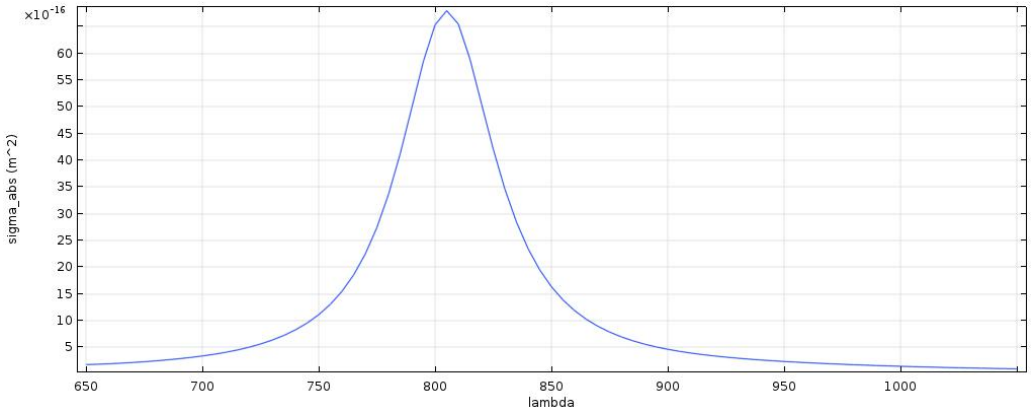

Source: belongs to the author.

To obtain the plots after the simulation is finished, it is necessary to evaluate the calculated data. click on *Results* (toolbar). In *Derived Values* look for *Global Evaluation*. In the settings, select the field *Data set* and choose *Study 1/Parametric Solution 1 (Sol2)*. In *Expression*, type the name of the expression of table 7 that you desire to appraise. In this case, type *sigma_abs*. After the expression was selected, click on *Evaluate* and wait the results to be processed. The generated table can be exported to an external file. Figure 39 depict the optical absorption cross-section response of a gold nanorod of size 41×11 nm.

The absorption cross section obtained by FEM simulations in COMSOL were compared to Mie-Gans theory calculations. To better describe the optical response of larger AuNRs, the Modified Long Wavelength Approximation (MLWA) [56] was employed. Figure 40 shows the comparison among Mie-Gans theory, FEM simulation and the experimental extinction of a 41×10 nm AuNR in water. The differences between FEM and Mie-Gans theory are explained by the actual shape of the nanostructure, since the simulated AuNRs are cylinders capped with hemispheres, while Mie-Gans theory describes spheroids. Nevertheless, both simulations show very selective peaks, while experimental extinction is broader. The observed difference in linewidth occur due to the presence of a distribution of AuNR sizes around the average (41×10 nm) in the experimental sample.

Figure 40 – Comparison of the absorption cross sections obtained by FEM simulations and Mie-Gans theory for 41x10nm AuNR.

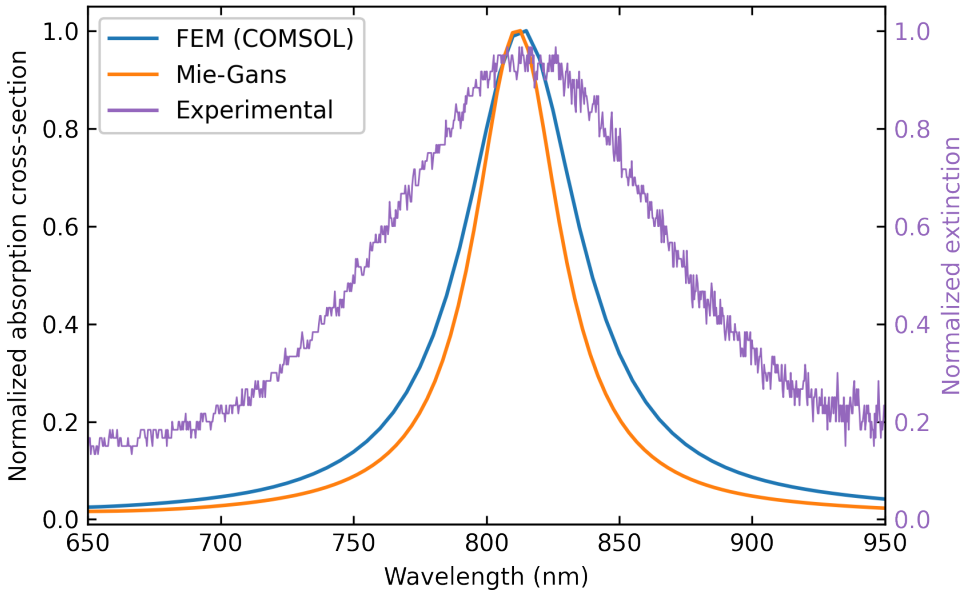

Source: belongs to the author.

APPENDIX C – ON-CHIP LENSLESS CONTACT-MODE MEASUREMENTS ON CMOS IMAGE SENSORS

During the course of my doctorate, I was awarded a scholarship that allowed me to move to Montreal (Canada) for 11 months, where I worked in the Department of Bioengineering at McGill University from April 2023 to March 2024, under the supervision of Prof. Sebastian Wachsmann-Hogiu. The development of lensless on-chip platforms enables the development of compact imaging devices. The low-cost optics as well as the size of such devices are advantageous for Point-of-Care applications that require simplicity and scalability in resource-poor environments. Therefore, the development of new biosensing platforms in conjunction with low-cost colorimetric detection techniques and lensless and on-chip microscopy becomes highly desirable, allowing the emergence of innovative applications. During this exchange, I was involved in the development of such platforms for sensing and imaging of on-chip samples on CMOS sensors, aimed at fluorescence and polarization detection.

Amid the exchange, with assistance provided by McGill University, I attended Photonics West 2024, hosted in San Francisco (California), where two two abstracts were submitted to SPIE BiOS. Organized by SPIE, Photonics West is the largest annual international conference in optics and photonics and SPIE BiOS is the most important biomedical optics conference in the field. The first work submitted, entitled "*Contact-Mode Fluorescence Measurements on a Lensless CMOS Image Sensor*" was related to activities developed by me at the Department of Bioengineering at McGill University, while the second work, entitled "*Size-dependence Gold Nanosphere Mediated Photoacoustic Generation*" was related to research activities linked to my doctorate and carried out in Brazil. The latter was awarded at the conference at which it was presented (Nanoscale Imaging, Sensing and Actuation for Biomedical Applications XXI), where I was awarded the Prizmatix Young Investigator Award.

TOTAL INTERNAL REFLECTION FLUORESCENCE

Fluorescence detection was implemented a Raspberry Pi camera (Rev 1.3), exposing the CMOS sensor by removing the lens and placing the samples in direct contact with the chip. Due to proximity, it is not possible to use optical filters to suppress the excitation beam. To achieve contact-mode imaging, we explored a Total Internal Reflection (TIR) configuration. In TIR fluorescence (TIRF), a prism is used to couple light, shown in Figure 41A. At the reflection interface, an evanescent wave arises penetrating the medium (Figure 41C) and promoting sample fluorescence that is detected by the camera. Fluorescence emission is then measured without lenses or filters. This can be seen in Figure 41D, of Rhodamine 6G in ethanol. The whole sensor area correspond to the camera field of view (FoV) and Rhodamine fluorescence is visible only where the laser undergoes TIR.

Figure 41 – On-chip lensless contact-mode fluorescence measurements. **A.** Schematic of the TIR on-chip device. **B.** Experimental setup. **C.** Depiction of penetrating evanescent waves arising at the TIR interface. **D.** Close-up of TIR on-chip device with Rhodamine 6G fluorescence in ethanol. The whole FoV of the camera is depicted here.

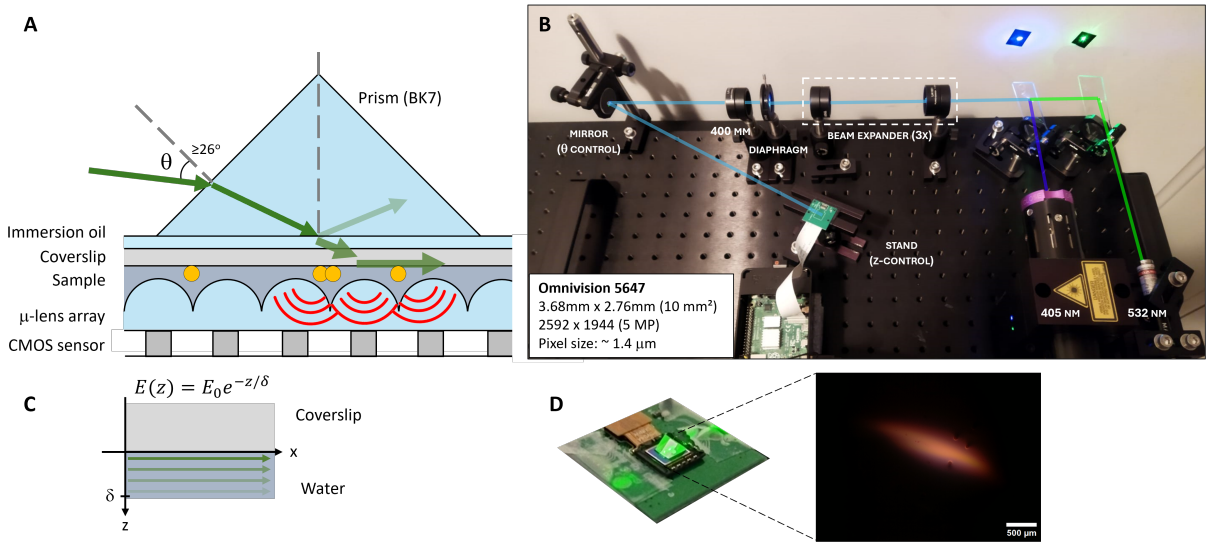

Source: belongs to the author.

The next step was to test fluorescent microspheres. Here, $10.7\ \mu\text{m}$ beads were imaged in both bright field (Figures 42A and 42C) and TIRF (Figures 42B and 42D). It is apparent how much laser scattering (blue) affects the image. In such proximity (in which the actual size of the microspheres spans only a few pixels), the scattered and the fluorescent lights through the Bayer filter contributes to the appearance of wrong colors, as seen in Figure 42B. The developed imaging platform has the potential to achieve micrometer-scale spatial resolution (Figure 42E) with a huge field of view, determined by the size of the sensor.

Figure 42 – $10.7\ \mu\text{m}$ fluorescent microspheres (Nile Red) in **A.** bright field configuration; **B.** TIRF (ex. 405 nm); **C.** close up of side-by-side fluorescent beads; and **E.** resolution test. The yellow dashed and solid lines delineate the profiles for the resulution test.

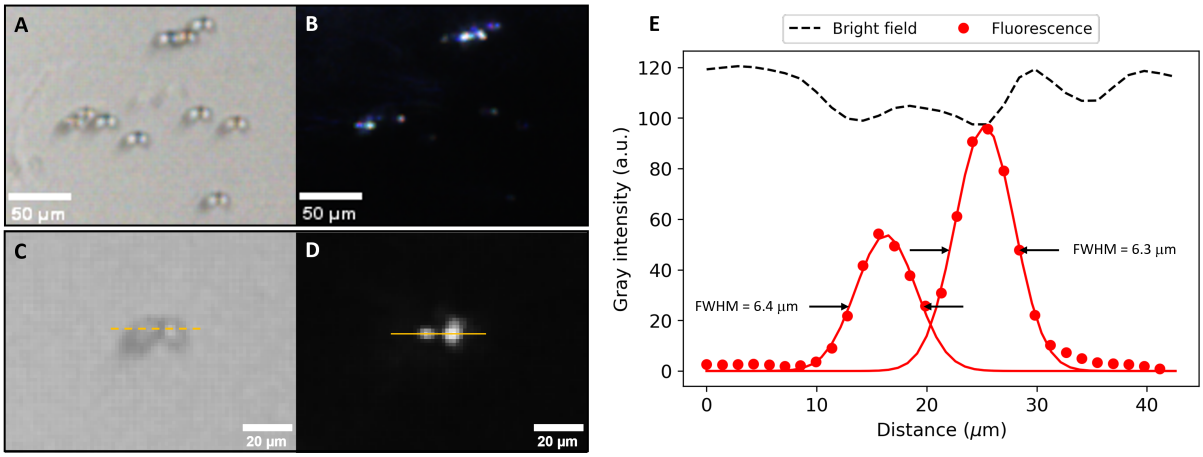

Source: belongs to the author.

POLARIZED LIGHT MICROSCOPY

Similarly, LED lighting has been explored in conjunction with crossed polarizers to perform on-chip polarization microscopy. Polarized light microscopy is a technique in which polarizing filters are used to extract optical information from birefringent materials (Figure 43A). Figure 43C illustrate the experimental setup, that comprised of a non-polarized illumination source (white LED), a set of cross polarizers and a full waveplate. The illumination source is collimated and then polarized by the first linear polarizer. A full waveplate is used to add or subtract effective retardance from the sample (Figure 43B). The birefringent sample is then dropcasted on top of the cross polarizer, that is in contact with the image sensor and forms the polarization analyzer (Figure 43D). Figure 43E and 43F are the resolution tests conducted for polystyrene beads.

Figure 43 – Experimental setup and characterization of on-chip lensless cross-polarization platform. **A.** Schematic diagram of the experimental setup; **B.** depiction of the main elements of the device; **C.** experimental setup implementation; **D.** close up of the polarization analyzer (image sensor + cross-polarizer); and resolution tests for **E.** one and **F.** two polystyrene beads.

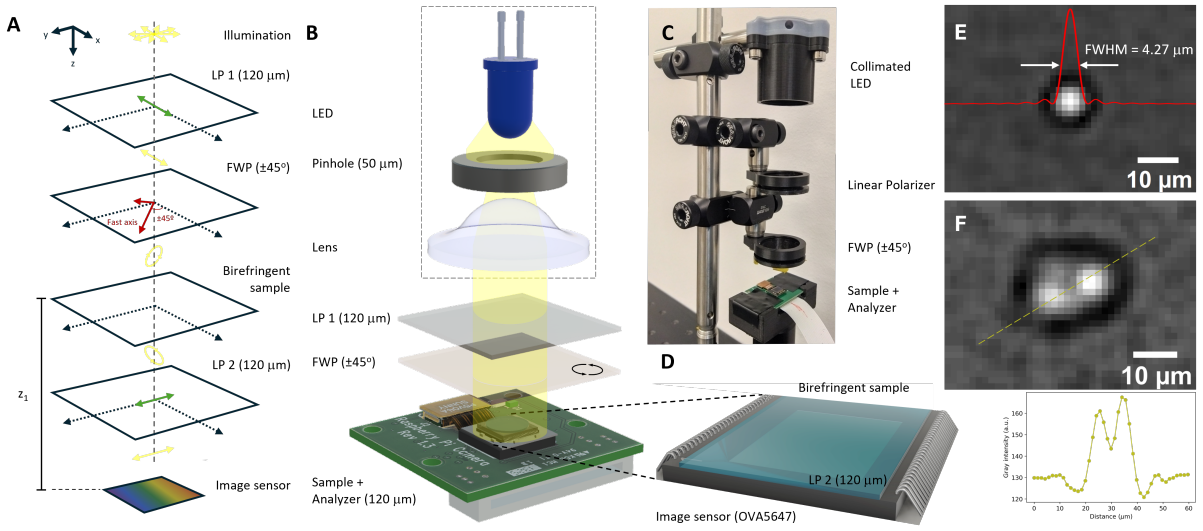

Source: belongs to the author.

In Figure 44, the effect of the full waveplate (FWP) in birefringent samples with low order interference colors is demonstrated. The FWP introduces additional phase shift, enhancing the interference colors. Rotating the FWP by + (-) 45° add (subtract) phase shift to the sample, and slightly change the interference colors by producing higher (lower) order interference patterns. This process is wavelength dependent and is typically explored for sample identification in fields such as geology and rheumatology. Here, the addition and subtration of phase shift is shown exploring the birefringence of organic molecules such as Ascorbic acid and living organisms (Euglena). The correlation between interference color, sample thickness and birefringence is well known and documented by the Michel-Lévy interference color chart.

Figure 44 – Birefringent samples under on-chip polarized light microscopy. Without the FWP, interference wavelength is too small and the colors appear washed. Phase shifted is introduced by adding the FWP through the increase of interference order. Positioning the FWP at $\pm 45^{o}$ produce slight changes in the interference colors and enable sample identification. The yellow arrows depict the FWP positioning.

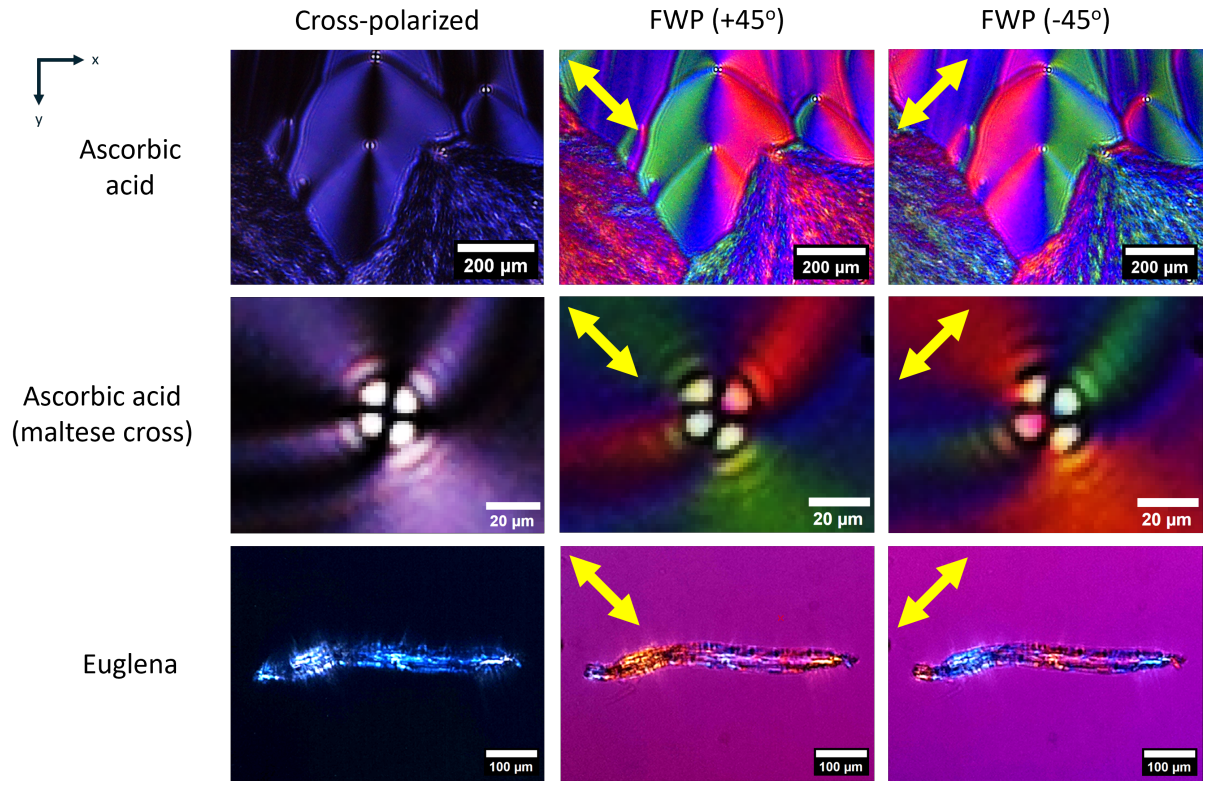

Source: belongs to the author.

With some mathematical modeling, the obtained color images can be explored to extract quantitative data from birefringent samples. This process involved the implementation of an algorithm responsible for transforming the interference colors that resulted from the birefringence of the samples into phase differences, producing phase images. Our approach calculates simple polarization rotations in the optical path and compute the interference colors. Waveplates and polarizers are modeled analytically using the Jones formalism. Therefore, the polarization rotation detected at the CMOS sensor for a given wavelength ($\mathrm{J_{Txy}}(\lambda)$) is:

$$J_{Txy}(\lambda) = M_{y-pol}(\lambda) M_{sample}(\lambda) M_{fwp}(\pm\pi/4, \lambda) J_{xy}(\lambda) \ , \tag{C.1}$$

in which $\mathrm{J_{xy}}(\lambda)$ represents x-polarized (horizontal) light and $\mathrm{M_{y-pol}}(\lambda)$ is the Jones matrix for y-axis (vertical) polarizer. The spectral distribution of the light source must be considered, as it directly affects the resulting colors. The FWP ($\mathrm{M_{fwp}}$) and the birefringent sample ($\mathrm{M_{sample}}$) are modeled as linear phase retarders:

$$M_{fwp}(\pm\pi/4,\lambda) = R(\pm\pi/4)\begin{bmatrix}1 & 0\\ 0 & e^{j\phi_0(\lambda)}\end{bmatrix} \text{ and} \tag{C.2}$$

$$M_{sample}(\lambda) = \begin{bmatrix}1 & 0\\ 0 & e^{j\phi(\lambda)}\end{bmatrix} . \tag{C.3}$$

Here, $\mathrm{R}(\pm\pi/4)$ is the rotation matrix at $\pm 45^{\mathrm{o}}$, $\phi_0(\lambda)$ is the FWP phase shift and $\phi(\lambda)$ is the phase shift introduced by sample birefringence.

From the spectral distribution of the light source, this framework is used to compute the resulting color at the CMOS sensor, based on the phase shift seen by each wavelength. The phase shift is swept for all wavelengths and the resulting spectrum of the light reaching the image sensor is thus converted into an effective color using the CIE's color matching functions. Following this method, the effective interference color is calculated for each phase shift and stored in an interference colorspace for later use.

The stored data is used to solve the inverse problem: if the illumination setup and waveplate rotation are know, phase shift can be extracted from a sample based on the interference colors it shows. Due to the similarity of the colors throughout inteference orders, a further minimization step based on CIE2000 (color difference formula) is required to discriminate the correct phase shift. The process is repeated for each pixel of the image. Therefore, quantitative data from a real sample is extracted and a phase map is reconstructed from a color image.

Furthermore, as white light is employed, the monochromatic relation between phase shift and the sample properties, $\phi(\lambda) = \phi_0(\lambda) + \frac{2\pi\delta(\lambda)}{\lambda}$, cannot be used. Here, $\delta(\lambda) = \mathrm{t}\ \Delta\mathrm{n}(\lambda)$ is the optical path difference for sample thickness t and sample birefringence $\Delta\mathrm{n}$. Consequently, the spectrum of the light source must also be considered:

$$\phi \ = \ \phi_0 \ - \int_{\lambda_i}^{\lambda_f} \frac{\delta(\lambda)}{\lambda^2} d\lambda \ . \tag{C.4}$$

Since δ is a parameter intrinsic to the material, if t is known, $\Delta\mathrm{n}$ can be retrieved, and vice versa.

To demonstrate the process for a single image pixel, a flat piece of birefringent mica of known thickness ($210\ \mu\mathrm{m}$) was used. Subjecting the sample to on-chip polarized light microscopy produced an image containing only one color, uniform across the FoV. Figure 45 illustrate the perceived difference in color as function of the sample birefringence. The two possible values are highlighted by red arrows and the actual color sampled by the CMOS sensor is also shown. After minimization, the calculated birefringence was estimated as 0.0051, a close match to the actual mica birefringence (0.0054) [237].

Figure 45 – Process applied for the discrimination of mica birefringence. Given the colorspace and known thickness, the birefringence was retrieved using the minimization process described.

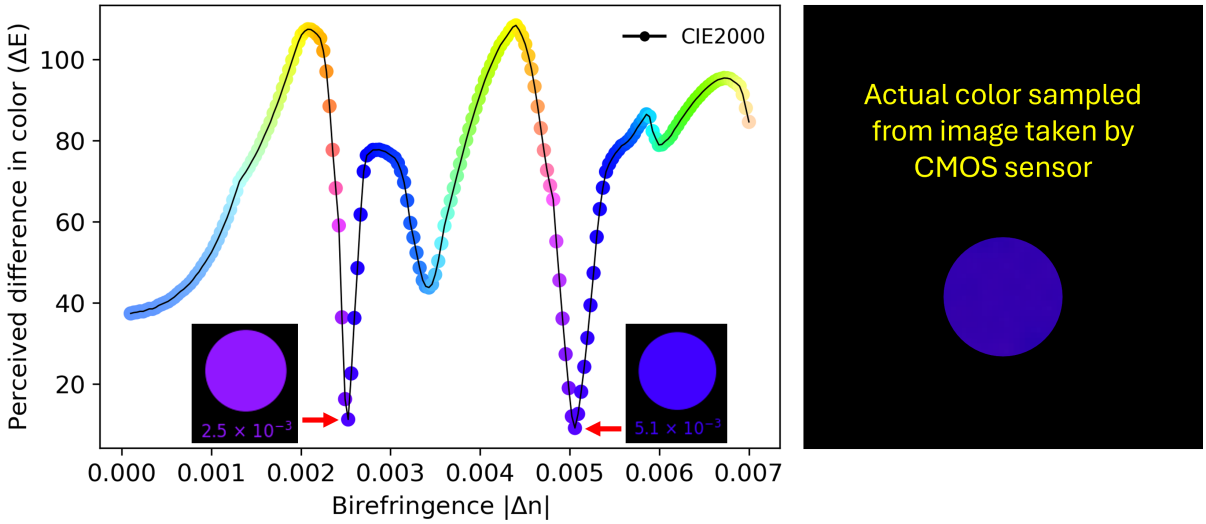

Source: belongs to the author.

Additionally, monosodium urate crystals (MSU) were synthesized following the methodology reported by Liu et al.[238]. MSU is one of the most common salts formed by uric acid ions and its presence in synovial fluid is an indicative of gout. Gout is a common crystal-induced arthritis, in which MSU crystals precipitate within synovial fluid and tissues, resulting in a dramatic inflammatory response characterized by intense pain. The synthesized crystals pictured in Figure 46 show the typical long needle-shape expected from MSU crystals.

Figure 46 – Bright field image of the synthesized MSU crystals showing their distinct long needle-shape format.

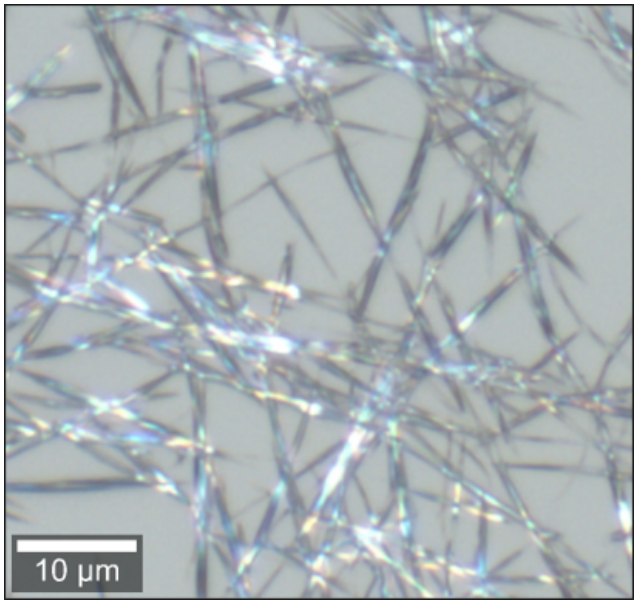

Source: belongs to the author.

The sample was dropcasted in the setup and imaged under cross-polarization at different retardances using the waveplate to enhance interference colors. The interference colors were processed and a phase image was obtained for each case. This procedure is depicted in Figure 47. Gout crystals are generally long and needle-like, negatively birefringent and their long axis is the "fast" axis. When the long (fast) axis of a gout crystal is aligned with the slow axis of the FWP, the phase difference results in a yellow interference color. If the long (fast) axis of a gout crystal is aligned with the fast axis of the FWP, then the phase difference results in a blue color. Phase maps (virtual colors) were obtained from the acquired interference color images, as seen in Figures 47. The reconstructed phase shift is negative, in accordance to the negative birefringence of MSU crystals.

Figure 47 – Steps for phase map extraction using the synthesized MSU crystals. The reconstructed phase maps (virtual colors) corroborate with the negative birefringence of MSU crystals.

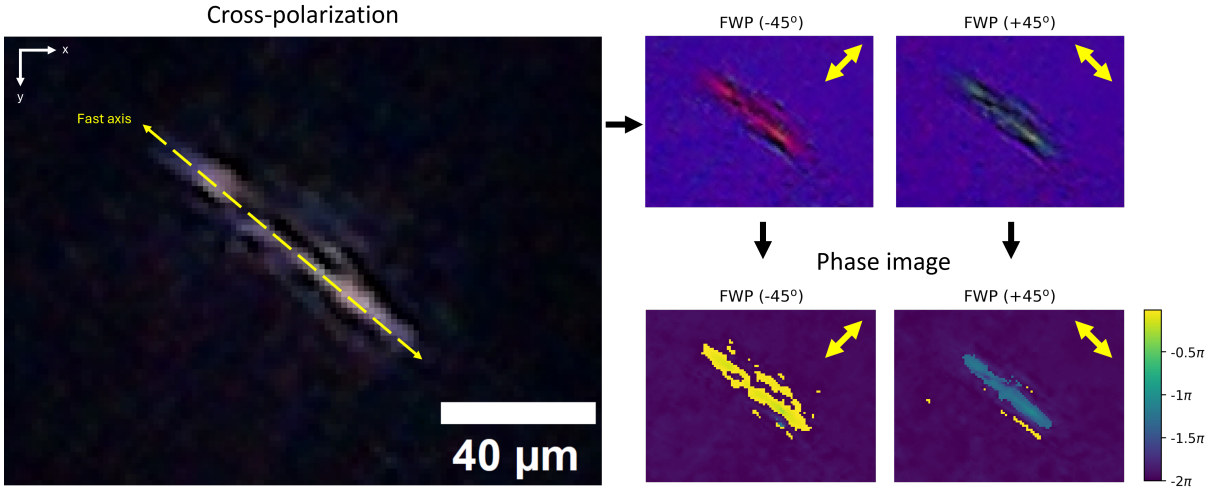

Source: belongs to the author.

Moreover, despite our attempts to experimentally demonstrate the developed technique in the detection of MSU crystals, whose presence in synovial fluid is indicative for the diagnosis of gout, further characterizations are still needed to validate the proposed methodology.

ANNEX A - REFRACTIVE INDEX OF POLYDOPAMINE

In this annex, we provide experimental data used for the execution of this dissertation, but that isn't easily accessible. This concerns data reported in the literature or made available by vendors in image format, which hinders their straightforward use. Furthermore, the reported data is not available on mainstream online databases. From figures, the online app WebPlotDigitizer 4.8 (https://apps.automeris.io/wpd4/) was used to extract and export data in table format.

The real and imaginary parts of the refractive index of polydopamine were obtained from Qie, Moghaddam e Thormann[1]. Here, the authors extracted optical models from ellipsometry of thin film samples of polydopamine. The extracted data, which is available below in table format, was used to reproduce the real ($\epsilon_r = n^2 - \kappa^2$, Figure 48A) and imaginary ($\epsilon_i = 2n\kappa$, Figure 48A) permittivities of polydopamine.

Figure 48 – **A.** Real and **B.** imaginary permittivities of polydopamine, obtained from refractive index data extracted from Qie, Moghaddam e Thormann[1].

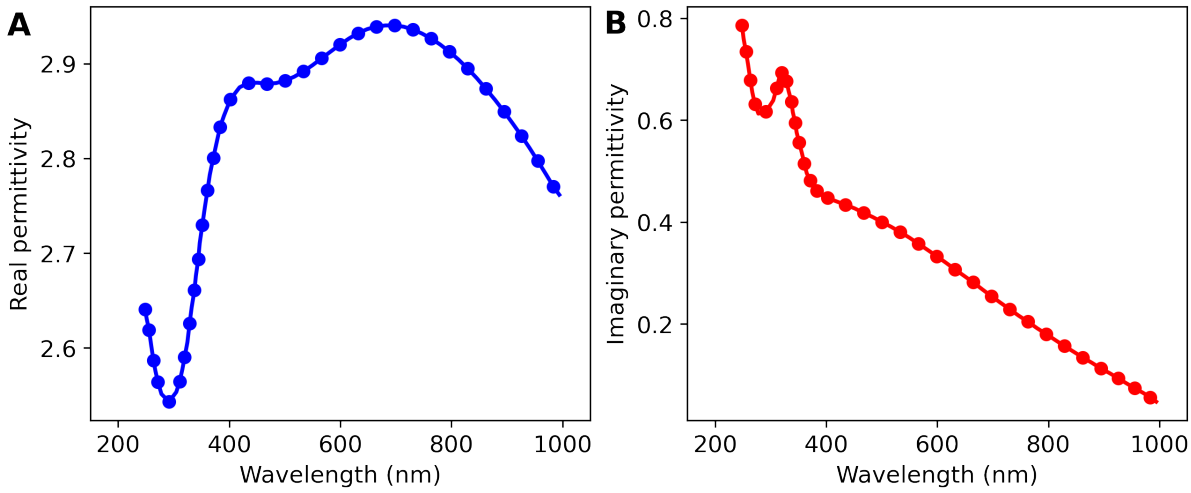

Source: belongs to the author.

$\lambda\ (\mu m)$	n	κ	$\lambda\ (\mu m)$	n	κ	$\lambda\ (\mu m)$	n	κ
0.2484	1.6425	0.2392	0.3607	1.6703	0.1542	0.6646	1.7163	0.0820
0.2514	1.6383	0.2317	0.3649	1.6746	0.1481	0.6810	1.7165	0.0780
0.2555	1.6339	0.2247	0.3712	1.6796	0.1433	0.6975	1.7163	0.0741
0.2593	1.6281	0.2179	0.3776	1.6844	0.1396	0.7139	1.7157	0.0704
0.2634	1.6219	0.2091	0.3834	1.6887	0.1365	0.7303	1.7147	0.0668
0.2671	1.6175	0.2022	0.3904	1.6920	0.1339	0.7467	1.7134	0.0631
0.2716	1.6131	0.1958	0.4021	1.6970	0.1318	0.7632	1.7117	0.0597
0.2779	1.6086	0.1904	0.4185	1.7005	0.1295	0.7796	1.7097	0.0561
0.2915	1.6062	0.1919	0.4349	1.7017	0.1274	0.7960	1.7074	0.0528

0.3046	1.6102	0.1983	0.4513	1.7016	0.1254	0.8125	1.7049	0.0494
0.3107	1.6146	0.2052	0.4678	1.7011	0.1228	0.8289	1.7020	0.0460
0.3154	1.6191	0.2107	0.4842	1.7011	0.1204	0.8454	1.6990	0.0428
0.3196	1.6235	0.2134	0.5006	1.7017	0.1175	0.8618	1.6956	0.0396
0.3246	1.6281	0.2120	0.5170	1.7027	0.1147	0.8783	1.6921	0.0366
0.3285	1.6335	0.2070	0.5334	1.7041	0.1115	0.8947	1.6883	0.0334
0.3324	1.6381	0.2005	0.5498	1.7058	0.1083	0.9106	1.6844	0.0307
0.3374	1.6427	0.1937	0.5662	1.7077	0.1046	0.9258	1.6806	0.0278
0.3398	1.6464	0.1870	0.5826	1.7096	0.1010	0.9405	1.6767	0.0249
0.3442	1.6511	0.1802	0.5990	1.7115	0.0973	0.9552	1.6726	0.0221
0.3468	1.6555	0.1738	0.6154	1.7132	0.0935	0.9699	1.6684	0.0195
0.3514	1.6606	0.1674	0.6318	1.7147	0.0895	0.9834	1.6645	0.0169
0.3561	1.6656	0.1608	0.6482	1.7157	0.0858	0.9940	1.6618	0.0143

ANNEX B - AWARDS

SBEB

A **Sociedade Brasileira de Engenharia Biomédica** confere a

Túlio L. Pedrosa

o **1º lugar** do

Prêmio Antonio Fernando Catelli Infantosi

pela apresentação do trabalho intitulado

Otimização de Nanobastões de Ouro para Terapia Fototérmica de Alta Performance

em coautoria com Sajid Farooq e Renato E. Araujo, durante o

XXVII Congresso Brasileiro de Engenharia Biomédica

realizado de 26 a 30 de outubro de 2020.

Rio de Janeiro, 28 de outubro de 2020

Rodrigo Pereira Baretto da Costa-Félix
PRESIDENTE DA SBEB

Adriano de Oliveira Andrade
COORDENADOR GERAL DO PROCESSO DE AVALIAÇÃO

SPIE. PHOTONICS WEST

PRIZMATIX YOUNG INVESTIGATOR AWARD

Tulio de Lima Pedrosa

University Federal de Pernambuco Brazil and McGill University

Size-dependence gold nanosphere mediated photoacoustic generation

Presented at
Nanoscale Imaging, Sensing, and Actuation for Biomedical Applications XXI

Presented by
Dror Fixler, Bar-Ilan University
Sebastian Wachsmann-Hogiu, McGill University

2024 Conference Chairs

CamScanner